UNIVERSITÀ
DEGLI STUDI
DI PADOVA

Sede Amministrativa: Università degli Studi di Padova

Dipartimento di Territorio e Sistemi Agro Forestali

SCUOLA DI DOTTORATO DI RICERCA IN TERRITORIO AMBIENTE RISORSE SALUTE
CICLO XXVIII

THE USE OF STRUCTURE FROM MOTION TECHNOLOGIES FOR HIGH-RESOLUTION TERRAIN MODELLING ON HIGH ALTITUDE CATCHMENTS

Direttore della Scuola: Ch.mo Prof. Mario Aristide Lenzi
Supervisore: Ch.mo Prof. Antonio Vettore
Co-supervisore: Ch.mo Prof. Norbert Pfeifer

Dottoranda: Livia Piermattei

The use of Structure from Motion technologies for high-resolution terrain modelling on high altitude catchments

Author

Livia Piermattei

University of Padova

livia.piermattei@studenti.unipd.it
livia.piermattei@libero.it

Department of Land, Environment, Agriculture and Forestry (TESAF)

Supervisor

Antonio Vettore

University of Padova

antonio.vettore@unipd.it
+39 0498272688

Via dell'Università 16
35020, Legnaro (PD), Italy

Department of Land, Environment, Agriculture and Forestry (TESAF)

Co-supervisor

Norbert Pfeifer
Vienna University of Technology

norbert.pfeifer@geo.tuwien.ac.at

+43 (1) 58801 12219

Gußhausstraße 27-29
1040, Vienna, Austria

Department of Geodesy
and Geoinformation (GEO)

ABSTRACT

The research project developed in this Thesis involves the application of close-range photogrammetry based on the Structure from Motion (SfM) approach that allows reconstructing the 3D point cloud of the photographed object from a sequence of overlapping images taken with a common digital camera. Thanks to the characteristics of high portability of the equipment, flexibility of the method to reconstruct surface at different scale with high resolution, low-cost, and ease of use also for not expertise during both acquisition and processing phase, the SfM-photogrammetry is becoming a valid alternative to the range-based technology for remote sensing and monitoring of dynamic natural environments. The aim of this research was to test and validate the capability of a ground photogrammetric survey to reconstruct a surface by dealing the main practical issues of a ground acquisition and by highlighting the main error sources which may be present within the field data. Furthermore, the feasibility of the SfM-photogrammetry approach for monitoring glacial and periglacial processes was tested in order to highlight the limitation and the potential of the method for these applications.

A total of four study sites were surveyed in order to validate the photogrammetric method. A depth investigation on the photo-based approach was carried out in a test field area where different image acquisition, georeferencing methods and processing were compared and evaluated. A terrestrial panorama images acquisition was proposed and tested in this work. This acquisition strategy provided advantages in comparison to a normal single frame acquisition by increasing the spatial coverage of the reconstructed surface and the number of overlapping images that ensure higher accuracy.

The potential and limits of the ground-based SfM-photogrammetry approach for monitoring glacial and periglacial processes were investigated in three different environments. For each of these study areas several tests concerning the quality of the obtained photogrammetric digital elevation models (DEMs) were performed. Different resolution and accuracy of the photogrammetric DEMs were obtained for the three case studies according to the different ground survey characteristics and survey object (i.e. extension and accessibility of the areas, camera-object distance, surface coverage, and camera resolution and geometry network). For the investigated areas, the main practical problems of the ground photogrammetric surveys that affected the SfM-photogrammetry results were: i) image quality determined by poor texture (i.e. snow and dark rock area with low contrast) and strong illumination variations during long time photos acquisition, ii) camera network geometry (i.e. high camera-object distance, poor overlapping images) and iii) distribution and accuracy of control measurements. However, the photogrammetric 3D model allowed us to estimate with good accuracy the glacial and periglacial processes respect to the reference data.

The investigation on the SfM-photogrammetry quality reconstruction allowed to have a complete view of the critical points and the potential of this method for multitemporal analysis in remote alpine area and thus to assess the applicability range for future realistic case scenarios.

RIASSUNTO

L’attività di ricerca sviluppata in questa tesi riguarda lo studio e l’applicazione della fotogrammetria close-range basata sulla tecnica della Structure from Motion o image-based modeling) per la realizzazione di modelli digitali del terreno (DEMs) ad alta risoluzione che costituiscono la base informativa fondamentale per analisi geomorfologiche. Per Structure from Motion (SfM) si intende una tecnica di calcolo che consente di ricostruire tridimensionalmente un oggetto reale da una serie di immagini sovrapposte ricorrendo alle formulazioni proprie della fotogrammetria e agli automatismi (algoritmi) della Computer Vision. La SfM comparata alla tecnologia laser (LiDAR) presenta numerosi vantaggi legati alla elevata portabilità della strumentazione, flessibilità del metodo di ricostruire superfici a diverse scale ad alta risoluzione, il basso costo e la facilità di applicazione, anche da non esperti, sia durante la fase di acquisizione che di elaborazione dei dati. Per tali motivi questa metodologia di rilievo sta diventando una interessante alternativa alla tecnologia LiDAR, in particolare per il rilievo e monitoraggio di ambienti naturali in zone remote. L’obiettivo principale della ricerca è stato quello testare le potenzialità della fotogrammetria terrestre per generare DEMs con accuratezze e precisioni adeguate all’oggetto rilevato e al tipo di analisi, in particolare alle analisi dei processi glaciali e periglaciali. Una indagine approfondita sui principali problemi pratici legati ad un rilievo fotogrammetrico terrestre e sulle principali fonti di errore che caratterizzano il metodo è stata eseguita su un’area di studio. Diversi sono i fattori che influenzano la qualità del modello fotogrammetrico in termini di accuratezza, precisione e risoluzione. Si è dimostrato che la geometria di presa delle immagini e la distribuzione dei punti di controllo necessari per la georeferenziazione sono i fattori chiave che determinano la qualità del modello e possono portare alla formazione di distorsioni se non accuratamente pianificati. Per migliorare la geometria di presa delle immagini è stata testata una diversa strategia di acquisizione basata su immagini panoramiche. Rispetto ad una acquisizione di singole immagine acquisite ad ogni posizione, una acquisizione multi immagine ha generato accuratezze più elevate e una copertura spaziale maggiore dell`area ricostruita. Per validare la tecnica della fotogrammetria terrestre in ambiente glaciale e periglaciale sono stati identificati tre casi studio con diverse caratteristiche in termini di accessibilità, estensione della superficie e tipo di copertura (detrito, neve fresca e roccia). Nello specifico sono stati rilevati con la fotogrammetria terrestre il ghiaccio del Montasio Occidentale, il ghiaccio di La Mare e il rock glacier AVDM3 al fine di calcolare il bilancio di massa annuale dei ghiacciai e le velocità di scorrimento del rock glacier. L’accuratezza del metodo fotogrammetrico è stata convalidata per ogni singolo caso studio con dati LiDAR. Diverse sono le accuratezze e le precisione ottenute nei tre casi studio. Tuttavia, i DEMs generati dalla fotogrammetria hanno permesso di stimare con buona precisione i processi glaciali e periglaciali con accuratezze comprabile con la tecnologia laser. Le indagini effettuate sui vari casi studio hanno permesso di avere una visione completa sul metodo della SfM e sui punti critici e le potenzialità di questo tecnica di rilievo per l'analisi multi-temporale in bacini montani.

ACKNOWEDGEMENTS

Here I am to write the doctoral thesis, a project started by a simple idea after a meeting, and developed over three years in a completely unexpected but with growing up of satisfaction and enthusiasm. Three years of change, growth, unique persons and valuable contacts for a future still in the research (I will carry out my dream!).

Thanks go to my supervisor, Antonio Vettore, with whom I had the pleasure to work and express my ideas, that supported me and left me the autonomy to plan my project, trusting me, and thus increasing my sense of responsibilities and my personal growth. Special thanks to Norbert Pfeifer, an outstanding Researcher and Professor and person, who welcomed me for one year in his research group, and that taught me and helped me to reason, concluding thus this study in the best way, above all expectation. It was for me a fundamental point of reference.

A special thanks to:

- Luca Carturan, for making me discover the mountains and glaciers, by explaining and explaining and explaining how they "work", and for sharing with me all his strength and passion that puts in the research and in "his glaciers" ...I could say, unique! And not least thanks for the friendship and demonstrated willingness to listen to me when I needed it.
- The whole group of Geomatics and CIRGEO for putting up with me during the two years in Legnaro and even when I was abroad, always willing to help me in the work but also in the personal lives.
- Alberto Guarnieri, for his teaching and friendship demonstrated on many occasions.
- Paolo Tarolli for helpful advice and encouragement in this research.
- Department of TESAF, the Forestry group, with special thanks to Alan Crivellaro, and to the entire laboratory IDEA.
- To my family (mom, dad, Alma and Edoardo) and to my closest friends for the many encouragements and necessary distraction.
- Victor Modamio for his presence that has changed my life.

During the last year of the PhD I had the opportunity to work at the Department Geodesy and Geoinformation at the TU Vienna. A special environment, friendly, perfectly organized, with very high level of research and even more united. Thanks to each of them.

TABLE OF CONTENTS

1

INTRODUCTION

Three-dimensional (3D) topographic reconstructions based on high resolution digital elevation models (DEMs) are the main product for a variety of applications in remote-sensing research as they represent the principal products for understanding the morphology of the terrain and the analysis of processes (Barrand et al., 2009). High-resolution topography offers powerful new insights in numerous Earth science fields, including process geomorphology, hydrology, sedimentology, and structural geology. In recent decades, new remote sensing techniques, such as airborne laser scanning (ALS) and terrestrial laser scanning (TLS) using light detection and ranging technology (LiDAR), are the most prevalent techniques for high-density and high-accuracy 3D terrain point data acquisition that revolutionized the quality of the DEMs (Tarolli et al., 2009; Brasington et al., 2012). However, the high costs and logistical demands of these range-based survey techniques can restrict their utilization (Johnson et al., 2014).

The increased need to reduce the costs and operational limits of LiDAR applications in areas that are not easily accessible, has increased the use of digital close-range photogrammetry survey technique. In addition, recent improvements in the quality and performance of digital cameras for close range applications and advances in computer vision/image processing have prompted the development of a photogrammetric approach that is ideally suited for low-budget research and application in remote areas (James and Robson, 2012). This emerging low-cost and straightforward photogrammetric method represent the latest stage of an evolutionary story, in which imagery has been employed for spatial measurements in earth science and specifically geomorphology. This method is based on structure-from-motion (SfM; Ullman, 1979) and dense image matching algorithms, enables the automated production of high-resolution topographic reconstructions from multiple overlapping photographs, which are captured by a camera that moves around a scene (Fisher et al., 2013; Quan and Kanade, 2010). While not originally intended for geological applications, since 2011, geoscientists have adopted SfM-photogrammetry as a methodology for collecting low-cost, high spatial resolution three-dimensional data for topographic and surface modeling (Dietrich, 2015). Additionally, the development of software with a user-friendly interface and a high level of automation in image processing has promoted the extensive use of this photogrammetric technique in geoscientific applications (e.g. James and Robson, 2012; Diefenbach et al., 2012; Westoby et al., 2012; Bretar et al., 2013; Fonstad et al., 2013; Kääb et al., 2013; Bemis et al., 2014; Javernick et al., 2014).

SfM-photogrammetry has some distinct advantages over TLS and ALS that make it ideal for a wide range of geomorphic research especially in remote areas. The LiDAR system can acquire data up to hundreds of thousands of points per second. ALS is useful for quickly mapping wide areas, with a high degree of automation and the point resolution and accuracy results in decimetre scale (Bangen et al., 2014). However, the high costs, the difficulty of detecting areas at lower spatial scales, and the presence of rock walls are factors that reduce the capability of observation by aircraft and require integration with ground surveys. The use of TLS enables high-resolution surveys to be conducted from more suitable and safe locations, and the construction of high-quality DEMs (in terms of point density) compared with ALS. TLS became a well-established methodology in geomorphology over small spatial scales. However, this type of instrumentation involves a high initial investment, requires experienced personnel for its use and data processing, and entails logistic difficulties and costs for transportation of the equipment. Traditional topographic surveys by means of Total Station (TS) and Differential Global Positioning System (dGPS) are subject to many of the same advantages (accuracy and precision) and disadvantages as the LiDAR technology, but additionally with a low point density achievable within a survey campaign. In terms of point density, the resulting data of SfM-photogrammetry are most similar to those obtained by TLS by reaching similar and also greater point densities and while point precision and accuracy is mostly determined by survey range, sub-cm scale errors are achievable (Smith and Vericat, 2015).

Summarizing the characteristics of airborne and terrestrial LiDAR surveying in remote environments, the first advantage of SfM-photogrammetry as alternative to LiDAR technology is the cost and high portability of the instrument. Furthermore, SfM-photogrammetry using both commercially and open source software packages is highly automated and therefore can be easily performed by non-experts. Researchers can collect imagery acquired both at nadiral and obliquely, varying resolution and with any digital camera, as non-metric camera is required. The data collection can be easily deployed by a person working alone. Recently, certain researchers included also the smartphone imagery in a SfM-photogrammetry workflow. The other advantages are the flexibility to capture data at a wide range of spatial scales (from a few centimeters up to kilometres), and rapidly generate sub-decimetre-resolution DEMs and orthophotos. Certainly, SfM-photogrammetry is not a complete substitute of the others survey methods outlined above and it is clear that each technique has different strengths and weakness, hence each of them is better suited to a different task (Smith et al., 2015). However, thanks to the characteristics highlighted above, the SfM-photogrammetry could result useful for a variety of research fields and civil purposes. In particular, when the surface is characterized by a rapid variability over time, the importance of having a low-cost method that can provide precise results is more apparent.

The research project concerns the study and the application of the low-cost SfM-photogrammetry technique to realize high resolution DEMs. The aim of the research was to identify some practical aspects and challenges related to the application of terrestrial SfM-photogrammetry in the remote areas using a common SRL digital camera. In detail, the applicability of the ground photogrammetric approach for glacial and periglacial multitemporal-analysis was investigated in this work. Different image acquisitions and image processing methods were tested in order to obtain DEMs with accuracy and precision appropriate to the type of analysis. Then, in order to verify the feasibility and efficiency of the proposed method over different areas, a total of four sites were surveyed. The accuracy investigation on the SfM-photogrammetry DEMs quality allowed to highlight the limitations and the potential of this method for multitemporal analysis in remote alpine area and thus to assess an applicability range for future realistic case scenarios.

1.1 CONTRIBUTION OF THE THESIS

The overarching aims of this research are to provide practical applications of terrestrial photogrammetry conducting a quantitative assessment of the capabilities of the SfM-photogrammetry approach for glaciological studies and identifying the main practical issues of a photogrammetric survey to reconstruct complex alpine terrain and object feature. The thesis is focused on the terrestrial image acquisition and different study areas with different ground-survey characteristics were identified. The primary goal of the photogrammetric surveys was to obtain the optimum balance between the cost, the time and the risks associated with the ground image capturing and the need to maximize the quality of the generated DEMs based on the final objectives and on the available human and economic resources.

The research objectives for this dissertation were twofold, related to the two main chapters in this volume.

The first objective was to validate the capability of a ground SfM-photogrammetry survey to reconstruct a surface by dealing with the main practical issues of a ground acquisition and by highlighting the main source errors which may be present within the field data. For this purpose, a test field area was identified, and the final accuracy of the 3D model according to the cameras network geometry (i.e. camera positions, number of overlapping images, camera-object distance), the camera acquisition by proposing a different image acquisition strategy based on panorama images and the georeferencing procedure, was analysed.

The second objective was to test the SfM approach for monitoring glacial and periglacial processing highlighting the limitation and the potential of the method for these applications. Three case studies were identified for the research project: Montasio Occidentale Glacier (Eastern Italian Alps), La Mare Glacier and neighbouring rock glacier in the Ortles Cevedale Group. The aim was to obtain, from multitemporal terrestrial photogrammetric surveys, using a common digital reflex camera, DEMs accuracies and resolutions sufficient for the calculation of the glacier mass balance (Montasio Occidentale and La Mare glacier case studies), and for the detection of the surface displacement of the rock glacier. For each of these study areas, the main factors that affect the accuracy of the photogrammetric DEMs were investigated and the relevance of these factors for the interpretation of glacial and periglacial analysis were discussed.

According to these main objectives the following research questions are posed:

Geomorphological application (Chapter 3)

- Which are the main issues of a ground SfM-survey?
- How accurate, precise and replicable are the topographic dataset generated using a ground SfM-photogrammetry approach in a different geomorphological context?
- How the DEM obtained using the SfM-photogrammetry compare with those obtained by terrestrial laser scanning in term of accuracy and resolution?
- How the panorama images acquisition improve the SfM-photogrammetry quality and which are the advantages of this acquisition strategy?

Glacial and periglacial application (Chapter 4)

- Which is the contribution of SfM-photogrammetry in glacial and periglacial applications in comparison to the other technologies?
- Which are the main issues on these applications and the main error sources that affect the quality of the SfM-reconstruction?
- Is the SfM-photogrammetry applicable to monitoring glacial and periglacial processes, how accurate and repeatable are the results in comparison to the LiDAR technologies and how much 'effort' is required to achieve that accuracy compared to alternative methods?
- How the accuracies and resolutions change according to different ground survey characteristics?

Data collected from field sites are used to address these research questions. This research will contribute to several fields related to the terrestrial SfM-photogrammetry applications for 3D and 4D (i.e. of environmental dynamics) earth-surface reconstruction. The investigated method provides a cheaper, easily adoptable and accurate alternative for reconstructing surface and estimating the surface change. A practical guideline for a ground-based imagery collection according to the desired accuracy and resolution is defined. Furthermore, a different method for data collection has been proposed and tested. This method can provide suggestions for further researcher and applications in similar contexts. By determining the inherent error and uncertainty in SfM-photogrammetry datasets according to different ground-survey characteristics, geomorphologists or others users will have a better understanding of the limitations and potential of the method. An overview of the thesis structure and the research sites is presented below.

1.2 THESIS OUTLINE

This thesis is composed of five chapters and is structured according to Figure 1.1. Chapter 3 and Chapter 4 represents the core of the PhD research, by describing the quality estimation of the SfM-photogrammetry in a test filed area and the application of the method in glacial and periglacial environments. These Chapters include a background section, and for each study site a detailed description of the area, the methods, the results and discussion. Certain results have already been published (or submitted) in scientific journals. All references, are at the bottom of the thesis but corresponding Figures and Tables are listed in the text with a progressive number according to the number of Chapter.

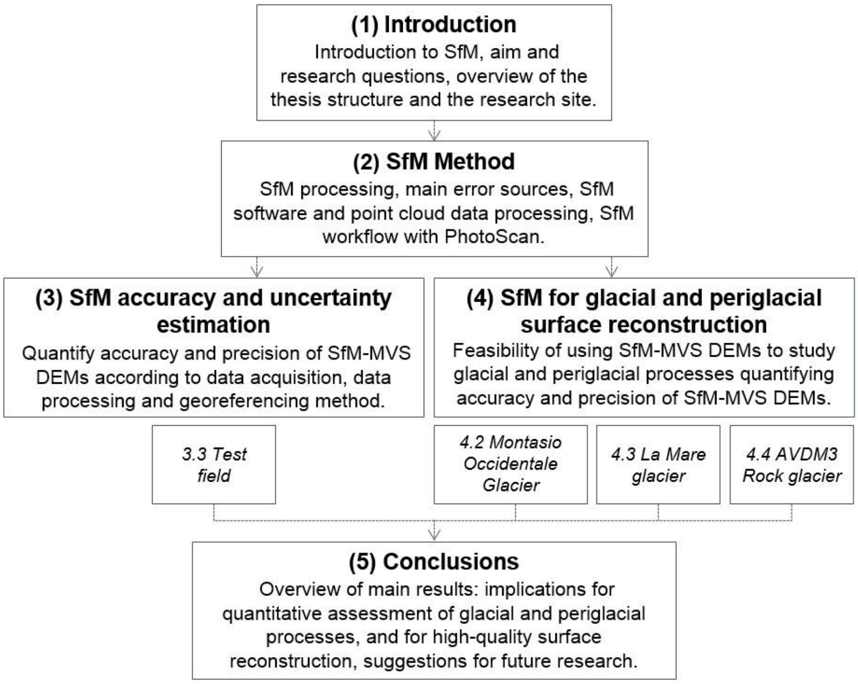

Figure 1.1 Overview of the Thesis structure.

The thesis is organized as follows:

Chapter 2 provided with a description of the SfM method and the main algorithm that composed the photogrammetric approach. Then, a description of the available software is also provide with a detail description of the commercial software Agisoft PhotoScan (AgiSoft LLC 2010a and 2010b) used in this work and of the SfM-photogrammetry processing workflow of PhotoScan (PS).

Within Chapter 3, the main source errors that affect the 3D SfM-photogrammetry reconstruction are described by summarising the results published in literature in this respect. The quality analysis of the SfM-photogrammetry was performed in a test filed area. In particular the camera network geometry and the georeferencing methods were investigated as they represent the main practical challenges for a terrestrial photogrammetric survey. Possible solutions regarding these issues were tested and discussed.

Within Chapter 4, the capability of the SfM approach to reconstruct two glaciers and a rock glacier surface is assessed. Understanding the sources and magnitude of error and SfM uncertainty is important to interpret the results about glacial (i.e. mass balance) and periglacial (surface movements) processes.

Chapter 5 summarizes the main results from all applications and analysis and presents the synthesis. Based on the study results, this chapter answers the fundamental questions of this PhD research and also lists potential further research following this project.

1.3 STUDY AREA

The main characteristics of the study sites is provided in Table 1.1. A detail descriptions of each area are in the corresponding paragraphs. The investigation on the photo-based approach was carried out in a test-area located at Torrente Val Montina, Perarolo di Cadore (Italy). This site was chosen as it provided an interesting morphological context, with different coverage types, (i.e. gravel river debris of different sizes and ground covered by vegetation, trees and shrubs) and it allowed to acquire the images at different distances, the positioning of artificial targets used as control measurements and an easy surveying with TLS used as benchmark.

Table 1.1. Main characteristics of study sites divided by chapters.

	Study sites			
	Chapter 3	**Chapter 4**		
Characteristics	*Test-field*	*Montasio Occidentale Glacier*	*La Mare Glacier*	*AVDM3 Rock Glacier*
Location	Perarolo di Cadore (Italy)	Italian Julian Alps (Italy)	Eastern Italian Alps (Italy)	Eastern Italian Alps (Italy)
Dimension [km^2]	0.0073	0.068	2.11	0.058
Elevation [m a.s.l.]	558 - 608	1860 - 2050	2660 - 3590	2943 - 3085
SfM survey data	4 Aug. 2014	5 Oct. 2012 26 Sept. 2013 25 Oct. 2014	4 Sept. 2013 27 Sept. 2014	27 Sept. 2014
Accessibility	Partially (inside)	Partially (inside)	None	Partially (inside/ outside)
Covered type	Gravel, grass, shrubs	Snow-firn, ice, debris	Fresh snow, firn, ice, debris	Rock
Reference data	TLS Total Station GPS (4 Aug. 2014)	TLS (5 Oct. 2012 26 Sept. 2013) GPR (29 Oct. 2014)	ALS (17 Sept. 2003 22 Sept.2013 24 Sept. 2014)	ALS (17 Sept. 2003 22 Sept.2013 24 Sept. 2014)

To investigate the potential of the SfM-photogrammetry in glacial and periglacial environment three sites with different ground-survey characteristics (Table 1.1) in terms of accessibility, extension of the object, and surface morphology with the presence of different substrata (snow, firn, fresh snow, debris and rock covered of variable grain size) were surveyed. These pilot studies complement previous investigations on the areas performed with LiDAR (both terrestrial and aerial laser scanning), Ground Penetrating Radar (GPR), and field measurements (Carturan et al., 2013b, 2013c, Seppi et al., 2013). Therefore a comparison between SfM-photogrammetry and other survey technologies for monitoring glacial and periglacial environments was performed in terms of accuracy and precision for multitemporal analysis, resolution, costs and operability.

2

STRUCTURE-FROM-MOTION

2.1 SFM-PHOTOGRAMMETRY: STATE OF THE ART

Several tools and methods for obtaining information about the 3D geometry of scenes from 2D views using techniques developed in the field of photogrammetry exist (Verhoeven et al., 2012). In traditional photogrammetry, two overlapping images (a stereo pair) are taken with a calibrated (metric) camera(s). By knowing the internal camera geometry, lens distortions, and the distance between photos (parallax), the stereo perspective allows users to calculate the distance from the camera to objects in the photographs using trigonometry. The downside of this type of photogrammetry is that users need a priori knowledge of the exact camera positions, or the 3D location of a set of control points located in the scene of interest, the internal camera geometry, and lens distortions to reconstruct a three-dimensional dataset of the scene. Moreover, achievable spatial resolution is a function of the pixel size and the accuracy is reduced with increasing the distance between the camera and object of interest. But fine resolution and accurate (mm-scale) topography can be obtain at range of several metres (close-range photogrammetry). However, the main disadvantages of conventional photogrammetry are the degree of expertise required, the difficulty and expensive to obtain a large amount of data, and the relative flexibility of the image geometry (e.g. degree of overlap).

The Structure from Motion approach represents the last evolution of the photogrammetry although the origins of the approach are from the field of computer vision, beginning with Ullman (1979) and evolving into the current iterations of algorithms (Snavely, 2006, 2008; Furukawa and Ponce, 2010). The SfM is characterized by the combination of the algorithm of photogrammetry as bundle adjustment and automatic algorithms from computer vision as feature detection. Both computer-vision and photogrammetry researchers showed the interest in the features extraction algorithms as a tool to automatically obtain stable points simply from the texture of the photographed object. The emergence of these algorithms has made it possible to develop SfM software that allowed to obtain, in a totally automatic, 3D information of the photographed object from a sequence of overlapping images, taken with a common digital camera (Fig. 2.1). From the homologous points that link the images, SfM uses bundle adjustment algorithm to simultaneously estimate 3D geometry (or structure) of a scene, the different camera poses and orientation (extrinsic orientation) and the camera calibration parameters (intrinsic orientation). Conventional photogrammetry shares these steps, however SfM is able to calculate the relative camera positions without needs to be known a priori the exact cameras locations. A non-metric camera can be used to collect imagery, which reduces the cost of collecting imagery. Where camera calibration parameters are unavailable (self-calibration), the internal camera geometry estimation (e.g. focal length, skew, principal point) and lens distortions are estimated starting from the image EXIF details. Additionally, SfM approach, instead of using two overlapping images, uses multiple (three or more) images to solve the trigonometry and extract the three-dimensional dataset that help reduce the error in each 3D point that comes from the simplified camera and lens geometries models.

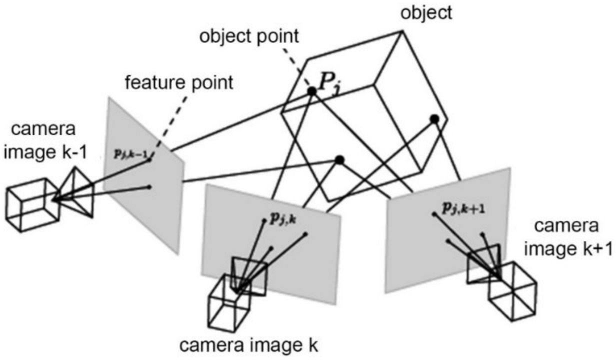

Figure 2.1. The SfM concept, 3D model is reconstructed from a sequence of overlapping images by using feature detection and matching algorithm.

The crucial step to orient a set of overlapping images is the detection of a sufficient number of homologous points (called 'tie points') that link the different images. The general algorithms that composed the SfM workflow is described below.

1. Feature extraction

The identification of the tie points is fully automated in the SfM workflow and starts with the extraction of feature point (or 'keypoints') from each image using algorithms of feature detection. To be most useful for SfM the keypoints identification should be valid for images taken at relatively wide-baselines (i.e. different perspective) (Smith et al., 2015). While there are several methods for identifying feature (including SURF (Bay et al., 2008), ASIFT (Morel and Yu, 2009), BRIEF (Calonder et al., 2010)), the 'scale-invariant-feature-transformation' (SIFT) (Lowe, 2004) object recognition system is used most widely in SfM as provides features invariant to scale changes, rotations and partially invariant to illumination changes. The use of such algorithm allows to obtain, for each feature extracted, the descriptors (numerical vectors consist of 64 or 128 elements), which describe the trend of the gradient in the neighbourhood of point.

2. Feature matching (keypoint correspondence)

The calculation of the Euclidean distance is one of the methods used to determine how similar two descriptors are. In practice, fixed a descriptor is on one image, the search of the homologue descriptor closest resembling to this on other images is started. The problem can be traced to search the nearest neighbour in an n-dimensional space (where n is the size of the descriptor). In such high dimensional space, Euclidean nearest neighbour search is computationally demanding (Arya et al., 1998) and the computational complexity is closely related to the size of the search space. K-dimensional trees (or *k-d* trees, Bentley, 1975; Friedman et al., 1977) are applied as an efficient solution to this problem. To reduce computation time algorithms less precise but much more efficient in the identification of the nearest neighbour have been developed and they are based on an approach called 'Approximate Nearest Neighbour' (ANN) (Arya and Mount, 1993). A further optimization of the latter approach, for searches in high dimensions spaces, has been developed and implemented by Lowe, named 'Fast Library for Approximate Nearest Neighbour' (FLANN) (Muja and Lowe, 2009). Regardless of the algorithm used, it is incorrect to classify the nearest neighbour as a homologue points. This classification shall be lawful only if the distance between the descriptor of the fixed keypoints and the nearest neighbour is less than a predetermined threshold. Brown and Lowe (2003) suggest using a maximum threshold of 0.6. Snavely et al. (2008) specified a minimum value of 0.8 to increase the number of matches.

It is apparent that the matching of the extracted feature points (i.e. comparison between descriptors) is the most relevant task of the whole automatic process of camera orientation given that the subsequent calculations are based on those data. In this phase the correspondences (match points) are determined for couples of images by a comparison for similarity between descriptors.

3. Identifying geometrically consistent matches (outlier removal)

The detection of the match points provides a percentage of outliers that it is often not negligible and therefore a further filter of keypoint correspondences is then applied. Robust algorithm for determine outliers like RANSAC (RANdom SAmple Consensus) (Fischler and Bolles, 1981) are based on robust estimates of the mathematical model that describes the epipolar geometry (Fig. 2.2), starting from the set of matches identified by the feature matching. In an automatic orientation algorithm, the mathematical model that you want to estimate is the fundamental matrix, (F-matrix or essential matrix if the camera is calibrated). The F-matrix specifies the relationship between the two images and it allow to reconstruct the geometry of the scene up to a projective transformation where all points lying on a single line will remain aligned in this way (i.e. 'collinearity' is preserved) (Smith et al., 2015). Taking any image pair with multiple common keypoints, candidate F-matrices are evaluated using the RANSAC method in which keypoints used in the construction of the F-matrix are randomly sampled. Then the difference between the returned F-matrix and that returned by other sampled keypoints is computed (Smith et al., 2015). Beyond a threshold the keypoint is considered an outlier, then sampling is repeated on different subset until there is a 95% chance that the subset contains only inliers for which F-matrix is returned. Then, all the outliers are removed.

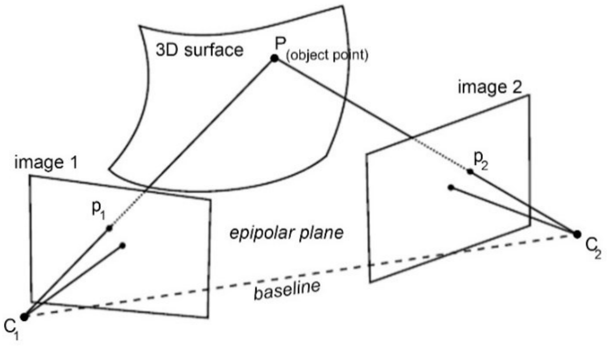

Figure 2.2. The epipolar geometry. The optical centre of the two images C_1 and C_2, an object point P, and the image point p_1 and p_2 of P all lie in the same plane (epipolar plane).

4. Propagation of correspondences

The valid matching points are then available for pairs of images, and in order to complete the phase of each camera orientation it is necessary to propagate the finding correspondences to the entire block of images.

5. Bundle adjustment

The correspondences extracted (tie points) from the entire image block are given as input to an algorithm of BA (Triggs et al., 1999) which has the task of calculating the orientations of each cameras at the time of image acquisition and the spatial coordinates of the tie points. This approach is a standard procedure in photogrammetry since 30 years, and has now been adopted by all software of automatic camera orientation. The BA is a least squares solution method for nonlinear systems. 'Bundle' refers to the bundles of light rays connecting camera centres to 3D points and 'adjustment' refers to the minimisation of a non-linear cost function which minimizes the reprojection error between the observed point and the projected image by varying the parameters of external orientation (and in some case internal) of the cameras. To solve this numerical solution the Levemberg-Marquardt is the most used algorithm. In the BA solution should be define a datum that means a reference system by imposing certain constraints which define the position of the origin in space, orientation and scale. Generally, software of automatic camera orientation adopt the solution free network adjustment. This means that the resulting 3D model has to be subsequently scale and roto-translated into an appropriate reference system. This is performed using a rigid seven parameter transformation, consisting of one scale factor which applies to all three dimension, three translation parameters in X, Y and Z, and three rotations parameters around the X-axis, Y-axis and Z-axis.

In classical photogrammetry it is preferred to fix the reference system and the scale by the use of GCPS (Ground control Points), in fact, the latter are generally included as observations within the BA procedures. As seven parameters must be determined to define a spatial reference system, a minimum of three GCPs well distributed in space is required; this approach is named *minimal constraints*.

In free-network there is no constraint in the model, while the presence of the GCPs significantly affect the BA operations by means of the constraints on the model. On the other hand, the final results are equivalent in the presence of a camera network geometry that allows to obtain redundant intersections and with angles of incidence close to 90°. Generally, automatic camera calibration using self-calibration is a standard in most of the image based dense matching tools available, whatever the kind of camera used, but detailed quality results from the adjustment are usually not available for the end use (Börlin et al., 2014). This approach allows to further minimize the reprojection error, but it can generate deformations on photogrammetric model.

The SfM algorithms, strictly speaking, refers to the steps described above and they can be summarised as following: identification and matching of homologues feature in overlapping photos, computation of camera calibration parameters for each image, relative orientation of camera positions and generation of a 3D sparse point cloud that represents the location of the tie points. At the end of the SfM approach the reconstructed scene is in an arbitrary coordinate system, meaning that the relative distances between camera locations and all of the 3D points are consistent, but not metric.

The reconstruction of a dense surface is executed by a dense matching algorithm (i.e. the correspondence information is determined for each pixel). Several dense matching algorithms have been proposed, as reviewed in Scharstein and Szeliski (2002), Seitz et al. (2006), Remondino et al. (2013). An exhaustive overview of the matching methods and algorithms implemented in the main software is provided by Ahmadabadian et al. (2013). "The first key point of different methods relies in the way the algorithm provide a dense number of points to guarantee a continuous reconstruction of the surface also in presence of sharp edges or low-texture area. The second key points is related to the robustness against outliers, which may be due to repeated patterns, poor contrast in the images, change of illumination image blur and noise or large perspective deformations" (Scaioni, 2015). Any dense matching technique are based on the minimization of a cost function that is built up on the basis of the intensity values. Many method also include some constraints coming from the know image mutual geometry (i.e., the external camera orientation) (Scaioni, 2015). Whereas SfM algorithms operate on a sparse set of feature points that are extracted from the source photographs, the dense reconstruction algorithms operate at the individual pixel scale (Seitz et al., 2006). As all pixels are employed for the detailed reconstruction of the scene, this step is the most computationally intensive step. The accuracy that can be obtainable is difficult to predict and to be evaluated because it depends on the large number of factors, as reported above (i.e. the quality and the texture of the images) (Grün, 2012).

At this stage, the reconstructed surface is still expressed in local coordinates and contains arbitrary units. In order to extract metric information of the reconstructed surface, in local or global-coordinate system, control data or a scale definition by using a known distance are required. Control data concerns whether ground control points, scale measurements, or 'direct' georeferencing from known camera positions used for datum definition. To perform multi-temporal analyses the dense point cloud needs to be georeferenced with reference to an absolute coordinate system. In general the georeferencing is obtained via the manual identification of control points with known coordinates in the photographs. A much larger number of control measurements then three is recommended (James and Robson, 2012), but this depend on the survey area (accessibility, size and morphology). They should cover the entire area and be well distributed throughout the area (Javernick et al., 2014).

2.2 SFM-PHOTOGRAMMETRY: SOFTWARE AND TOOLS

The general SfM-photogrammetry workflow to create a georeferenced 3D point cloud of the photographed object can be summarized in three-step: i) SfM procedure, ii) calculation of a dense 3D surface from reconstructed image network geometry using a dense image matching algorithm, and iii) georeferencing of the dense point cloud. This workflow is highly automated and different available software provide different user-control that in some case are limited to some pre-processing steps. The SfM photogrammetry packages ranging from web services to open-source and commercial software (Smith et al., 2015). Open source and web-based services software have played a significant role in the development of SfM photogrammetry approaches. Open source code packages are used regularly for SfM as the source code is available for modification and distribution; differently, freely-available packages are free to use but no source code is provide. The main web-based services includes Autodesk 123DCatch (www.123dapp.com/catch), Microsoft Photosynth (www.photosynth.net), and ARC3D (www.arc3d.be). These software are highly automated and post-processing operations are limited and require export to other software for processing or editing (e.g. CloudCompare (www.danielgm.net/cc). In the case of Photosynth the dense matching and the georeferencing step are not allowed and requires additional software. Snavely et al., (2006; 2008), Furukawa and Ponce (2010) provide the basis to implement one of the first open-source workflow for free SfM photogrammetry combining Bundler (www.cs.cornell.edu/snavely/bundler) for the sparse point cloud generation and PMVS2 (Patch based Multi-View Stereo, www.di.ens.fr/pmvs) for the dense cloud reconstruction in the SfMToolkit. Bundler does not provide a graphic unit interface (GUI) and for this reason the use is limited compared to commercially available alternatives. Therefore further contributors put their efforts in offering solutions based on GUI for image-based 3D reconstruction. The open source VisualSfM (http://ccwu.me/vsfm) combines a SfM algorithm and PMVS in a single user interface. Compared to other SfM packages, the open-source MicMac (www.micmac.ign.fr) comprises a full SfM workflow and it is focused on accuracy instead of automation, offering complex models of camera intrinsic parameters, and giving the possibility to include GCP information in the bundle adjustment step, yielding accurate results. This packages, originally developed for aerial image matching, became available to public since 2007 and then evolved to a more straightforward SfM pipeline, with further tools such as APERO (Pierrot-Deseilligny and Clery, 2011). On the one hand, the high degree of possible user-software interaction can be advantageous to adopt the 3D reconstruction to each specific case study, on the other hand it represents a drawback as further knowledge into the method are required. Only a few studies have used the software in geoscientific applications (Bretar et al., 2013; Stumpf et al., 2015; Ouèdraogo et al., 2014; Stöcker et al., 2015; Eltner and Schneider, 2015). Among available SfM software the commercial program PhotoScan, from AgiSoft LLC (AgiSoft LLC, 2010a and 2010b www.agisoft.com), is the most frequently applied SfM software, although it works as black box, and the processing step are currently limited. This is due to the user-friendly interface, ease of use thanks to the high automatism and quite lower prise compared to other photogrammetry commercial packages. In addition the software enables all operations for obtaining a georeferenced 3D model of the scene, included a mesh reconstruction, DEM and orthophoto. In the range of commercial tool Pix4DMapper (www.pix4d.com) is an emerging software used in several soil erosion application (Castillo et al., 2012; Eltner et al., 2013) and has been shown to perform well on bundle adjustment but less well on dense matching and orthophoto generation (Unger et al., 2014). Additional commercial packages like Eos PhotoModeler Scanner (www.photomodeler.co.uk), Autodesk image Modeler (www.autodesk.com/imagemodele), D-Sculptor (www.d-vw.com), 3DFZephir (www.3dflow.net) require more photogrammetric expertise.

The fast development of photogrammetric packages has determined a need of software open-source able to manage (visualizing and editing) the huge amount of data produced by the SfM technique. In this category the most common tools are Meshlab (http://meshlab.sourceforge.net) and CloudCompare (above).

2.2.1 SfM workflow with PhotoScan

The commercial software PhotoScan Pro (version 1.0.3, 1.1.5) was chosen to process the imagery collected at all sites as the software allows in one environment to complete all the operations necessary for exporting the dense point cloud of the photographed object in a global reference system. This section provide an overview of each step used to process the dataset. Details on the image processing results are given for each case study in the corresponding chapters.

The adopted workflow is summarised in Figure 2.3 and for each study area the SfM imagery procedure and pre/post-processing steps are reported in Table 2.1. The specifics workflow adopted for each study site is described in the corresponding chapter, and the related schemes are shown in Appendix A.

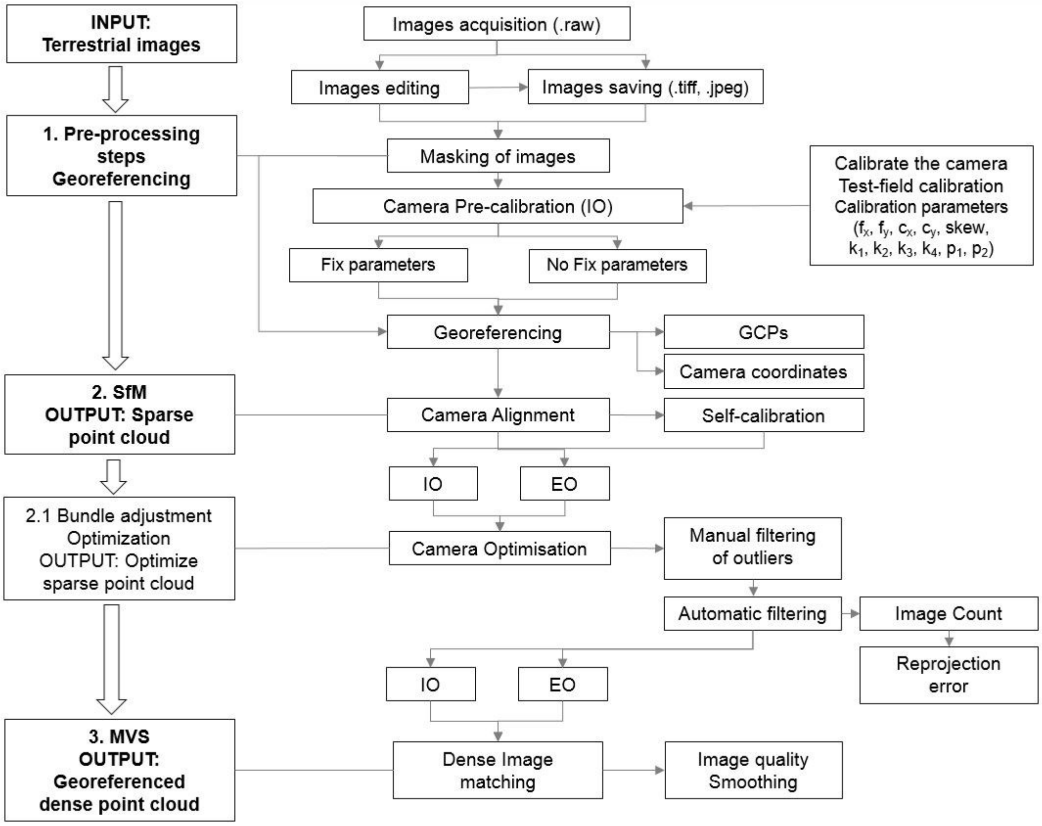

Figure 2.3. Image processing workflow with PhotoScan.

The key components of the used SfM photogrammetry in PS are: 1). ‘Marker’ identification on the images, 2). ‘Align images’ and ‘Optimization’ that means SfM processing and bundle adjustment optimization according to the reprojection error and the known control data (GCPs or camera positions) and 3). ‘Build geometry’ to reconstruct the dense point cloud with the Multi-View Stereo (MVS) algorithm. While the software is highly automated, a series of settings and intermediate processing steps allow to enhance the results of each of the three main steps and consequently different results according to the constraints imposed during the camera orientation and the imagery processing. However, the exact algorithm that are implemented in PhotoScan are not publicly known. The sets of images of the four case studies were acquired with different digital consumer camera and focal length under various illumination conditions. The images generated by the digital camera were stored as a RAW images in order to have the possibility to edit the images. To overcome the significant variability in brightness during the glacier surveys (Montasio Occidentale glacier and La Mare glacier study sites), the RAW images have been edited to adjust the exposure and contrast in order to retrieve information from the overexposed (e.g., snow-covered) areas and underexposed (e.g., shadowed) areas. These editing steps had a positive impact on the feature extraction performance but the impact of these development steps on the accuracy of the extracted feature points was not tested in this study. The RAW files (original or after editing) were saved as JPEG or TIFF files in the computer.

The process starts with the straightforward uploading of images into the Software. In the whole image sets, the non-stationary objects (e.g. clouds, strong shadows, and river), sky, and features lying in the distant background have been masked. The masked part of the photos are not taken into account while estimating camera positions and consequently, during the dense image matching computation.

Pre-processing step: masking of images, pre-calibration and georeferencing

The software allows to import camera calibration parameters. For accurate data extraction and due to the weak camera network geometry and the homogeneous texture of the surveyed terrains (i.e. La Mare glacier and AVDM3 Rock glacier case study), the camera has to be pre-calibrated in two SfM-photogrammetry applications (Table 2.1). Different calibration techniques can be used, usually based in a test field with signalized targets that can be set in a flat surface or even in a plotted sheet. In this work, the estimation of calibration parameters has been designed, after each survey, in a test field by acquiring an image dataset created for that purpose. The images were taken by setting the camera at the same way used in the survey: focal length, aperture, ISO, camera-object distance >10m. Both parallel and convergent image configurations were adopted for acquiring the images. The corner of a building was the object chosen to calibrate the cameras in order to have different depths and not a flat surface, and with a strong texture defined by irregular bricks. 12 black/white circular targets have been positioned on the surface and on the ground at different depths and their centres were measured with Total Station in a local coordinates system. The inner orientation parameters were estimated in PhotoScan using a self-calibrating bundle adjustment by including the measured GCPs into BA optimization. This strategy was chosen as each SfM tools provides different solutions for estimating the camera calibration. PS uses the Brown model (Brown 1966), to estimate the inner parameters (fx, fy, cx, cy, skew, k1, k2, k3, k4, p1, p2). Therefore, it is important that the calibration software used to estimate the parameters employs the same mathematical model (i.e. Brown) as the one used for bundle adjustment (Remondino et al., 2013). These estimated parameters where then used to orient the images of the study areas. Additionally, the estimated intrinsic parameters were kept constant during the entire SfM processing.

In this work, for each SfM application, the control measurements were included into the SfM process to avoid instability in the bundle adjustment solution (Verhoeven et al., 2015). PhotoScan supports setting a coordinate system based on either ground control point (marker) coordinates or camera coordinates. Different solution were adopted according to study area. For the practical case studies, the limited accessibility of the area and logistical problems have prevented the use of artificial targets as GCPs. Therefore they were selected as natural features in stable area outside the glaciers and rock glacier, and their coordinates were extracted from the ALS hillshaded DTM or from the TLS point cloud (see Table 2.1). Different georeferencing methods using natural feature, artificial target and directing georeferencing were compared in the test field area. To scale and georeferencing the data, markers were visually and manually identified on each photo where it was visible (on at least 2 photos). The software support a guided approach marker projection, means that automatically the software projects the corresponding ray onto the model surface and calculates marker projections on the rest of the photos where marker is visible. This guided marker placement usually speeds up the procedure of marker placement significantly and also reduces the chance of incorrect marker placement but the geometry of the scene (camera orientation) must be reconstructed (AgiSoft LLC 2010b). The GCPs (or camera coordinates) error estimates by the software is the average transformation residual error (i.e. the distance between the input and estimated positions of the GCPs).

Align images and optimization, SfM step

PhotoScan estimates internal and external camera orientation parameters during photo alignment starting from the data EXIF of the photos. This estimation was performed using image data and the control measurements, following the criteria adopted in this work. However, the optimization procedure implemented in PhotoScan was required to refine both the IO and EO minimizing the sum of reprojection error and reference coordinate misalignment error. The optimization was performed by removing outliers and incorrect matches from the sparse point cloud. Firstly, by means a manual removal of obviously mislocated points of the sparse point cloud. Then, point representing high amount of noise were removed automatically according to the "Image Count" (number of images that view the reconstructed point, two is the minimum) and the "reprojection error". The latter is expressed in pixels by PhotoScan and reports the accuracy of the match point positioning in the image space (average and maximum values) after the photograph alignment step. High reprojection error usually indicates poor localization accuracy of the corresponding point projections at the point matching step. It is also typical for false matches (AgiSoft LLC 2010b).

Geometry building, dense image matching

The dense image matching performed with the MVS algorithm is the step that requires more memory and processing time that depends on the number of images, their resolution and the extension of area to reconstruct. Therefore the user can chose the images resolution (called in the software "quality") for the dense matching computation halving the original dimension (i.e. 'Ultra-High' means full resolution). The imagery sampling affects the resolution of the dense point cloud (point density), and slightly also the accuracy of the point cloud as investigated in this work. Additionally, different smoothing filtering can be selected for generating the dense points. The filters are divided into Aggressive, Moderate and Mild, but any explanation is described in the manual about these filters. In the SfM applications the "mild" smoothing filter was adopted to preserve as much spatial information as possible and the three filters were compared in the test field area.

Following the dense point cloud reconstruction, PS supports the reconstruction of rasterized DEMs and the 3D model texturing by the raw image pixel value. However, these steps are not part of the adopted methodology with the exception of the orthophoto generation that can be exported only after the 3D model (mesh) reconstruction. The output exported from PS was a dense point cloud in .txt format with the information of X, Y, Z coordinates, R, G, B, and normal vector for each point. For comparison purpose with the reference LiDAR data, DEMs (both LiDAR and SfM) were produced in GIS environment using the same interpolation method (Natural Neighbour interpolation).

Table 2.1. Imagery processing with PS for each study sites.

	Study sites			
SfM processing	*Test-field*	*Montasio Occidentale Glacier*	*La Mare Glacier*	*AVDM3 Rock Glacier*
Images acquisition	single images panorama images	single images	panorama images	single images
Image editing	-	✓	✓	-
PhotoScan pre- processing step				
Mask images	✓	✓	✓	✓
Pre-calibration	-	-	✓	✓
Georeferencing	artificial GCPs natural GCPs directing georeferencing	natural GCPs (TLS point cloud)	natural GCPs (ALS DEM)	natural GCPs (ALS DEM)
PhotoScan processing step				
BA-Optimization	✓	✓	✓	✓
Dense matching quality	Ultra-high High Medium	Ultra-high Medium	Ultra-high High	High
Orthophoto	-	✓	✓	✓
Post – processing of dense point cloud				
Filtering of noise	-	✓	✓	✓
Sub-sampled	-	✓	✓	✓

3

ACCURACY, UNCERTAINTY, AND REPEATABILITY OF SfM

The 3D data collection technique cannot be correctly performed without understanding its behaviour and potential and unknowing what accuracy and data quality is attainable under certain conditions (Remondino et al., 2013). To create 3D data starting from the field measurement performed with a passive sensor one fundamental properties of the collected data is the sampling resolution, i.e. the minimum distance between two consecutive measurements that is given by the image Ground Sampling Distance (GSD). Using photogrammetry theory, a rough estimation about achievable accuracy attained from SfM-photogrammetry can be estimate a priori according to the pixel size, the adopted focal length and the distance to the target object.

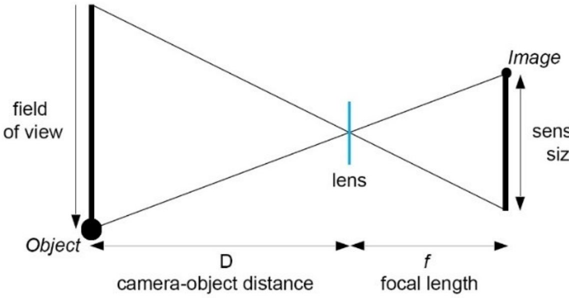

Figure 3.1. Relationship between focal Length, FOV, Sensor Size, and working distance.

The ratio between the scale of the image and the scale of the object is the same as the ratio between the camera-object distance *D* and the focal length *f*. The distance in case of terrestrial acquisition is defined by depth. Therefore, the ratio between the size of a pixel (defined by the camera used) on the image sensor and the size of a pixel on the object is also the same ratio (Fig. 3.1) and mathematically is expressed as:

$$pixelsize_{ground} = (D/f) \times pixelsize_{image} \tag{3.1}$$

For traditional stereo photogrammetry, by knowing the accuracy in terms of pixels in the image sensor, σ_i, the planimetric accuracy on the ground is defined as:

$$\sigma_{plan} = \sigma_i \times pixelsize_{ground} \tag{3.2}$$

This formula represents the accuracy in the plane that is parallel to the image sensor. The precision of depth (or "height", for aerial photography), σ_{depth}, for a point from a stereo measurements, in relation to the measurement accuracy in image space σ_{pixel} can be expressed as:

$$\sigma_{depth} = \frac{D}{B} \times \sigma_{plan} \qquad (3.3)$$

where B is the baseline, i.e. the distance between the camera centers (the stereo base).

A different formula was defined by Fraser (1996) to estimate the achievable coordinate precision, σ_c for individual points viewed in k images for convergent imagery:

$$\sigma_c = \frac{q\bar{D}}{\sqrt{k}\,d}\ \sigma_i \qquad (3.4)$$

where q is a factor that represents the strength of a photogrammetric network geometry, $\bar{D}$ is the mean distance from the camera to a target and d is the principle distance of the camera (a measurement similar to focal length).

Consequently, the precision of the photogrammetric measurement mainly depend on f/D, which represents the image scale and B/D, which represents the intersection angle (or base-distance ratio). The precision of image measurements σ_i is generally a sub-pixel value that range from 0.5 to 0.1 pixel. This value depends on a few factors, like the quality of the images (noise and blur) and the accuracy of the camera calibration. The images accuracy can be described as "uncertainty in the precise location of a point in an image". This uncertainty in the point's location translates into an uncertainty in the direction of the ray that we project from that point, through the perspective centre, into the scene.

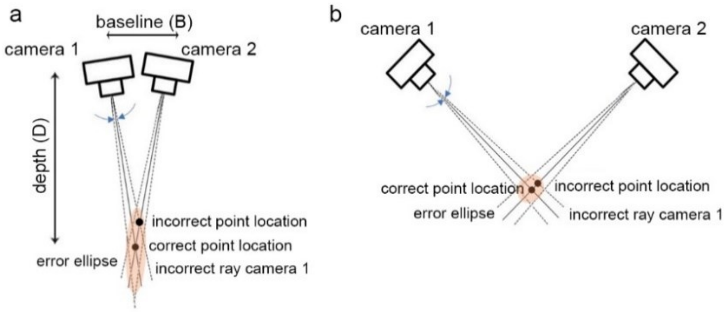

Figure 3.2. Intersection geometry and error plot. a) Weak intersection with small base\depth ratio; b) Strong intersection with large base\depth ratio.

An approach to reduce the absolute error in the XYZ coordinates is to have a smaller image point error (Fraser, 1996). In Figure 3.2, the dashed lines illustrate the range of possible ray directions associated with the range of possible locations within each image for each point, The possible intersection locations in the object space is roughly elliptical and can be defined with an "error ellipse". The "planimetric accuracy" is uncertainty in the plane that cuts the ellipse at right angles to the view direction, and "depth accuracy" is uncertainty in the long axis of the ellipse. By moving the cameras further apart, i.e. by increasing the base-distance ratio (Fig. 3.2b), it's apparent that the ellipse becomes more circular and thus the distance accuracy is improved. The optimal geometric condition are for intersection angle close to 90°. The acceptable B/D ratio to achieve high accuracy ranges from 0.16 to 0.5 or even higher. Generally, the depth error increases significantly when the B/D ratio decrease below 0.3.

The accuracy based mainly on the based-distance ratio has been extensively studied (Kraus, 1997; Munkelt et al., 2007). A good B/D (i.e. large intersection angle) and large image scale (wide angle lens) ensure high depth accuracy and are used to cover large area. However, for the Structure from Motion applications, large baseline models have lower image similarity which is challenging for the matching method providing lower completeness and point density and an increase amount of outliers since the matching fails more likely. Contrary, small intersection angles and image scale lead to high completeness due to high image similarity and the good matching performance, but also poor depth precision due to the weak geometrical conditions (Wenzel et al., 2013). Smaller baseline are allowed to achieve good depth (Z) accuracy for accuracy image precision like 0.1 pixel (Delon and Rougé, 2007).

According to the required depth precision, image scale and intersection angle should be chosen. In the following two sections the main error sources and concept behind the quality of the Structure form Motion are briefly covered. Background theory and application of SfM is given with a geoscience focus.

3.1 SFM PHOTOGRAMMETRY: ERROR SOURCES

The SfM-photogrammetry is considered the ideal means to yield photorealistic and accurate digital reconstructions of real-world objects in a fast and straightforward way. However, special care should be taken while planning the photogrammetric survey to optimize the 3D model quality (i.e. accuracy and uncertainty) and spatial coverage. Investigations on error sources of SfM-photogrammetry are provided in several papers, including (Micheletti et al., 2014; Nocerino et al., 2014; Bemis et al., 2014; James and Robson, 2014). The accuracy of SfM-photogrammetry model depends upon three main factors: i) the network geometry, (i.e. number of photos, intersection angle, percentage of overlapping, and the presence of convergent views), ii) the image quality (i.e. imagery resolution, sharpness and light conditions during photos acquisition, and surface texture), iii) the distribution and precision of the control data concerns whether ground control points (GCPs), scale measurements, or camera positions used for datum definition. In addition, different accuracies can be obtained according to the method used to the accuracy assessment, the platform used to capture the images (both terrestrial and aerial), the image processing and software used (i.e. camera calibration parameters, accuracy and distribution of matching points) and the nature and complexity of the study object (see Section 3.2).

Camera network geometry

In photogrammetry, camera network geometry is denoted as the imaging setting specifying the number of overlapping images, percentage of image overlaps, the obliqueness and convergence of the view, the shooting distance, the baseline and therefore the camera intersection angles between images that view the same points and angle of incidence with the surface, such that an accurate 3D scene can be reconstructed. Design of the imaging network in accordance with the required accuracy, resolution and completeness is still a challenging task in photogrammetry (Wenzel et al., 2013; Alsadik et al., 2013; Nocerino et al., 2013).

The accuracy of the results directly depends on the number of frames provided to the software. To ensure accuracy, each point on the object should be visible in at least two images but generally, additional frames imply more accurate models. Micheletti et al. (2014) in a laboratory experiment has decreased the median distance errors of models from 0.171 mm to 0.114 mm adding one frame (from seven to eight frames). The addition of on frame when using the minimum number of images can considerably increase the model accuracy. Nonetheless, no a linear trend exists between achievable accuracy and the number of used images and the relation is likely to differ from case to case (Micheletti et al., 2014). Moreover, when the number of images is already sufficient for a good representation of the surface of interest, the benefit of redundancy seems to affect the outliers rather than accuracy improvement (Rumpler et al., 2014). The decrease of noise of the surface data for redundant measurement, is provided by highly overlapping imagery, which enables the rejection of outliers during the surface reconstruction and minimises the risk of data gaps (Wenzel et al., 2013). However, the issue to find the minimum number of cameras (i.e. filtering out cameras that are redundant to reduce computation time) in an optimal configuration, which guarantees the sufficient coverage and accuracy in the object space is beginning to be investigated (Alsadik et al., 2013)

The baseline and ray intersection geometry on feature matching have a higher influence on the resulting accuracy than the redundancy in image acquisition (Rumpler et al., 2014). As introduce in the section before, a weak photogrammetric block design reduces the ability of automated feature matching to identify reliably corresponding features in overlapping images affecting the final accuracy and completeness of the 3D model. Additionally, a wrong photogrammetric planning can lead to a general deformation ('bending' or 'doming' effect) in the 3D results (Nocerino et al., 2014). This effect can appear especially in case of open sequence of images like a single strip of a flat object (e.g. small depth as wall or façade). The inclusion of convergent images (Fig. 3.3), more typical for terrestrial data collection rather than aerial configuration where a parallel axes schemes prevails, strengthen considerably the network geometry and help to avoid global deformation of the image-based 3D results (Nocerino et al., 2014). The capture of convergent imagery allow also reconstruction of surfaces with a complex morphology.

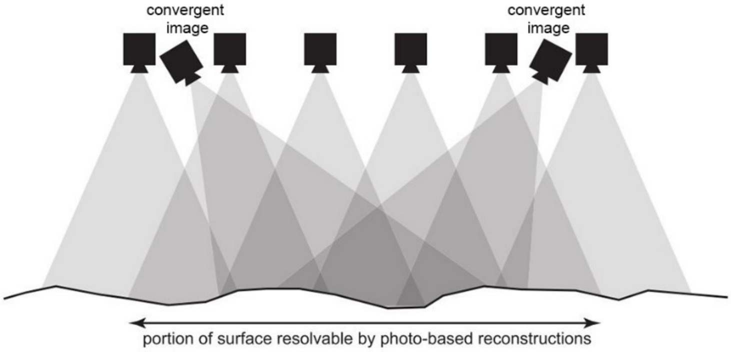

Figure 3.3. Illustration of parallel versus convergent camera orientation.

The distance between the camera and the study object (depth) is an important parameter in the camera placement objective as a strong correlation exist between the measurements error and the shooting distance. Dai et al., (2013), Rumpler et al., (2014) demonstrated that the measurements error increases with increasing the distance to the object, as reasonable hypothesis given by the Equation 3.1, which highlighted the relation between the precision with the image scale and intersection angle. James and Robson (2012) demonstrated that for many geoscience applications, the surface precisions are around 1:1000 (i.e. a precision of ±1 mm for every 1 m of viewing distance). In general, the maximum distance between the camera and the object has to be planned according to the required object minimum resolution or ground simple distance (GSD). However, in practical applications, the shooting distance is strongly influenced by the scene (space available between the camera and the object, accessibility to the area and occlusions) that differ from case to case and often a proper planning is infeasible.

Camera calibration

Larger focal length lead to higher resolution models but as general rule, twice the number of photographs required increasing the processing time (Bemis et al., 2014). In general, wide angle-lenses (equivalent to 35mm on traditional SLR) are most easily to calibrate compare to longer lenses (>55mm), fisheye that required specific calibration models (Micusik and Pajdla, 2006), or ultra-wide angle lens i.e. GoPro camera type.

Image quality

The capability to identified homologues image points are related to texture (i.e. the level of contrast in the imagery) of the feature to be modelled, the sharpness and resolution of the images. Image contents, which cannot be enhanced substantially because depends by the photographed object, are the primary factors controlling the success of image-matching (Grün, 2012). The quality of SfM-photogrammetry results depends significantly on the image-matching performance (Grün, 2012; Dall'Asta et al., 2015) either during camera orientation and subsequent dense-matching when 3D information is calculated for almost every pixel. A low image texture, like snow covered glaciers

(Gómez-Gutiérrez et al., 2014a) or sandy beach (Mancini et al., 2013), generates more uncertain point qualities, and lower density of the point clouds due to lower performance of dense image matching algorithm. The point density is influenced on the sharpness and the resolution of the photo dataset in addition to the texture (Westoby et al., 2012). The lower contrast caused by under or over-exposure during the images acquisition is another error sources in the reconstructed point cloud, although Gómez-Gutiérrez et al., (2015) demonstrated that HDR acquisition not improved significantly the final accuracy. Gómez-Gutiérrez (2014a) achieved highest errors in the shadow areas, and Bemis et al., (2014) highlighted the issue of the duration of the survey because the sun's azimuth continues to change during the survey and therefore the matching of the points between the images becomes complicated by changes in shadow length. In general high resolution dataset are preferred to low resolution since details and large disparity variations can be preserved. However, comparison between simple low-cost cameras (such as compact camera or those embedded in smartphone) and SLRs digital camera do not show significant differences in point cloud quality at short ranges (Micheletti et al., 2014; Thoeni et al., 2014). Additionally, Thoeni et al., 2014 has achieved higher accuracy and biggest GSD with a camera of lower resolution, probably due to the higher quality of CCD image sensor. For longer survey ranges, i.e. >100 m image resolution and sharpness becomes more important (Smith et al., 2015).

Control measurements

For scaling and georeferencing the SfM-photogrammetry model control measurements based on visible targets (GCPs) that can be identified in the images is the most applied method GCPs. Scale measurements, or camera positions can also be used for datum definition. Targets should be placed on stable features and be visible in as many images as possible (Smith et al., 2015). Several studies demonstrated that control points are not only necessary to scale the model but also to compensate for non-linear model misalignment (James and Robsons, 2012; Remodino et al., 2013; Nocerino et al., 2014; Thoeni et al., 2014). A minimum of three GCP (four is recommended) are necessary for the datum definition. However, is the distribution of the control data through the area of interest that determines the quality of the final model and can help to reduce the model distortion (James and Robsons, 2014). Nocerino et al. (2014) showed that the free network (without GCPs into the bundle adjustment) provided the lowest standard deviation of the object points, while in the constrained solution (with GCPs) the standard deviation of the points uniformly increase accordingly to the accuracy of the employed GCPs. Therefore, the scaling operation by GCPs must be performed during the image triangulation step (bundle adjustment) and not a-posteriori (once the 3D model is obtained) otherwise possible image block or model deformations cannot be compensated (Remodino et al., 2012). Increasing the number of GCPs do not significantly improve the results of the bundle (Nocerino et al., 2014). GCPs should ideally cover both margins and the centre of the scene (Bemis et al., 2014) and a linear configuration should be avoid. SfM-photogrammetry

3D model should be georeferenced only with high accuracy surveyed ground control point (i.e. by means total station or RTK-dGPS) in order to reduce the error introduced into the data set, in particular if the control measurements are included into the camera orientation optimization (Dietrich, 2015). In case of limited GCP accuracy, the ICP algorithm provided to be a valuable tool to resolve residual alignment errors and to ensure that the coordinate system alignment is as tight as possible (Micheletti et al., 2014; Johnson et al., 2014; Stumpf et al., 2015). ICP works iteratively to find the rigid body transformation (translation and rotation) that minimizes the spatial difference between the two point clouds (Chen and Medioni, 1992). However, this step helps account for remaining differences in the global registration of the two data sets that result from changes in absolute GPS positioning between the two surveys, but does not affect the internal shape of either data set (Johnson et al., 2014).

Systematic error and bending effect due to poor planning of a camera network and due to camera factors.

In measurements, the systematic error is a bias that occurs consistently (Viswanathan, 2005), resulting from inaccuracy of a system as one observe or measures. For image-based system, the systematic error can be derived from the camera characteristics (i.e. the lens distortion and the approximated principal distance) and a poor planning of camera network geometry (Dai et al., 2014). For modern digital camera, the camera lens distortion can be taken as the aggregate of the radial distortion and the decentering distortion (Beyer et al., 1995; Fraser, 1996). The latter is caused by the presence of a combination of lenses and therefore the centers of those lens elements cannot be strictly collinear, giving rise to decentering distortion. The radial lens distortion occur in each lens and the distortion effect is magnified along the radial direction of the lens: The further a point lies on the border of the lens, larger is the error in the projected image point. The systematic error caused by these factors can be minimized through camera calibration.

Wackrow and Chandler in 2008 identified significant dependency of the systematic error on the lens model but also in the imaging configuration, demonstrated that oblique convergent imagery can minimize the remaining systematic error caused by slightly inaccurately estimated lens distortion parameters (Wackrow and Chandler, 2008, 2011). The increasing application of SfM-photogrammetry for reconstructing large-scale scenes has promoted researcher to investigate the connection with the geometry of camera network and the systematic error of measurements. Several studies have revealed that the accuracy of the network increases with the increase of converge angle of camera, the number of intersection rays to an object point and the intersection angles (Remondino and Fraser, 2006; Wenzel et al., 2013; James and Robsons, 2014; Nocerino et al., 2014; Micheletti et al., 2014). According to this, in case of UAV (or similar) surveys where the camera base is parallel to the object plane and the optical axis of the camera intersects the object plane orthogonally, oblique convergence imagery have to be acquired. In fact, for image sets with near parallel viewing directions, self-calibration bundle adjustment (normally used in SfM-photogrammetry based reconstruction) will not able to derive radial lens distortion accurately, and will give associated systematic 'doming' DEM deformation (James and Robson, 2014; Dietrich, 2015). If an accurate camera model is available, then self-calibration is not required and systematic error should be negligible (James and Robson, 2014). If oblique imagery are not available or difficult to acquire, as in case of fixed-wings UAV platform, control points should be widely distributed, covering both the survey centre and peripheral regions, enabling radial z-error plots to be generated. However, Javernick et al. (2014) by including control points in the bundle adjustment were able to reduce z-error to the decimetre level, but evidence of systematic error was remained.

Practical guidance for a SfM-photogrammetry survey planning

As describe above resolution accuracy and uncertainty of the SfM-photogrammetry 3D reconstruction are dependent upon a number of parameters. Planning of SfM-photogrammetry survey must consider the required GSD, the point accuracy and their resolution, the site characteristics and constraints (distance, dimension, type of covered), the available equipment (type of camera and lenses), illumination issues, and presence of occlusion (e.g. rock masses or vegetation). Several recent publications compared image-based technique with range-based technologies demonstrating that both technologies are capable for providing similar accuracy and resolution when supported by a well-designed plan (Remondino et al., 2013).

Practical guidelines for acquisition planning with buildings, and cultural object can be found in Wenzel et al. (2013) and Remondino et al. (2013). Suggestions on the practise for photograph collection in order to obtain optimal results in natural environment are provided by Favalli et al. (2012); James and Robson (2012); Westoby et al. (2012); Bemis et al. (2014); Micheletti et al. (2014); Smith et al. (2015), and Stumpf et al. (2015).

Firstly, a reconnaissance tour on the site is one of the first task that should be undertaken in order to create valuable information that can influence decisions related to the set-up and data collection, as well as in addressing safety issue and then choose the right equipment and platform (i.e. handheld camera, aerial like UAV, or the combination of both). Summarising the results published in literature the following practical guidance should be while planning of SfM-photogrammetry data acquisition.

Camera network geometry design and data acquisition

- Plan the image GSD in accordance with the project needs and employed sensor and then consequently, the distance between the camera and the object, which is subject to the user-defined resolution accuracy, and camera field of view.
- The distance between overlapping camera that view the same points must be chose according to the B/D ratio by ensuring high depth accuracy. James and Robsons (2012) provided a convenient expression defined *precision ratio* that can be used in planning SfM-MVS project to ensure that the required precision

are achieved. The parameter compares the precision of the 3D data obtained to the average viewing distance used (i.e., the mean camera-to surface distance).

- Convergent imagery (see Fig. 3.3) reduces the model distortion and allows reconstruction of complex surfaces with a wide variety of face directions.
- To ensure sufficient similarity between overlapping images and matching success, use short baseline in case of complex object by reducing also risk of gaps. In addition maximum angular changes of 20° are advisable to identify correct keypoint correspondence that is limited for larger changes of perspective.
- Potentially occluded parts should be visible in at least 3 images. High redundancy on images observation increase the accuracy. However the exact number depends on the scene size and complexity. 80% of overlap between adjacent images is suggested.
- Acquire the images at different heights at each station, enable different viewing angles on the object. E.g. multiple rings for surrounding acquisition.
- Diffuse light condition are preferable to avoid reflective surface and strong contrast that negatively affect point matching.
- The interval between images should be minimised (<30m, Bemis et al., (2014)) as changes to lighting conditions and shadow locations will interfere with keypoints matching.
- Not stationary object in the scene that could potentially key points should be excluded during the camera orientation.

Camera setting

- Select the camera with larger sensor as provide a better dynamic range, finer detail and less noise.
- For large scale reconstructions, use large depth field because all pixel must be in focus for optimize the dense matching performance. This is achieve by setting high *f-values* (e.g. *f11-f14* thus small aperture) and where possible using a tripod in case of slow shutter speed.
- Images should not be geometrically altered (e.g. crop, rescale, use of image stabiliser) or compressed. For texturing reasons, it might be worth to acquire high dynamics range (HDR) images (Remondino et al., 2013).
- To reduce the noise of the images is preferable use low ISO value (e.g. 100/200), although noise levels depend on the quality of the camera. As suggested by Remondino et al., (2013), the goal is to achieve minimum noise at maximum sharpness/focus on all surfaces of interest by controlling, in the order of priority, aperture, shutter speed and ISO. To control these variables a compact camera should be avoided. To ensure sharpness, in case of exposure time >1/100s use a tripod. Maximize radiometric quality avoiding overexposed area, slightly underexposed images are better than overexposed.
- A medium focal length (equivalent to 50 mm on a full frame camera) is the most favourable setting. These lenses produce less geometric distortion and

create scene close to what the human eyes see. If it is necessary to use a wide angle lens ensure a larger overlap between images in order to avoid low quality reconstruction in the parts of the image that are near the frame edges (Remondino et al., 2013). To reduce the lens deformation a fixed focal length is recommended.

Georeferencing

- GCPs should be surveyed with accuracy 4-3 times better than the image GSD by using for example total station or GNSS. If the model is required to be georeferenced, in the absence of accurate GCPs, an alternative solution is identify natural features (at least three points) over stable areas clearly visible in the images. Although this method lack high accuracy as usually the control points are manually selected from LiDAR DEM of point cloud (Johnson et al., 2014).
- The GCPs should be distributed homogeneously on the surface.

3.2 QUALITY OF SFM IN GEOSCIENCE

The previously described advantages of the method have promoted the extensive use of the SfM-photogrammetry technique in geoscientific applications. Especially after that James and Robson (2012), Westoby et al. (2012) and Fonstad et al. (2013) demonstrated the suitability and flexibility of the SfM-photogrammetry to be applied at a wide range of scales. Furthermore, the combination of the SfM-photogrammetry approach with the rapid development of the unmanned aerial vehicles (UAVs) contributed to extend the range of applications up to 32 km for riverscape mapping (Dietrich, 2015). Some of the SfM-photogrammetry applications between 2012 and 2015 have included geomorphology (James and Robson, 2012; Diefenbach et al., 2012; Javernick et al., 2014), soil science (Castillo et al., 2012; Bemis et al., 2014; Stöcker et al., 2015; Kaiser et al., 2015), volcanology (James and Robson, 2012; Bretar et al., 2013), fluvial morphology (Woodget et al., 2014; Prosdocimi et al., 2015; Dietrich, 2015), and coastal morphology (Westoby et al., 2012), mass movements (Stumpf et al., 2015), forestry and precision agriculture (Dandois and Ellis, 2013; Mathews and Jensen, 2013) and glacial and periglacial environment (Kääb et al., 2014; Immerzeel et al. 2014; Dall'Asta et al., 2015; Rippin et al., 2015; Piermattei et al., 2015).
However, if the flexibility of the method is an advantage, on the other hand the quality of the resulting SfM-photogrammetry model depends on many factors related to an individual survey and this represents the biggest disadvantage of the technique (Smith at al., 2015). In addition, in similar contexts different results can be achieved depending on the platforms used (ground-based imagery or airborne solutions), sensor, data acquisition and software for imagery processing or post processing (i.e. filtering of noise and digital elevation model generation). To date, there is no comprehensive synthesis

of the practical options of a planning of a SfM-photogrammetry survey and the consequent errors that can derive from each choice.

As with any emerging technology, quantitative estimation of SfM-photogrammetry data accuracy is prerequisite to reliable application to a real problem, in particular to reconstruct surface topography over the time is mandatory to estimate the errors that are inherent to the technologies used. An overview of the SfM accuracy obtained in geoscience is given by Clapuyt et al. (2015), Smith et al. (2015), Eltern et al. (2016).

Accuracy assessment technique and accuracy measurements

A visual assessment of the SfM output in term of camera orientation and sparse point cloud is necessary to assess obvious positional errors of the camera orientation or artefacts in the sparse point cloud (Verhoeven et al., 2015). However, the total amount of the sparse and dense point cloud not express the strength and reliability of the method. Most of the SfM-photogrammetry packages do not provide accuracy values of the SfM results (e.g. standard deviation of 3D points and parameter correlations) or dense image matching performance. It is often assumed that the total reprojection error is a very good indication of the global accuracy of the SfM solution as demonstrated for example by Verhoeven et al. (2015), but this error is strictly related to the amount and position of the tie points extracted during the camera orientation. Registration residual error of ground control measurements is an accuracy statistic value reported by SfM-photogrammetry software. However, for considering this value as an accuracy assessment, it depends of the nature of the georeferencing that means if the control measurements are included in the BA optimisation or are used for georeferencing the model after the SfM step. In this latter case, the residual error provides reliable quality information because registration points are not integrated into model estimation. Otherwise, as BA minimises the error at these positions, the statistic only shows how well the software is fitting the data to the ground control measurements.

An accuracy assessment by comparing the output with other high resolution acquisition technique is required. Although, it is difficult to find a suitable reference for error assessment of SfM-photogrammetry in geoscientific or geomorphological applications due to the complex of the studied surface. TLS and ALS provide directly comparable topographic data. However, these reference data derived by laser scanning are rarely available and establish these data as benchmark for the SfM workflow is a challenging task because generally the technique is applied to natural environments. In fact, in many applications the quantitate validation of SfM-photogrammetry results is the primary aim, but others applications consist on mapping topography or extract planimetric measurement from SfM derived orthophoto, or use SfM approach to quantify surface change and volume. Therefore, a limited number of published studies performs accuracy assessment with independent references that are either area based (e.g. TLS) or point based (e.g. dGPS points) measurements.

So far, three validation methods, either point based or area based measurements, have been identified: 1). Point-to-Point (PP), 2). Point-to-Raster (PR) and 3). Raster-to-Raster (RR) (See Smith and Vericat, 2015). PP and RR are area based methods. The precondition to compare two point clouds (e.g. SfM-photogrammetry vs. TLS) is that two points would be exactly concordant under error free conditions, otherwise the comparison is suitable for a preliminary error assessment because this methods is affected by outliers and differing point density. The RR method is the comparison between the derived DEMs. To ensure comparability and validate the DEM generation, the adopted interpolation method for deriving DEM (both photogrammetry and reference) should be the same for both data and has to be chosen carefully according to complex of data and roughness. Additionally the method cannot be applied in case of undercuts surface as demonstrated by Frankl et al. (2014). PR is a point based method; DEM derived from SfM-photogrammetry are validated against point data generated by TS or dGPS. This approach however, ensure high accuracy of the reference data but it lacks of spatial coverage for a precision statement of local deviations. All of these methods allow to measure the distance between the reference data and the SfM-photogrammetry reconstructed surface. The main used tools for point cloud comparison are provided in the open source software Cloud Compare. Here the comparison is performed by calculating the absolute distance (Cloud-to-Cloud, C2C) between two point clouds or using the M3C2 algorithm proposed by Lague et al. (2013) that considers the surface normal for each points based on all data points within a pre-specified radius to inform the comparison of points. Stumpf et al. (2015) and Gómez Gutiérrez et al. (2015) achieved lower error values measured with M3C2 rather than C2C or point-to-mesh. The latter is another validation method that was adopted by Favalli et al. (2012). However this approach has the same issue of PR method and its application on very rough surfaces is not appropriate. As highlight in the recently review of the SfM-MVS applications by Smith et al. (2015), lower errors are measured for point-to-point distances and point-to-raster rather than raster differencing.

The main statistics reported to validate the SfM-photogrammetry results are the Root Mean Squared Error (RMSE), Mean error (ME) or Mean Absolute Error (MAE) and Standard Deviation (σ). RMSE is reported more commonly, as it gives an absolute accuracy value integrating all sources of error. ME should be treated with caution, because in many studies by comparing the SfM-photogrammetry model with a ground truth data has been demonstrated the presence of systematic errors visible as a pattern of positive and negative errors which compensate each other (James and Robson (2014); Dietrich, 2015). Therefore, this alternating pattern is not apparent in the mean values but can be explained by an error distribution map.

Filtering and digital elevation model generation

In several SfM-photogrammetry applications, before to start the comparison for accuracy assessment of the method, the ICP alignment of the overlapping portions of the SfM and LiDAR reference point cloud is performed to refine the registration error (rotation and translation). This method widely used for LiDAR processing, is also a logical step for SfM application as the aim is to compare two methods used to generate data in the same coordinate system requiring any alignment problems to be removed. A prerequisite for an accurate ICP-based registration is that the overlapping areas are completely free of vegetation.

Distinguish between ground surface and non-surface points and normalizing point density is often required for point clouds (Brasington et al., 2012). In most of geoscience applications the interest is on a bare surface model, usually defined by digital terrain model (DTM). In area of light to dense vegetation, the presence for bare surface becomes the primary disadvantages to SfM-photogrammetry reconstruction relative to active source 3D data collection tools (Bemis et al., 2014). In forested terrain ALS has a strong advantages compared to photogrammetry because the pulse of light is able to penetrate the vegetation and thus collecting ground surface points if the forest cover is not too dense. As the SfM-photogrammetry is a passive survey technique and the requirement to reconstruct the surface with the SfM-photogrammetry approach is to collect multiple images from different perspectives, the number of resolvable ground surface points is dramatically reduced by the occlusion of the vegetation covered when moving from one camera position to the next. Classification of vegetation and ground points is more challenges as they may be less easily distinguished. If the vegetation is sparse enough to allow a sufficient number of ground features to be identified and matched, the derived point cloud could be classify adopting the similar approaches developed for LiDAR classification, (Bemis et al. 2104). Brodu and Lague (2012) developed a tool (Canupo software) to classify the vegetation points based on multi-scale dimensionality criteria. Use of colour filters is also possible, as the photogrammetric technique returns true coloured points. In SfM-photogrammetry, vegetation is problematic for occlusion effects that means that areas occluded by vegetation cannot be recovered by the acquisition of images from different angles. In addition the vegetation is the cause of degradation in the quality of surface reconstruction (Micheletti et al., 2014; Dietrich, 2015). Westoby et al. (2012) and Bühler et al. (2014) largely discussed the evidence error introduce by the vegetation. So far, the use of SfM for terrain mapping has been limited to sites with sparse or lowing vegetation (Johnson et al., 2014).

Normalization of point density is a necessary step for creation of raster-based topographic data products, and reduce the file size. Usually the SfM-point cloud, especially form the ground present gaps that need to be fill and interpolated for DEM creation. Commercial available SfM-MVS software like PhotoScan provide tool for DEM generation and orthophoto. The latter are usually generated by running surfacing algorithms to generate a textured mesh, reprojection the photographs onto the mesh and viewing the mesh from an orthographic projection (Smith et al., 2015).

Accuracy assessment according to platform

A range of options are available to collect imagery that can be used for SfM-photogrammetry, either from ground-based or airborne acquisition. By comparing the two solutions, the handheld ground-based solutions are the best trade-off between pixel resolution, image quality and cost-effectiveness. It is easy to implement and to apply in several context as only a camera and georeferencing method is needed. The key disadvantages of this solution is that the spatial coverage is limited during one survey campaign. Although, the feasibility of a ground-based surveys is strictly related to the morphology and accessibility to the target area. James and Quinton (2014), Micheletti et al. (2014), Smith et al. (2014) have reconstructed areas like valley, cliffs (high relief) wider than one hectare from a terrestrial acquisition. Furthermore, matching of oblique images in flat context could provide not reliable results with high level of outliers (Smith et al., 2015).

To overcome these limitations, in recent years the UAVs have been used extensively for acquisition of SfM-photogrammetry. A wide range of UAV platform exist with different characteristics in terms of costs, stability (e.g. vibrations), payload and therefore type of camera that can be mounted, either fixed or gimballed-camera mount, flight times and therefore spatial coverage and fly control software (i.e. pre-programmed routes). Winged UAVs might not be stable enough under windy condition, and it might be difficult to find suitable starting and landing spots (Bühler et al., 2014). UAVs with rotors (i.e. 'multicopters' including quadcopters, hexacopters or octocopters) are much more stable and can acquire data under windy condition, but they have very limited flight times due to high energy consumption and the batteries needing that have to be change very often. UAVs with rotors are not yet able to efficiently cover areas larger than a few square kilometers in alpine conditions (Bühler et al., 2014). Another category of aerial platform is the piloted overflight in aircraft (Dietrich, 2015; Javernick et al., 2014) but its practical application is limited. These platforms improve the spatial coverage and are able to survey areas not reachable by a ground acquisition. However, several drawbacks exist in comparisons to a terrestrial acquisition. Firstly, these platforms require more expertise and they reduce the economic advantage of SfM-photogrammetry for the higher cost of the instrumentation and eventual damage that occur often. Then, the final pixel resolution for a specific camera is defined by the flying altitude, and in general, the blurring of the images caused by vibration reduces the quality of results. Moreover, in many countries legislation limits the range and ground type over which UAVs can fly.

3.3 TEST-FIELD

A test-field area surveyed using terrestrial photogrammetry has been chosen in order to test in a planned environment a series of parameters that affect the quality of the photogrammetric results. In this work two crucial practical aspects have been addressed which are (i) the camera network geometry and (ii) control data, showing strategies, considerations and the possible solutions. From a practical application point of view, a proper planning (of both photos and control data) of the photogrammetric survey especially for ground-based acquisition, is not always ensured due to the limited accessibility of the target object and the presence of occlusions such as vegetation cover or the presence of rock masses. To solve these problems, a different image acquisition strategy was proposed and several georeferencing procedure were tested to deal with the practical issues of a terrestrial photogrammetric survey.

The proposed photogrammetric survey is based on the acquisition of a sequence of images in panorama mode. This means that at each established position a series of pictures with overlapping fields of view are taken by rotating the camera on a standard tripod, to cover the object of interest. Because there is an offset of the pivot point from the projection center, these images theoretically cannot be stitched into a panorama. The advantages of this acquisition mode were already highlighted by Wenzel et al., (2013) who named the method "*One Panorama each step*". Multiple images acquired at each step to cover the whole desired object offer the benefit of redundancy of viewpoints from different directions and minimize the risk of data gaps. They proposed a practical guideline for acquisition planning, by suggesting the panorama acquisition, but detailed descriptions of the method and the accuracy estimation were not reported in the text.

The research study investigated the feasibility in terms of final accuracy of the 'panorama' method in comparison to the single frame acquisition for reconstructing the surface topography. Additionally, other factors of camera network geometry that influence the accuracy of 3D reconstruction were evaluated by changing 1) the number of overlapping images, 2) the camera-object distance by acquiring the images at three distances, and 3) the type and resolution of the camera.

The geo-referencing investigation consists of testing the use of directly observed camera positions with GPS (named GPS-PRCs), different GCP configurations, and GCPs with different accuracy, i.e. artificial targets vs. natural features.

Images of a test field in a low-slope artificial hill were acquired from the ground using an SLR camera. To validate the photogrammetric results a modern terrestrial laser scanner (TLS) survey was used as benchmark and a series of artificial targets measured with a total station were selected as check points (CPs). The commercial software PhotoScan (v.1.1.5) was employed to process the image datasets. Henceforth, the photogrammetric results obtained by PhotoScan are named with the acronym of PS.

3.3.1 Study Area

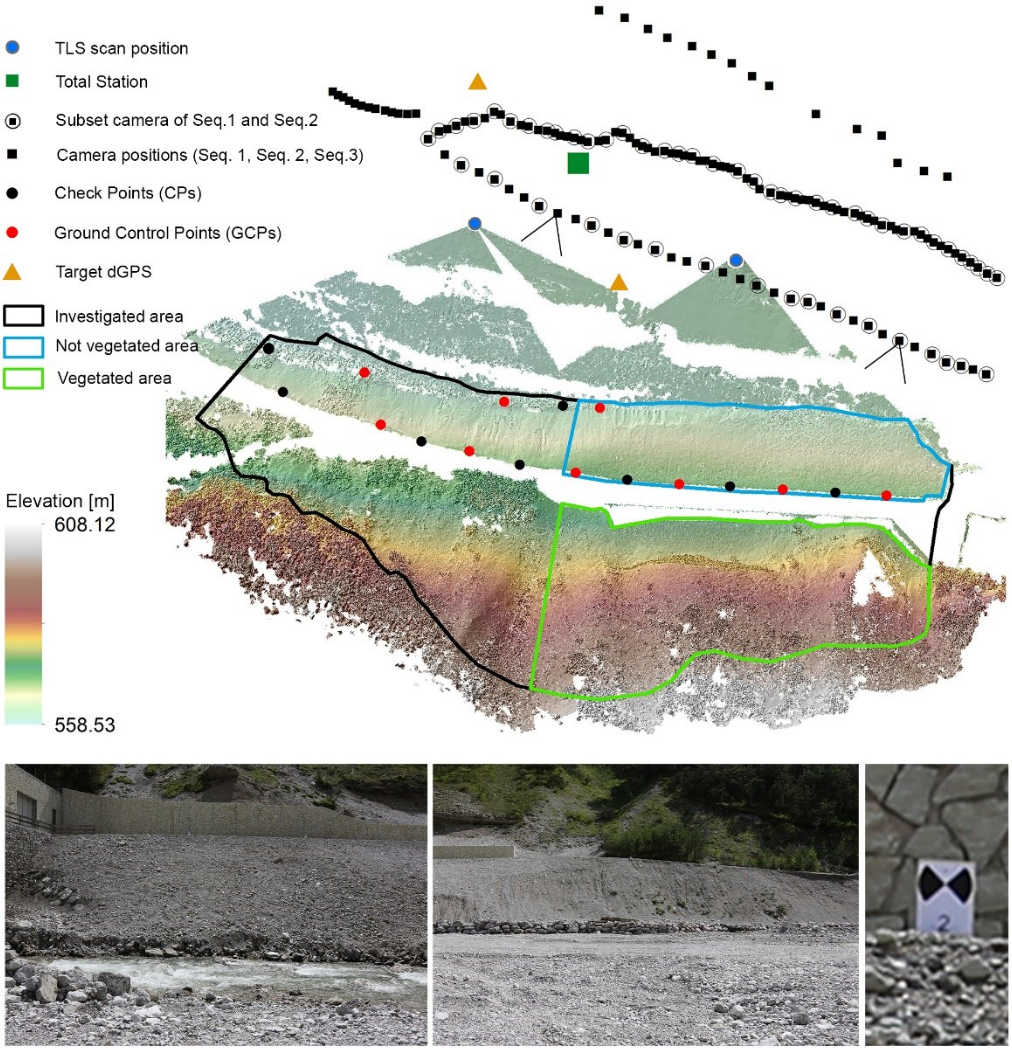

Figure 3.4. Geographic settings and survey configuration of the test field.

To test our image acquisition strategy and to deal with the practical issues of a terrestrial photogrammetric survey we selected a test area located at Torrente Val Montina, Perarolo di Cadore (Italy). The surveyed area is a hill next to the hydroelectric power station which was built at the terminal flat area of the stream Montina, a small branch of the river Piave. An access road to the building adjacent to a wall crosses the area. The investigated area alongside the stream has an extension of 150 meters and covers an area of about 7,300 m2 with an average slope of about 38°. The surface of the hill is characterized at the lower part, close to water, by gravel river debris of different sizes and at the upper part by shrub cover (Fig. 3.4).

3.3.2 Methods

The test survey took place on August 4th, 2014. The following surveying methodology was adopted to acquire the dataset: i) topographic survey with total station to measure the control data; ii) static positioning GNSS survey to perform the datum transformation; iii) terrestrial laser scanning acquisition of the area of interest and the artificial targets; iv) terrestrial photogrammetric survey acquiring the images from the same position in panorama mode and single photos; v) GPS-PRCs in real time kinematic (RTK). Data acquisition and photogrammetric workflow to produce the dense point clouds are described in the next section.

Topographic and TLS data acquisition and processing

The data acquisition started with the planning of target positions. We used 17 black/white targets mounted on a vertical planar support and two tripod-mounted Leica targets (i.e. 6'' circular blue/white target). The Black and white targets, used for photogrammetric purposes, were distributed within the area of interest. Due to accessibility and safety issues it was impossible to achieve a proper placing of these targets for the photogrammetric survey (i.e. covering the 3D extent of the area). A first line of 12 targets was distributed along the road and a second parallel line of 5 targets on the lower part of the hill, close to the river. The two circular targets were surveyed by dGPS measurements using a dual frequency GPS/GLONASS receiver (Topcon Hiper Pro) to geo-reference the data in the global coordinate system UTM-WGS84, zone 33N. The targets (both black/white and circular) were measured by means of a total station and of the TLS. The total station measurements were carried out with a reflectorless Leica TPS700 from one position, considering a maximum distance to the black and white targets of 95 m. The total station coordinates of the black and white targets were used for the image processing. Eight of these targets were used as GCPs in the bundle adjustment, and the other points as CPs (Fig. 3.4). RMSE of the target centers measured by total station compared to those surveyed by TLS was 0.013 m. The ScanStation C10 TLS was employed to generate a reference point cloud to validate the photogrammetric survey. TLS measurements were performed from two scan positions, located at mean distance of 50 m from the object. Target-based registration using both black and white flat targets and circular targets provided a first registration error of 0.019 m. The ICP optimization implemented in Leica Cyclone 8.0 produced an RMS value of 0.012 m (average 0.009 m).

The GPS-PRCs were measured by the following combination. As the images were taken from a tripod, the tripod plumb points were measured by GPS in Real Time Kinematic (RTK). The height of the camera tripod head (measured with a handheld laser range finder) was added to estimate the coordinates of the projection centers.

Photogrammetric data acquisition and processing

Data acquisition

Overlapping photos were acquired simultaneously with two different cameras, a SLR camera and a compact camera. The compact camera was a Canon PowerShot SX230 (5mm focal length) and it was used to acquire single images from each position. With the SLR camera the acquisition mode of the images was twofold, i.e. single images and panorama images. These images were taken with a Canon EOS5D Mark III (28 mm focal length, sensor size of 36.0 x 24.0 mm) attached to a tripod to avoid camera shake and to ensure approximately the same object coordinates of the projection centers for panorama image sets. The acquisition mode was as following: from each individual camera position, a first normal image of the investigated surface was taken, keeping the direction of the camera optical axis almost perpendicular to the surface. Then, to cover the whole surface from these positions, additional images were taken in panoramic mode, which involved taking a series of overlapping photographs by rotating the camera on the tripod from left to right. Before to move to next position, a single image (normal view) with the compact camera was taken. The photos were captured at three different distances to the interest object. The first sequence of images was acquired maintaining an average depth distance (D) of about 50 m from the object, yielding a mean GSD of 0.02 m. It was composed by 36 consecutive camera positions that implied 376 images for the panoramas from these positions (around 7÷14 photos per each position). The mean baseline (B) between adjacent camera positions was about 3 m.

To test the effect of distance on the accuracy and resolution of the SfM-photogrammetry model, other two sequence of images were acquired in parallel to the first. The same camera types were adopted to shoot the photos and additionally for the third sequence either single and panorama images were carried out. The second sequence of images was acquired at a mean distance of 70 m from the object by reducing the B to 1 m that increased the total number of images to 87. In the third sequence, due to the presence of vegetation on the line of acquisition, the images were acquired with a B of around 10 m at a distance of 90 m, for a total of 15 images. The mean GSD was 0.03 m and 0.06 m for the second and third sequence, respectively. Henceforth, the three sequence of images are named as Seq.1, Seq.2, and Seq.3.

Data processing

To test the panorama image acquisition, a subset of the entire dataset of Seq.1 was selected to reduce the amount of panorama images. Therefore, 18 camera positions of the entire sequence (36 images) were chosen including the first and the last station (Fig. 3.5). Consequently, the mean baseline between adjacent images was 8 meters. The normal images acquired from each of these positions were included in the panorama dataset during the processing, resulting in 187 images in total. The panorama dataset of the third sequence was composed by 144 images as only 15 camera positions were planned. Therefore the entire dataset was processed.

The dataset of 36 images of Seq. 1 was processed separately eight times testing i) GPS-PRCs, ii) natural features employed as GCPs whose coordinates were extracted from the TLS point cloud, and iii) different GCP configurations i.e. number and distribution of artificial targets measured with topographic instrumentation.

According to the process described in Figure A1, (Appendix A), the camera has not been pre-calibrated. Therefore a self-calibration procedure was adopted for the interior camera calibration. The calibration parameters as well as the external orientation of the images have been optimized in terms of "reprojection error". The software automatically select the points with a maximum reprojection error that has been set equal to a meter and recalculate parameters (internal and external) using tie points remaining. Not stationary objects present in the images like water of the river and clouds in the sky were masked after the images uploading in the software. The dense image matching was done by processing the images at half resolution. Additionally, some settings parameters of the dense point cloud reconstruction available in the software have been tested in term of final accuracy. In specific, the filtering used to create depth maps ('Aggressive', 'Mild' and 'Moderate') and the quality of the images (i.e. 'Ultra high', 'High' and 'Medium') used to reconstruct the dense cloud.

To identify the better processing of the panorama images with PS, additional constraints like camera positions into the BA and camera calibration parameters (that may be kept constant during the entire SfM processing) and were tested and compared.

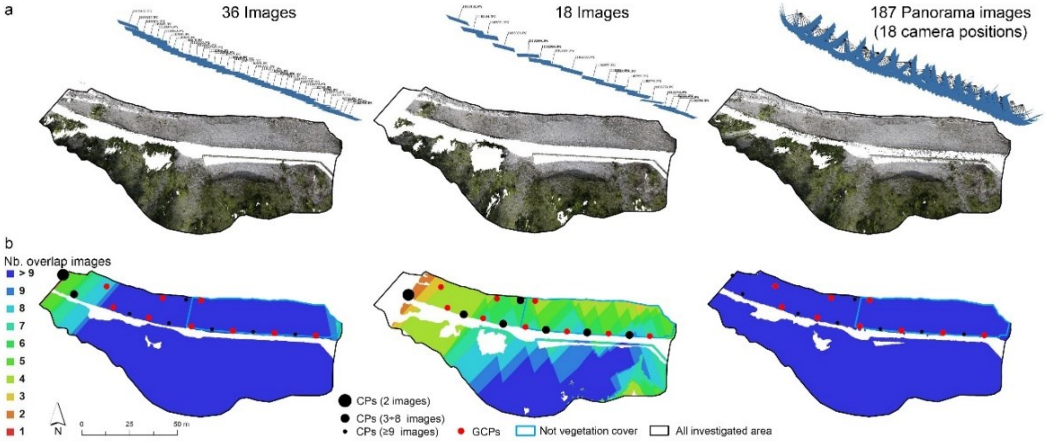

Figure 3.5. Acquisition geometry of Seq.1 for the panorama experimental test. a) Dense point cloud generated with PS and b) image coverage of the photogrammetric survey for each camera configuration: single (left, center) and panorama images (right). The black points represent the check point (CPs) and their dimension is related to the number of images that view that point.

Methods of accuracy assessment and analysis

Accuracy assessment of the photogrammetric results was performed considering both point cloud and digital elevation model (DEM). Even though the photogrammetric packages provide DEM reconstruction, the same interpolation method was adopted to create the elevation model of the TLS and the photogrammetric point cloud. These were created using Natural Neighbours interpolation in GIS environment with a pixel size of 0.05 x 0.05 m. For comparison purposes, areas without information were masked and not interpolated while converting point clouds into DEMs. The photogrammetric and the TLS 3D models were cropped to include only the area of interest. Furthermore, the analyses were performed for the entire investigated area and for two selected sub-area with and without vegetation cover. The TLS dataset and the 8 CPs were assumed as reference data. Considering the dataset the following accuracy analyses were performed:

- Root Mean Square Error (RMSE) of the computed object coordinates with respect to CP coordinates. We used the reconstructed, geo-referenced camera orientations to forward intersect the image observations of the CPs. Those forward intersected points were compared to the ones measured with the total station. The RMSE was evaluated for all CPs and in relation to the number of images (intersecting optical rays) that view these points (i.e. 2 images, 3÷8 images and >9 images) (Fig. 3.5).
- Absolute distance (cloud to cloud distance, C2C) between the TLS point cloud and the photogrammetric point cloud comparing both the sparse point cloud (tie points) and the dense point cloud.
- DEM of difference (DoD) between the TLS and the photogrammetric DEMs in the overlapping areas.

The main statistics as mean, standard deviation (σ) and RMSE for these analyses were derived. The spatial distribution of the error was also taken into account to describe the accuracy of the final DEMs.

The accuracy assessment of the reconstructed 3D models is divided in two sections according to the twofold aim of this work. In specific, the following analysis were conducted to develop the two objectives.

Objective 1): Accuracy assessment according the camera network geometry

- ❖ Repeatability of PS processing (embedded algorithms):
  - Data: 36 Images, Seq.1;
  - Analysis description: Reprocessing the same image dataset two time without changing the process method and setting parameters;
  - Accuracy estimation: CPs, C2C, DoD.
- ❖ Dense matching reconstruction with PS:
  - Data: 36 images, Seq.1;
  - Analysis description: Starting from the same oriented image block calculate the dense point cloud by changing i) the resolution of the images, named ‘Quality’ in PS, and ii). The smoothing filter, named ‘Filter’ in PS.

  - Accuracy estimation: C2C, DoD.
- ❖ Panorama images processing with PS:
  - Data: 187 panorama images, Seq.1;
  - Analysis description: Testing of various image process using different constraint (six tests).
  - Accuracy estimation: CPs, C2C, DoD.
- ❖ Panorama images vs Single images:
  - Data: 36 images and 18 images (single frame) and 187 panorama images (Result of test 4), Seq.1;
  - Analysis description: Comparison of the SfM-MVS results;
  - Accuracy estimation: CPs, C2C, DoD.
- ❖ Object-camera distance and Camera type:
  - Data: Canon EOS5D Mark III: 36 Images (Seq.1), 87 images (Seq.2), 36 Images (Seq.2), 15 images (Seq.3), 141 panorama images (Seq.3);
    Canon PowerShot: 36 Images (Seq.1), 15 images (Seq.3);
    Analysis description: Comparison of the SfM-MVS results;
  - Accuracy estimation: CPs, C2C, DoD.
- ❖ Incidence angle:
  - Data: 36 Images (Seq.1);
  - Analysis description: Calculation of the angle of incidence between camera and normal vector to the surface and relationship with Z-error.

<u>Objective 2): Accuracy assessment according the georeferencing approach</u>

- ❖ Directing georeferencing using GPS-PRCs of the camera
  - Data: 36 Images, Seq.1, GPS-PRCs measurements, GCPs coordinates (artificial targets) measured with TS;
  - Analysis: Comparison of the SfM-MVS results using GPS-PRCs and GCPs (9 artificial targets);
  - Accuracy analysis: CPs, C2C, DoD (before and after ICP).
- ❖ Directing georeferencing using GPS-PRCs of the camera + 4 natural feature as GCPs.
  - Data: 36 Images, Seq.1, GPS-PRCs measurements, coordinate of 4 points selected from the TLS point cloud used as GCPs;
  - Analysis: Comparison of the SfM-MVS results;
  - Accuracy analysis: CPs, C2C, DoD.
- ❖ GCPs georeferencing using 9 natural feature as GCPs
  - Data: 36 Images, Seq.1, coordinate of 9 points selected from the TLS point cloud used as GCPs, GCPs coordinates (artificial targets) measured with TS;
  - Analysis: Comparison of the SfM-MVS results by using natural feature (9 GCPs) vs artificial targets (9 GCPs);

    - Accuracy analysis: CPs, C2C, DoD;
- ❖ GCPs georeferencing using 5 GCPs (artificial targets) configurations;
    - Data: 36 Images, Seq.1, GCPs coordinates (artificial targets) measured with TS;
    - Analysis: Comparison of the SfM-MVS results obtained by 5 different GCPs configuration by changing number and location;
    - Accuracy analysis: CPs, C2C, DoD.

3.3.3 Results

Repeatability of PS processing

The first sequence of 36 images, with 9 artificial targets used as GCPs, was considered the reference photogrammetric dataset for the others experimental setup. In order to verify the reliability of these results obtained from PS, the same images sequence was reprocessed adopting the same workflow. The camera orientation and the dense point cloud reconstruction with PS present a high level of automatism and, as the software works like a black box, very limited knowledge about the embedded algorithms is available. Therefore this analysis allowed us to evaluate the repeatability of the algorithm implemented in the software.

The SfM-MVS reprocessing of the image dataset started with the camera orientation after the GCPs selection in the images. According to the workflow in Figure A1, (Appendix A), the camera optimization is the only semi-automatic step, which implies the selection of the tie-points that the software has to remove before to optimize the camera orientation (see Chapter 2, Sect. 2.2.1). First, the selection of these tie-points from the sparse point cloud is done via manual selection; then by setting the reprojection error the software will remove automatically the tie-points from the sparse point cloud with reprojection error higher than the setting value. Although the maximum reprojection error has been set to 1 pixel for both process, the tie-points automatically selected can slightly change by one process to another, and also the value of the maximum reprojection error of the remaining tie-points after the optimization can slightly be different. The two processing have small differences in the numbers of optimize tie-points with 129,892 and 133,457 pts for the first and second processing, respectively. Also the maximum reprojection error obtained by reprocessing is higher than the first with 1.221 pixel compared to 1.049 pixel. Then the other processing steps are completely automatically. The 3D models generated by both processing were compared with the ground truth data. The CPs errors provided identical results for the two processing. However the absolute distance between the two SfM-MVS point clouds obtained by the first processing (set as reference) and reprocessing the same images set was in average 0.012 m with a standard deviation of 0.013 m, (maximum error 6.922 m). The higher distance differences were principally distributed at the boundary of the reconstructed surface and on the vegetation covered areas (Fig. 3.6). This results was confirmed by the comparison of the two SfM-MVS point clouds with the TLS data. The error statistics produced identical results in the area not covered by vegetation that was also the reconstructed surface closer to the camera positions with stronger geometry of the camera (more overlapping images). The mean and σ differences with the TLS point cloud in the not vegetated area are 0.014 and 0.013 for the two images processing. The result suggests that the maximum accuracy obtainable by the adopted camera configuration and this dataset is 13 mm respect to the TLS measurements.

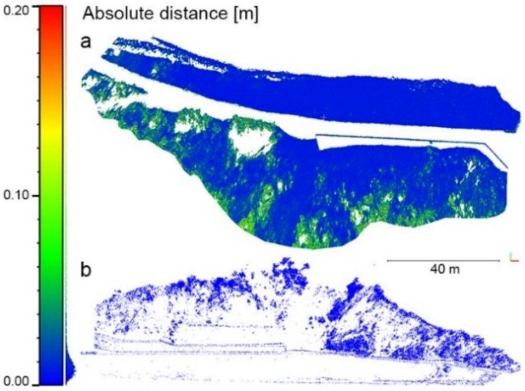

Figure 3.6 The absolute distance (C2C) between the SfM-MVS point clouds obtained processing two times the same images dataset with PS. a) A top view of the absolute distance (maximum value sett to 0.20 m) and b) a front view of the point cloud with an absolute distance values greater than 0.05 m.

Dense matching reconstruction with PS

The dense image matching is the step that requires more memory and processing time and often for large dataset with high resolution, (i.e. >100 images and >12 Mega pixel) it is impossible to reconstruct the dense point cloud using the full image resolution. Therefore, PS allows to downscale the images according to target 'Quality' parameters that is selected: 'Ultra High' no scaling (full resolution), 'High' images are downscaled two times by each side, 'Medium' downscaling four times by each side, 'Low' eight times, 'Lowest' sixteen times. The difference between High and Medium quality could be visible if original resolution is not high and some details are lost during downscaling. However, the downscaling affects the resolution of the dense point cloud (i.e. the point density) which depends on the number of processed pixels but the accuracy of the point cloud as well. The user should select the type of smoothing filter to generate the dense point cloud in PS. This filter is classified as Aggressive, Moderate and Mild. The dataset composed by 36 images (Seq. 1) was processed in order to estimate the effect of images down sampling provided by PS on the accuracy and resolution of the final 3D model. The quality of 'Ultra high', 'High' and 'Medium' with 'Mild' filter were tested. Furthermore, the dense point cloud of the same dataset was calculated by changing the smoothing filter and 'High' resolution quality has been set. The result showed that the images resolution for the dense matching affect drastically the number of dense point (Table 3.1 and Table 3.2). The mean and standard deviation of the DoD provided unexpected results as the Ultra High SfM-MVS DEM seems less accurate than the 'Medium' SfM-MVS DEM. Contrary, the point cloud comparison with the TLS provided more reliable results. The 'Ultra high' dense point cloud was 2 cm more accurate than the 'Medium' point cloud. Not significant differences in terms of number of points and accuracy were obtained by changing the smoothing filter.

Table 3.1. Accuracy estimation of the photogrammetric dense point cloud according to different image resolution and smoothing filter. The accuracy was evaluated for the three selected areas as absolute distance (C2C) between SfM-MVS and TLS point cloud set as reference. The TLS point cloud was composed by 21,292,050 pts for all reconstructed area, 6,235,258 pts for the sub-area without vegetation and 10,376,393 pts for the sub-area covered by vegetation.

		C2C between SfM-MVS and TLS point cloud								
Images Quality	Smoothing filter	All reconstructed area			Area without vegetation			Area with vegetation		
		Nb.Point Cloud [pts]	*Mean [m]*	*σ [m]*	*Nb.Point Cloud [pts]*	*Mean [m*	*σ [m]*	*Nb.Point Cloud [pts]*	*Mean [m*	*σ [m]*
Ultra High	Mild	70,232,381	0.033	0.074	21,169,829	0.013	0.012	24,369,697	0.044	0.116
High	Mild	19,296,400	0.040	0.085	4,808,269	0.014	0.013	7,329,673	0.052	0.127
	Moderate	19,845,341	0.041	0.088	4,684,563	0.014	0.013	7,582,995	0.052	0.131
	Aggressive	20,377,598	0.040	0.086	4,843,426	0.014	0.013	7,733,015	0.050	0.129
Medium	Mild	4,961,592	0.051	0.097	1,141,941	0.016	0.015	1,923,387	0.065	0.135

Table 3.2. Accuracy estimation of the photogrammetric dense point cloud according to different images resolution and smoothing filter. The accuracy was evaluated for the three selected areas as elevation difference (DoD) between SfM-MVS and TLS DEM set as reference.

		DoD between SfM-MVS and TLS DTM											
Images Quality	Smoothing filter	All reconstructed area				Area without vegetation				Area with vegetation			
		Min	*Max*	*Mean [m]*	*σ [m]*	*Min*	*Max*	*Mean [m]*	*σ [m]*	*Min*	*Max*	*Mean [m]*	*σ [m]*
Ultra High	Mild	-13.19	5.37	-0.05	0.52	-0.91	0.87	0.00	0.02	-6.53	5.37	-0.01	0.37
High	Mild	-13.17	5.64	-0.03	0.51	-0.88	0.88	0.00	0.02	-6.60	5.64	-0.01	0.40
	Moderate	-13.18	5.42	-0.04	0.52	-0.88	0.89	0.00	0.02	-6.57	5.42	-0.02	0.40
	Aggressive	-13.17	4.29	-0.05	0.52	-0.87	0.91	0.00	0.02	-6.40	4.06	-0.03	0.42
Medium	Mild	-13.15	5.25	-0.02	0.48	-0.79	0.84	0.00	0.02	-6.22	5.25	0.00	0.40

Accuracy assessment regarding to the camera network geometry

The proposed method based on panorama images acquisition was testing and compared to a single images acquisition reconstruction. Additionally, the factors of camera network geometry tested in this study area were the number of overlapping images, the object-camera distance, the camera type and the incidence angle.

Panorama images processing with PS

In order to identify the better workflow to process the 187 panorama images acquired from 18 positions (Seq. 1), different tests were performed as following:

- Test 1: Camera orientation with self-calibration including GCPs into the bundle adjustment optimization;
- Test 2: Camera orientation with self-calibration without GCPs constraint into the bundle adjustment optimization. The GCPs were used to scale and georeferenced the final dense point cloud after dense matching;
- Test 3: Camera orientation with the constraint of camera calibration (pre-calibrated camera) and GCPs into the bundle adjustment optimization. The camera calibration parameters were exported from the 36 dataset (Seq. 1) processed using the workflow in Figure A1 (Appendix A). The camera calibration parameters were not fixed during the bundle adjustment optimization;
- Test 4: Camera orientation with the constraint of camera calibration (pre-calibrated camera) and GCPs into the bundle adjustment optimization. The camera calibration parameters were exported from the 36 dataset (Seq. 1) processed using the workflow in Figure A1 (Appendix A). The camera calibration parameters were fixed during the bundle adjustment optimization;
- Test 5: Camera orientation with the constraint of camera calibration (pre-calibrated camera) and camera coordinates into the bundle adjustment optimization. The camera calibration parameters were exported from the 36 dataset (Seq. 1) processed using the workflow in Figure A1 (Appendix A). The camera calibration parameters were not fixed during the bundle adjustment optimization. The camera coordinates were export from the 36 images (Seq. 1) processed using the workflow in Figure A1 (Appendix A) by selecting the corresponding 18 camera positions. No GCPs were used in this test;
- Test 6: Camera orientation with the constraint of camera calibration (pre-calibrated camera) and camera coordinates into the bundle adjustment optimization. The camera calibration parameters were exported from the 36 dataset (Seq. 1) processed using the workflow in Figure A1 (Appendix A). The camera calibration parameters were fixed during the bundle adjustment optimization. The camera coordinates were export from the 36 images (Seq. 1) processed using the workflow in Figure A1 (Appendix A) by selecting the corresponding 18 camera positions. No GCPs were used in this test.

Test 5 and 6, without GCPs but with camera coordinates included into the bundle adjustment, provided the higher errors compared to the other tests which produced comparable error statistics (Table 3.4 and Table 3.5). To evaluate the error distribution for the first four test, a map of the elevation differences between SfM-MVS and TLS DEM was performed for each test (Fig. 3.7). The results suggest that GCPs to orient the panorama images are necessary. The better processing of the panorama images was based on a 'self-calibration' of the cameras by including the GCPs in the bundle adjustment optimization, without any others constraints, i.e. Test 1.

Table 3.3 SfM-MVS results of the panorama images processing (*total error of camera coordinates).

SfM-MVS results										
Images processing	Nb. images	Nb. Tie points	Reprojection error *[pix]*		GSD	9 GCPs error		8 Check point error *[m]*		
		[pts]	*Mean*	*Max*	*[m/pixel]*	*[m]*	*[pixel]*	*2 images*	*3÷8 images*	*>9 images*
Test 1	187	131,471	0.407	1.222	0.020	0.032	0.522	—	—	0.029
Test 2	187	143,694	0.407	1.066	0.020	0.026	1.823	—	—	0.058
Test 3	187	138,756	0.409	1.190	0.020	0.032	0.542	—	—	0.031
Test 4	187	100,289	0.412	1.283	0.020	0.069	0.632	—	—	0.133
Test 5	187	143,051	0.407	1.063	0.020	0.128*	—	—	—	0.626
Test 6	187	86,161	0.407	1.116	0.020	0.216*	—	—	—	0.312

Table 3.5. The elevation difference (DoD) calculated for each test between the panorama images reconstructed DEM and the TLS DEM set as reference data.

DoD between SfM-MVS and TLS DEM													
Images processing	Nb. images	All reconstructed area				Area without vegetation				Area with vegetation			
		Min [m]	*Max [m]*	*Mean [m]*	*σ [m]*	*Min [m]*	*Max [m]*	*Mean [m]*	*σ [m]*	*Min [m]*	*Max [m]*	*Mean [m]*	*σ [m]*
Test 1	188	-13.19	11.03	-0.03	0.50	-0.85	0.90	0.01	0.02	-6.62	5.95	-0.02	0.41
Test 2	188	-13.09	11.61	-0.01	0.51	-0.86	0.89	0.01	0.02	-6.63	5.46	0.02	0.41
Test 3	188	-13.24	11.28	-0.05	0.51	-0.79	0.91	0.01	0.02	-6.63	5.91	-0.03	0.41
Test 4	188	-13.01	11.08	-0.02	0.49	-0.68	0.88	0.01	0.03	-6.63	5.91	-0.03	0.41
Test 5	188	-14.39	9.45	-0.80	0.65	-0.97	0.64	-0.39	0.12	-7.80	4.61	-1.01	0.50
Test 6	188	-13.41	10.26	-0.31	0.52	-0.85	0.72	-0.16	0.05	-7.16	5.99	-0.41	0.43

Table 3.4. The absolute distance (C2C) calculated for each test between the panorama images reconstructed point cloud and TLS point cloud.

C2C between SfM-MVS and TLS point cloud										
Images processing	Nb. images	All reconstructed area			Area without vegetation			Area with vegetation		
		Point Cloud [pts]	*Mean [m]*	*σ [m]*	*Point Cloud [pts]*	*Mean [m]*	*σ [m]*	*Point Cloud [pts]*	*Mean [m]*	*σ [m]*
Test 1	188	21,587,050	0.048	0.108	4,340,984	0.016	0.015	8,680,504	0.059	0.144
Test 2	188	21,254,769	0.054	0.104	4,251,606	0.015	0.015	8,506,243	0.070	0.147
Test 3	188	21,564,849	0.051	0.108	4,303,006	0.018	0.015	8,691,481	0.062	0.145
Test 4	188	21,413,122	0.052	0.098	4,578,943	0.018	0.018	8,428,401	0.061	0.138
Test 5	188	21,868,384	0.557	0.272	4,428,757	0.302	0.113	8,719,013	0.705	0.217
Test 6	188	23,110,226	0.199	0.128	5,075,796	0.120	0.044	9,044,787	0.270	0.145

Panorama images vs Single images

The results obtained from the orientation of the panorama images (Test 1) were compared with the results produced from the single images processing by considering either the 18 single images and the 36 images dataset, in order to evaluate the accuracy of the SfM-MVS reconstruction from the panorama images in comparison to the single images acquired from the same positions and doubling the camera locations (Fig. 3.5). The photogrammetric dataset and the main results of the image processing based on the camera acquisition setup are shown in Tables 3.5 and Table 3.6. Few statistics and information on the camera orientation results are available from the PS software. Therefore a first analysis was to compare the sparse point clouds with the laser scanning point cloud in terms of absolute distances (C2C in Table 3.5).

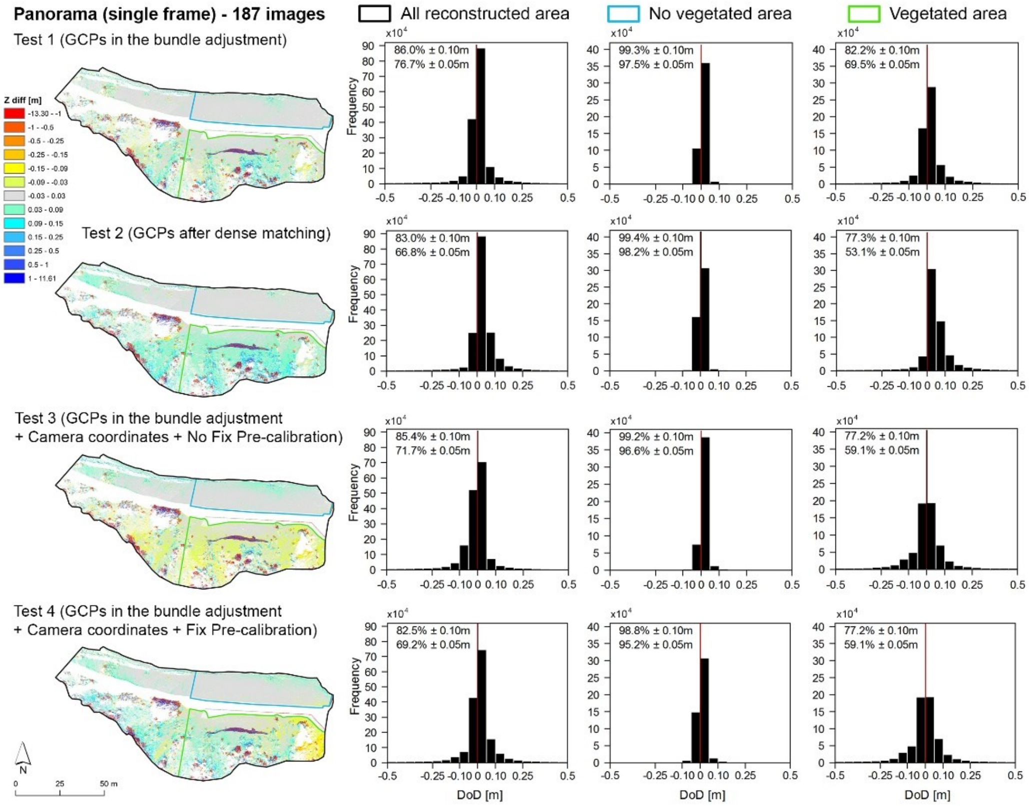

Figure 3.7. Map of the elevation difference (DoD) distribution calculated for each test between the panorama images reconstructed DEM and the TLS DEM. The histogram show the error distribution calculated for all reconstructed area, area covered by vegetation and without vegetation.

Table 3.5 Dataset characteristics and image processing results for single images acquisition vs. panorama acquisition using PS.

SfM results												
Camera acquisition	Reprojection error		Nb. of tie points	9 GCPs RMSE		Check point RMSE *[m]*				C2C sparse point		
	Mean [pix]	*Max [pix]*	*[pts]*	*[m]*	*[pixel]*	*All images*	*2 images*	*3÷8 images*	*≥9 images*	*Mean [m]*	*σ [m]*	*RMSE [m]*
36 images	0.390	1.049	119,719	0.015	0.321	0.068	0.183	0.034	0.019	0.025	0.040	0.047
18 images	0.357	1.100	35,356	0.030	0.261	0.034	0.065	0.026	—	0.032	0.062	0.070
187 panorama	0.407	1.222	115,055	0.032	0.522	0.029	—	—	0.029	0.027	0.058	0.064

The elevation of the panorama images sparse point cloud is on average higher than the TLS point cloud by 2.7 cm, with a variation of ± 5.8 cm. The 36 images orientation produced similar results in terms of mean, 2.5 cm, and standard deviation, 4.0 cm, with a comparable number of tie points. The 18 single images configuration provided a slightly lower accuracy (3.2 cm ± 6.2 cm) with also a lower number of extracted tie points. The accuracy estimation of the photogrammetric 3D model after dense point cloud reconstruction was performed by analysing the error statistics of both DoD and C2C comparison. The accuracies for the whole investigated area obtained by processing either the panorama images or the 18 single images, are practically identical to those obtained by processing 36 images. In the area not covered by vegetation, the 18 single images acquisition produced a higher value of σ and RMSE compared to the other two datasets. This result is confirmed by the frequency distribution histograms extracted from DoD （Fig. 3.8）. The histograms reveal a normal distribution of elevation differences in the three datasets. However, the dispersion around zero is lower in the panorama imagery in comparison to the single views acquired from the same positions: 86% of the height differences fall in the range ±0.05 m for the 18 images dataset, whereas the percentage increases to about 98% for both the panorama images and the 36 images. Furthermore, the 3D model generated from 18 single images was incomplete as visible in the spatial distribution of elevation differences （Fig. 3.8, “18 Images”）. The map of the z-differences suggests a deformation （bending effect） in the 3D results obtained by processing the single images, both from 18 and 36 camera positions （Figs. 3.8 and Fig. 3.9）. This deformation, strongest at the borders of the 3D model is also demonstrated by the high error （0.18 m） of the check point located in that area.

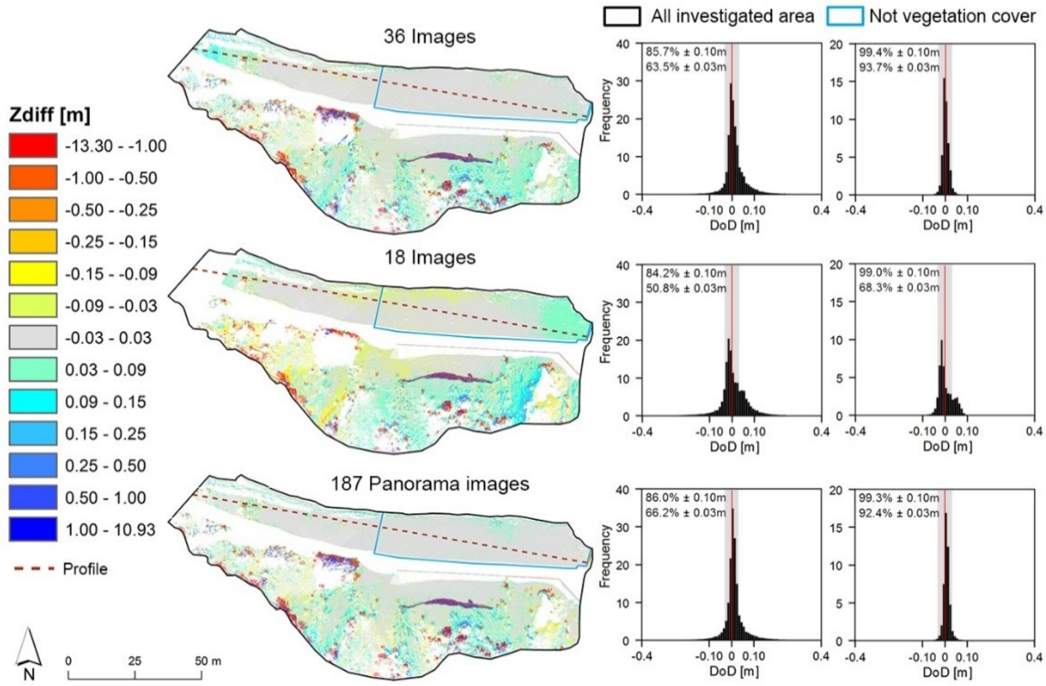

Figure 3.8. The spatial distribution of elevation differences （DoD） between TLS data and each DEM derived from each image dataset processed using PS.

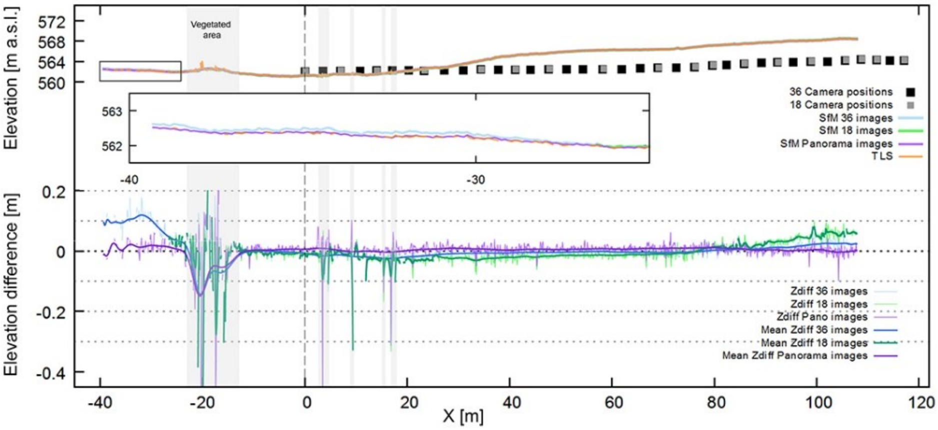

Figure 3.9. Profiles show the elevation change and the difference between PS and TLS-based DEMs. The location of the profile (red dashed line) is indicated in Figure 3.8. The origin of the x-axis is at the first camera position (in the West) and the minimum and maximum values of the z-differences are set to -0.4 m and 0.2 m, respectively.

Table 3.6. Accuracy assessment based on the elevation difference (DoD) and the absolute distance (C2C) between the photogrammetric data and the TLS reference data for each camera acquisition dataset processed by PS.

	DoD						**Nb. dense point**		**C2C dense point cloud**					
Camera acquisition	All investigated area			Not vegetated area			All investigated area	Not vegetated area	All investigated area			Not vegetated area		
	Mean [m]	*σ [m]*	*RMSE [m]*	*Mean [m]*	*σ [m]*	*RMSE [m]*			*Mean [m]*	*σ [m]*	*RMSE [m]*	*Mean [m]*	*σ [m]*	*RMSE [m]*
36 images	-0.03	0.51	0.508	0.00	0.02	0.022	19,296,390	4,808,269	0.040	0.086	0.095	0.014	0.013	0.019
18 images	-0.04	0.47	0.474	0.00	0.04	0.037	15,189,359	4,688,015	0.042	0.092	0.101	0.023	0.017	0.028
187 panorama	-0.03	0.50	0.505	0.01	0.02	0.024	21,587,050	4,340,984	0.048	0.104	0.114	0.016	0.015	0.022

Object-camera distance and Camera type

To evaluate the accuracy in relation to the distance that observe the scene, the images were acquired at a mean distance of 50 m (Seq. 1), 70 m (Seq. 2) and 90 m (Seq. 3) from the scene. The respective amount of images was 36, 87 and 15. To test the influence of the number of overlapping images on the final accuracy, a subset of 36 images was selected from the Seq. 2 and the results were compared with the entire dataset (87 images) acquired at the same distance and with the dataset composed by 36 images of the Seq. 1. Furthermore, the feasibility of the panorama image reconstruction at longer distances in comparison with single images reconstruction was tested using the third sequence of images (i.e. 144 panorama images vs 15 images at 90 m object-camera distance).

For each images sequence, the images of the compact camera were processed and the corresponding results obtained by the SLR were compared. The software was not able to process the dataset of the sequence 2. Therefore the comparison between the two camera types was done considering the dataset of the first and the third sequence at 50 and 90 m, respectively. Not panorama images were acquired by the compact camera. The same workflow was adopted to process all experimental dataset and the results are showed in Table 3.7, 3.8 and 3.9. The increase object-camera distance from 50 m to 90 m reduced around three time the number of the dense point cloud. However this result was influenced by the different number of camera position. In fact, at the same distance the lower number of images provided also the lower number of point cloud (Sequence 2, 36 images vs 87 images). Therefore is the number of overlapping images that influenced more the point density. Contrary, in terms of accuracy the lower number of images with higher baseline (36 images with B equal to 3 m) resulted to be more accurate than the point cloud generated from double camera position with lower baseline (87 images with B equal to 1 m). As expected, by increasing the intersection angle between the overlapping images the accuracies increase. The point cloud generated by panorama images, at an object-camera distance of 90 m, provided a slightly lower accuracy than the single images point cloud in the area covered by vegetation. Although in this area, the number of points were higher for the panorama images reconstruction due to the higher number of camera observations. By comparing the elevation difference of DEMs opposite results were obtained and the panorama images provided less error than the single images DEM in the three investigated areas (Fig. 3.11). The compact camera with lower resolution, and a wide focal length has provided a lower resolution of the point cloud and on the ground (GSD). However, in term of accuracy not significant differences were noted among the compact camera and the expensive SLR camera. As already reported in the literature (Thoeni et al., 2014).

Table 3.7. The SfM-MVS results for the three sequences of acquired images and for the two camera models.

SfM-MVS Results										
Images acquisition	Distance camera-object	Nb. images	Reprojection error *[pix]*		GSD	9 GCPs error		8 Check point error *[m]*		
			Mean	*Max*	*[m/pixel]*	*[m]*	*[pixel]*	*2 images*	*3÷8 images*	*>9 images*
				Canon EOS 5D Mark III						
Seq. 1	50	36	0.390	1.049	0.019	0.015	0.321	0.182	0.034	0.017
Seq. 2	70	36	0.394	1.042	0.029	0.013	0.373	0.168	0.013	0.019
Seq. 2	70	87	0.400	1.109	0.027	0.012	0.386	—	—	0.020
Seq. 3	90	15	0.381	1.024	0.040	0.024	0.319	—	0.069	0.033
Seq. 3 (Panorama)	90	141	0.411	1.054	0.040	0.018	0.452	—	—	0.020
				Canon Powershot						
Seq. 1	50	36	0.440	1.055	0.032	0.014	0.454	0.043	0.078	0.016
Seq. 3	90	15	0.452	1.121	0.061	0.023	0.547	—	0.141	0.018

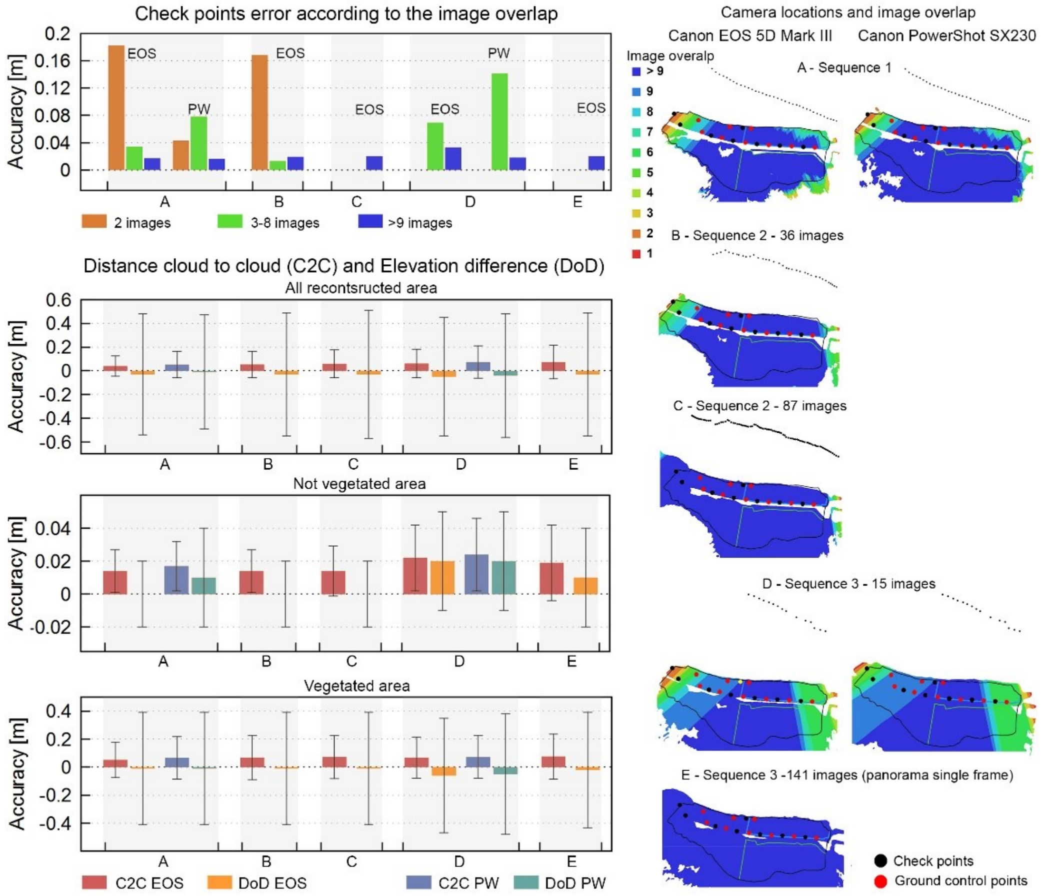

Figure 3.10. Accuracy of SfM-MVS estimates as Euclidean distance between laser and photogrammetry data in the three investigated areas (all reconstructed area, not vegetated area and vegetated area) and for the two camera models (Canon EOS MarkIII - EOS, and Canon Powershot - PW). Check points errors calculated for the camera models (EOS and PW) and for each camera sequence. The CPs error was evaluated according to the number of images that observed the point (image overlap).

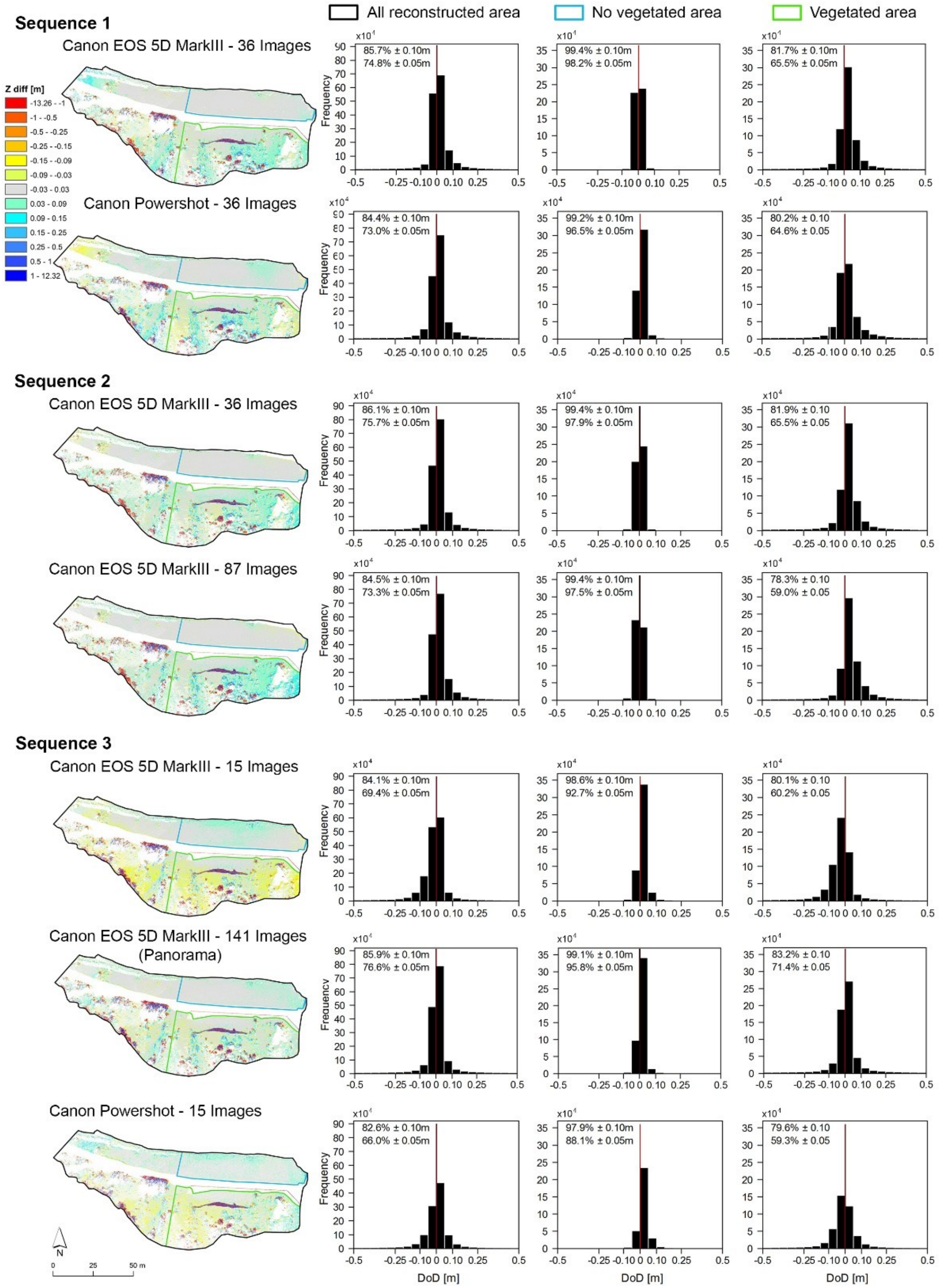

Figure 3.11. Elevation difference (DoD) between SfM-MVS DEM and TLS DEM calculated for each sequence of images with the two camera models.

Table 3.8. The Euclidean distances between laser and photogrammetric data (C2C) results for the three sequences of acquired images and for the two camera models.

Absolute distance (C2C) between SfM-MVS and TLS point cloud											
Images acquisition	Distance camera-object	Nb. images	All reconstructed area			Area without vegetation			Area with vegetation		
			Point Cloud [pts]	*Mean [m]*	*σ [m]*	*Point Cloud [pts]*	*Mean [m]*	*σ [m]*	*Point Cloud [pts]*	*Mean [m]*	*σ [m]*
Canon EOS 5D Mark III											
Seq. 1	50	36	19,296,400	0.040	0.085	4,808,269	0.014	0.013	7,329,673	0.052	0.127
Seq. 2	70	36	10,293,039	0.054	0.111	1,844,336	0.014	0.013	4,151,001	0.068	0.158
Seq. 2	70	87	13,255,461	0.060	0.119	2,203,769	0.014	0.015	5,234,747	0.073	0.154
Seq. 3	90	15	5,418,686	0.062	0.119	1,052,867	0.022	0.020	2,152,486	0.068	0.146
Seq. 3 (Panorama)	90	141	6,386,990	0.074	0.142	1,038,797	0.019	0.023	2,496,410	0.076	0.161
Canon Powershot											
Seq. 1	50	36	7,268,853	0.053	0.110	1,620,428	0.017	0.015	2,856,100	0.066	0.153
Seq. 3	90	15	2,279,842	0.074	0.136	433,614	0.024	0.022	882.445	0.072	0.152

Table 3.9. The elevation differences (DoD) between laser and photogrammetric data (C2C) results for the three sequences of acquired images and for the two camera models.

Elevation difference (DoD) between SfM-MVS and TLS DTM														
Images acquisition	Distance camera-object	Nb. images	All reconstructed area				Area without vegetation				Area with vegetation			
			Min [m]	*Max [m]*	*Mean [m]*	*σ [m]*	*Min [m]*	*Max [m]*	*Mean [m]*	*σ [m]*	*Min [m]*	*Max [m]*	*Mean [m]*	*σ [m]*
Canon EOS 5D Mark III														
Seq. 1	50	36	-13.17	5.64	-0.03	0.51	-0.88	0.88	0.00	0.02	-6.60	5.64	-0.01	0.40
Seq. 2	70	36	-13.17	5.56	-0.03	0.52	-0.70	0.93	0.00	0.02	-6.75	5.56	-0.01	0.40
Seq. 2	70	87	-13.17	6.50	-0.03	0.54	-0.68	1.04	0.00	0.02	-6.59	6.50	-0.01	0.40
Seq. 3	90	15	-13.26	12.11	-0.05	0.50	-0.72	0.98	0.02	0.03	-6.59	5.68	-0.06	0.41
Seq. 3 (Panorama)	90	141	-13.21	11.58	-0.03	0.52	-0.90	0.93	0.01	0.03	-6.75	5.73	-0.02	0.41
Canon Powershot														
Seq. 1	50	36	-12.92	11.56	-0.01	0.48	-0.83	0.98	0.01	0.03	-6.31	5.47	-0.01	0.40
Seq. 3	90	15	-13.23	12.32	-0.04	0.52	-0.75	0.97	0.02	0.03	-6.53	4.87	-0.05	0.43

Incidence angle

The incidence angle is an important control parameter on the reconstruction accuracy. The angle of incidence represents the angles between line of sight of the camera and normal vectors of the surface. The relationship between the incidence angle of camera and the elevation difference between SfM-MVS and TLS DEMs was estimated, considering the SfM-MVS model obtained by processing the first sequence of images (36 images). To estimate the incidence angles, the normal vectors of the surface and the camera positions has to be identified. The normal vectors were calculated for each cell of the SfM-MVS DEMs, considering a grid of 0.05 m x 0.05 m (Fig. 3.12b). The problem of camera positions was simplified by considering one average camera position. In this case the selection of one camera position has not affected the test because all cameras were acquired at the same altitude. The results showed no significant relationship between elevation error of SfM-MVS DEMs and incidence angle. However more than the 80% of the cells had an incidence angles between 60° and 90° (Fig. 3.12c and Fig. 3.12d).

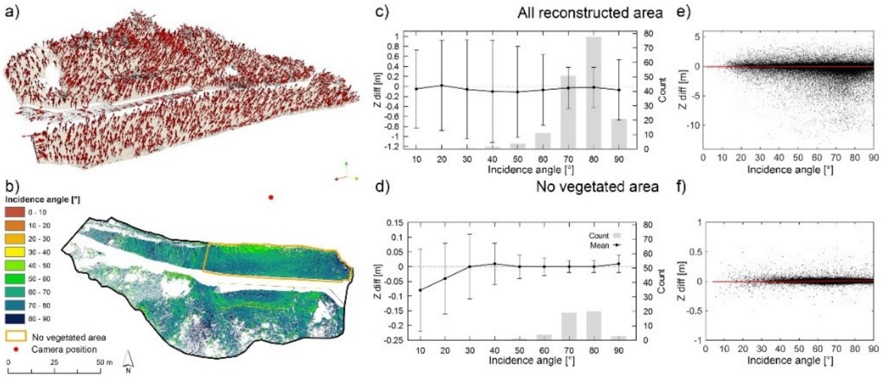

Figure 3.12. Incidence angles between the selected cameras position and vectors normal to the surface. (a) Plot of the vector normal to the surface and b) Map of the calculated incidence angle. Mean of elevation differences between SfM-MVS and TLS DEM with one standard deviation y bars calculated for incidence angle intervals c) in the all reconstructed area and d) in the not vegetated area and the scatterplot of the elevation difference and incidence angle e) in the all reconstructed area and f) in the not vegetated area.

Accuracy assessment regarding to the geo-referencing approach

To test the influence of the geo-referencing approach on the image-based reconstruction the Seq.1 data set composed by 36 images was processed. Geo-referencing based on the 9 artificial targets, being the GCPs already used above, is named in this section 'Configuration A' and we use respective results as reference for the others tests. All results for the different experimental setups are shown in Table 3.9.

Directing georeferencing using GPS-PRCs of the camera

A first investigation was performed on the feasibility of using the GPS-PRCs of the cameras to scale and geo-reference the image block. Since no reference data are available for the cameras position, the camera coordinates measured with RTK-GPS were compared with the camera positions estimated by PS after the bundle block adjustment and their differences for each camera positions are shown in Figure 6 as follows:

$\Delta_i = GPS - PRCs_i - O_{GCP,i}$; shown in Figure 3.13a;

$\Delta_i' = O_{GPS-PRCs,i} - O_{GCP,i}$; shown in Figure 3.13b;

where:

i: image index 1…36;

O: Projection center;

O_{GCP}: Projection center from PS using Configuration A;

GPS-PRCs: position of cameras measured with GPS;

$O_{GPS-PRCs}$: Projection center from PS using *GPS-PRCs* for datum transformation.

The largest discrepancies between the GPS_PRCs measurements and the OGCP were found for the y coordinate (depth value) of the cameras with a mean offset of 0.068 m, in comparison to -0.006m and 0.035m for the x and z coordinates, respectively (total RMSE is 0.093 m). The comparison of OGPS-PRCs with OGCP provided an almost linear trend with a RMSE of 0.078 m (Fig. 3.13b). The inaccuracy of the GPS-PRCs produced a shift and rotation of the final 3D model as visible in the spatial distribution of the elevation difference between SfM and TLS based DEM (Fig. 3.14, "GPS-PRCs"). To solve this shift error, a LiDAR survey of the same object can be used. In this work, we used the TLS point cloud to co-register the photogrammetric point cloud using the ICP algorithm and to combine direct geo-referencing with some natural features employed as GCPs. A version of the ICP algorithm tailored to topographic point clouds (Glira et al., 2015) was applied. The co-registration with the TLS point cloud minimized the orientation error of the photogrammetric model caused by the inaccuracies of the GPS-PRCs. Furthermore, even better results were achieved in terms of error statistics and spatial distribution of the elevation differences than those obtained from processing the images with GCPs (Table 3.11 and Fig. 3.14, "GPS-PRCs after ICP", "GCPs Configuration A"). Incorporating into the bundle adjustment the GPS-PRCs and 4 natural GCPs located in the lower part of the area reduced the tilt problem, but some distortions in the 3D model are visible in comparison with the reference TLS DEM (Fig. 3.14, "GPS-PRCs + 4 Natural Features").

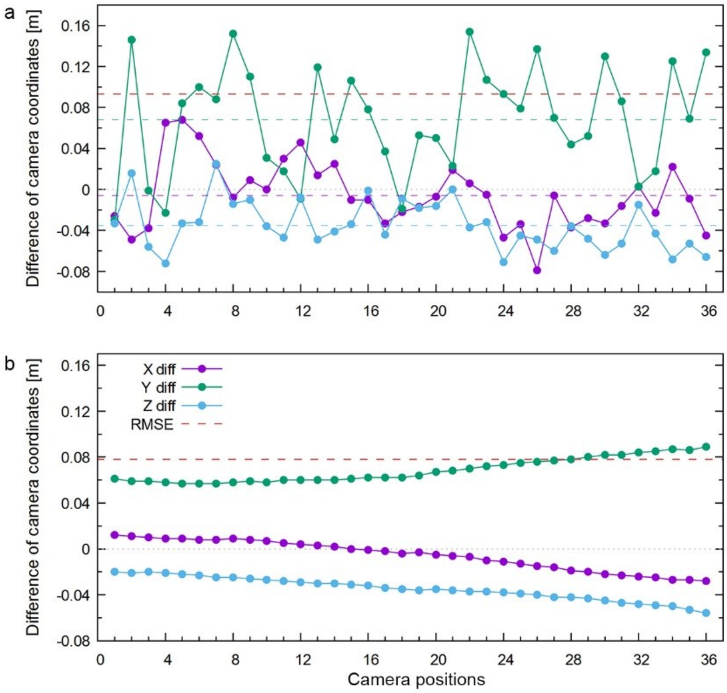

Figure 3.13. Differences between a) GPS-PRCs and O_{GCP}, and b) O_{GPS}-PRCs and O_{GCP}.

Table 3.10. Dataset characteristics and image processing results for the tested geo-referencing approaches.

SfM-MVS results

Georeferencing	Nb. GCPs	Reprojection error		9 GCPs RMSE		8 Check RMSE *[m]*			
		Mean [pix]	*Max [pix]*	*[m]*	*[pixel]*	*All images*	*2 images*	*4 images*	*>9 images*
GPS-PRCs	—	0.389	1.055	—	—	0.104	0.227	0.119	0.059
GPS-PRCs + Natural GCPs	4	0.392	1.042	0.039	0.461	0.063	0.086	0.058	0.059
Natural GCPs	9	0.392	1.047	0.046	1.00	0.058	0.134	0.027	0.038
A	9	0.390	1.049	0.015	0.321	0.068	0.183	0.034	0.019
B	3	0.390	1.068	0.003	0.288	0.082	0.161	0.032	0.067
C	4	0.391	1.061	0.016	0.295	0.063	0.169	0.019	0.021
D	6	0.390	1.086	0.009	0.342	0.064	0.162	0.051	0.024
E	3	0.392	1.073	0.010	0.237	0.053	0.110	0.023	0.054

GCPs georeferencing using 9 natural feature as GCPs.

To evaluate the influence of manual identification of natural GCPs, 9 points in the TLS point cloud and in the images were selected. These points were identified close to the artificial targets (Configuration A) in order to maintain the same control data distribution. The transformation residual error of the GCPs identification range from 0.019 m to 0.086 m (RMSE error was 0.046 m and 1.00 in pixel). Despite this error, no significantly lower accuracies were found in comparison to the results obtained by using artificial targets.

GCPs georeferencing using 5 GCPs configurations using 9 artificial targets.

To quantify the effect of ground control point location, five different GCP configurations (named A, B, C, D, E), changing the number and the distribution of the GCPs, were compared (Fig.3.14).

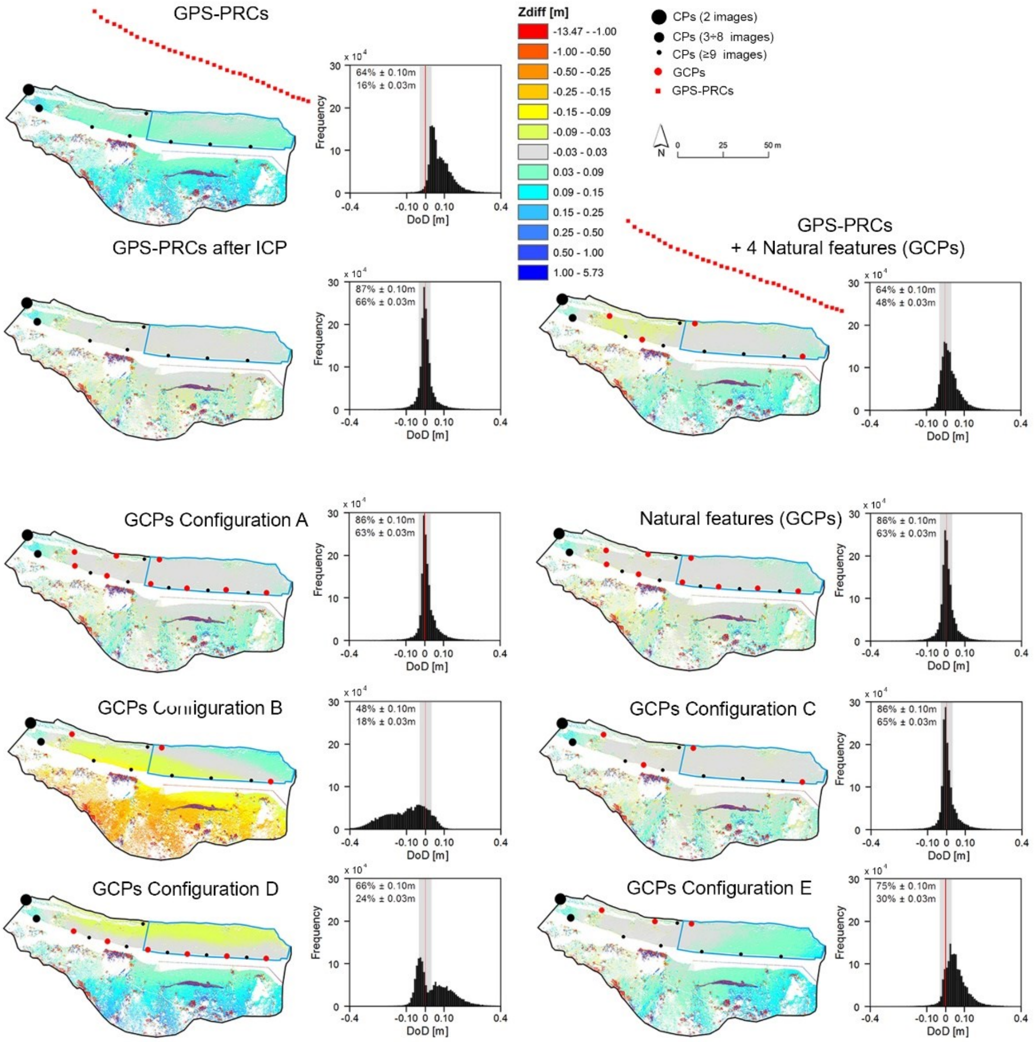

Figure 3.14. The spatial distribution of the elevation differences (DoD) between TLS data and each photogrammetric DEM obtained by processing the images with different georeferencing methods. The frequency distribution histograms extract from the DoD is provided for the entire investigated area.

Analysis of the GCP residuals suggested that the georeferencing had a RMSE of less than 2 cm for all GCP configurations. However, these statistics can be used as a first indication of accuracy of the network configuration, because these points were used to compute the solution of the network (Wachrow and Chandler, 2011) and the residual values show how well the data fit to the ground control points (Dietrich, 2015). The check points can be used to assess the accuracy in object space. However, in this work, the accuracy of the point cloud evaluated at the CPs is highly affected by the number of images that observe the area where the check point is located rather than by GCP distribution. Therefore, a spatial distribution of elevation differences between photogrammetry and TLS DEMs was considered to be essential for the accuracy analysis.

The map of z-error demonstrated strong model distortions (clustering of differences) in the configurations B, D and E caused by inappropriate GCP distributions (Fig. 3.14). These distortions are not highlighted in the accuracy estimation based on the mean, σ and RMSE of DoD, with the exception of the mean value of configuration B with -0.16 m calculated for the entire area (Table 3.11). For this test, a more reliable evaluation of the 3D model accuracy is provided by the distance analysis between the photogrammetric point cloud and the reference TLS point cloud. Configuration C characterized by four GCPs located on the boundary of the image block provided identical results of using 9 GCPs (Configuration A).

Table 3.11. Accuracy assessment based on the elevation difference (DoD) and the absolute distance (C2C) between the photogrammetric data and the TLS reference data for each geo-referencing experiment. * Without ICP registration with the TLS point cloud; ** After ICP registration with the TLS point cloud.

Georeferencing	Nb. GCPs	DoD						C2C					
		All investigated area			Not vegetated area			All investigated area			Not vegetated area		
		Mean [m]	*σ [m]*	*RMSE [m]*	*Mean [m]*	*σ [m]*	*RMSE [m]*	*Mean [m]*	*σ [m]*	*RMSE [m]*	*Mean [m]*	*σ [m]*	*RMSE [m]*
GPS-PRCs *	—	0.04	0.50	0.506	0.04	0.03	0.045	0.066	0.087	0.109	0.029	0.015	0.033
GPS-PRCs **	—	-0.04	0.50	0.506	0.00	0.02	0.024	0.039	0.086	0.095	0.015	0.013	0.020
GPS-PRCs + Natural GCPs	4	-0.02	0.51	0.508	0.00	0.03	0.026	0.046	0.086	0.098	0.016	0.014	0.021
Natural GCPs	9	-0.04	0.51	0.510	0.01	0.03	0.027	0.040	0.086	0.095	0.016	0.014	0.022
A	9	-0.03	0.51	0.508	0.00	0.02	0.022	0.040	0.086	0.095	0.014	0.013	0.019
B	3	-0.16	0.54	0.563	0.00	0.05	0.046	0.094	0.100	0.137	0.028	0.019	0.034
C	4	-0.04	0.50	0.505	-0.01	0.02	0.023	0.040	0.086	0.095	0.015	0.013	0.019
D	6	0.01	0.50	0.501	-0.03	0.03	0.042	0.062	0.089	0.109	0.027	0.017	0.033
E	3	0.01	0.51	0.507	0.04	0.03	0.053	0.055	0.086	0.102	0.034	0.021	0.039

3.3.4 Discussion

The results of this study show the feasibility of using images acquired in panorama mode to reconstruct the surface topography with the SfM approach. From a practical point of view the panorama images acquisition not required considerably more time in comparison to the single images acquisition. Furthermore, the proposed strategy improved the quality of the SfM results in comparison with those obtained from a single image. The advantages of the panorama acquisition are i) the high redundancy of the observations (i.e. how often a surface point is seen), ii) the increase of the baseline between images that view the same points that implies an increase of the intersection angles of optical rays, iii) the presence of multiple convergent images in the imaging geometry, and iv) less risk to have incomplete spatial coverage. These characteristics increase the quality of the 3D model reconstruction, as recently reported in literature. Indeed, as shown in (Rumpler et al., 2014) the mean accuracy increases with a higher number of images measurements, although there is a saturation on accuracy improvement within larger datasets. Similarly, Wenzel et al., (2013) demonstrated an improvement of the precision with increasing the intersection angles and redundancy. However, in this study the effect of large intersection angle on the final accuracy was greater than the number of overlapping images. Therefore, the panorama images acquired by rotating the camera at the same position allowed to increase the number of observations and at the same time the intersection angles between the cameras that view the same points, to lead to high completeness, especially in vegetated area and to reduce the systematic error thanks the presence of convergent imagery. The increase of the 3D model accuracy of the panorama images in comparison to the single images is defined by the higher number of points with higher accuracy according to TLS reference data which are distributed fairly evenly over the entire reconstructed area. Additionally, the elevation differences between the SfM and the TLS DEM show a lower distortion on the border of the reconstructed area in comparison to the model generated from 36 single images. The single views 3D model produced a bending effect on the border that is more evident in the model produced by a smaller number of camera positions. This demonstrates that parallel geometry of the images causes deformation, as reported in the literature (Dietrich, 2015), and the error is higher where the number of overlapping images is lower, and that the error increases outside the area covered by the GCPs. The RMSE of the CP located outside this area is greater than 10 cm. The model distortion could be solved by positioning GCPs there. The low overlap also leads to incomplete coverage of the 3D model, as demonstrated by the DEM reconstructed using 18 single images. The higher redundancy of the panorama acquisition increases the spatial coverage but also the number of tie points in comparison to the single images acquisition. The oblique views in panorama mode allow reconstructing areas that are occluded by vegetation and therefore not visible in a normal view on the object. The slightly lower number of the dense matching points that we obtain from the 'panorama' model in the vegetation-free area (close to the river) is probably caused by the different image masks of the river water and of the foreground used to process these images. The necessity to mask in PS the foreground for all panorama images represents a first drawback of this strategy as it is a time-consuming task. Specifically, the camera orientation without foreground masked (only the water of the river) provided worst results (i.e. not all images were properly oriented), therefore in this case was a mandatory task. Secondly, the high number of photographs uploaded requires more processing time and high computer performance, in particular for the dense matching computation.

For all reconstructed image-based models, the highest values of elevation difference are identified on the vegetated area and on the undercut area where, however, a vertical difference is not appropriate for accuracy evaluation. In SfM approach, vegetation represents a general limitation not only for occlusion but also for degradation in the quality of surface reconstruction (Micheletti et al., 2014; Dietrich, 2015) due to the high surface roughness and variable pattern (Stumpf et al., 2015). In our work, the standard deviation of elevation differences and distance 'cloud to cloud' with the TLS is significantly higher than the mean value in the vegetated area and it is the same order in the vegetation-free terrain. The mean value close to zero is related to the presence of negative and positive deviation that are rather spatially clustered. A positive trend of elevation differences is shown in the lower part of the area. This could be caused by the higher distance from the camera positions and by the not optimal distribution of GCPs to estimate the correct rotation of the surface.

The investigations in this paper highlighted a significant influence of the distribution of ground control points used for georeferencing on the SfM results. In particular, and in line with expectations, we demonstrated that a weak GCP distribution generated model distortions, providing good accuracy only within the area covered by the GCPs. Increasing the number of GCPs did not improve the photogrammetric results as also demonstrated by (Nocerino et al., 2014) and (James and Robsons, 2014). Furthermore, the final SfM accuracy is more affected by the GCP distribution than their accuracy, for example by using some natural features employed as GCPs whose coordinates were manually extracted from the TLS point cloud. As an alternative to GCP-based referencing we measured the GPS camera centers that were employed as control data. The resulting photogrammetric accuracy depends on the accuracy of GPS measurements. However, despite this inaccuracy, the 3D model showed no distortion or systematic error. The linear arrangement of camera positions left one rotation of the datum weakly defined. Therefore, an ICP registration with the reference TLS data was successfully used to compensate the transformation error (both translation and rotation) of the photogrammetric block. This solution provided the highest accuracy compared to other GCP-based geo-referencing tests.

4

SfM-MVS FOR MONITORING GLACIAL AND PERIGLACIAL PROCESSING

4.1 BACKGROUND AND INTRODUCTION

Three-dimensional (3D) topographic reconstructions based on high resolution digital terrain models (DTMs) are the main product for a variety of applications in glaciological research (Barrand et al., 2009). Digital Terrain Models (DTMs) of glaciated terrain are commonly applied to map glacier structure, morphology or landform distributions (e.g. Paul et al., 2004), to derive the parameters that are related to flow characteristics such as slope or velocity (e.g. Abdalati and Krabill et al., 1999), to measure changes in geometry and volume (e.g. Kääb and Funk, 1999; Krabill et al., 1999) and as input parameters for glacier mass-balance models (e.g. Arnold et al., 1996). Numerous techniques exist for monitoring and quantifying changes in the extent, mass and surface velocity of glaciers and rock glaciers and include both field and remote sensing methods (Immerzeel et al., 2014). Traditional topographic survey techniques, such as dGPS and Total Station, applied on glacial and peri-glacial environments are fundamentally based on field observations. Although these measurements generally yields high-quality data they are time-consuming and frequently provide small spatial extent with low point density, given the remoteness and low accessibility of mountain areas at high elevations (Roer et al., 2007; Barrand et al., 2009), that limit most practical applications (Karpillo and Ronald, 2009). Therefore, using remotely sensed datasets for at least two different points in time has become an important tool for monitoring high-mountain terrain dynamics (Kääb, 2002) and multitemporal DTMs are the most commonly used products for such investigations (Kääb, 2005; Tseng et al., 2015).

Among the many remote sensing techniques, aerial photogrammetry is the oldest method, and it has a long history of application in the study of glaciers (Welch and Howarth, 1968; Kääb and Funk, 1999; Schenk, 1999; Baltsavias et al., 2001; Kääb 2005; Haug et al., 2009; Bühler et al., 2014; Müller et al., 2014) and the monitoring of rock glaciers via repeated stereo images (Kääb et al., 1997; Kaufmann, 1998; Kääb et al., 2003; Fischer et al., 2011). Terrestrial (ground-based or close-range) photogrammetry was one of the first measurement techniques used to map high mountain terrain and for reliably measuring the flow velocity of a rock glacier (Kaufmann and Ladstädter, 2008; Kaufmann, 2012) until it was replaced by aerial and spaceborne platforms (Pellikka and Rees, 2009). Over the last decade, the photogrammetric technique has widely been replaced by LiDAR technology, both airborne and terrestrial laser scanning. LiDAR technology is reported as a very accurate methods for DTM

generation in geomorphology (e.g. Aguilar and Mills, 2008; Höfle and Rutzinger, 2011), also on snow (Höfle et al., 2007; Deems et al., 2013) and Alpine terrain (Bülher and Graf, 2013) and glacial environments (Geist Stotter, 2007; Kodde et al., 2007; Abermann et al., 2010; Knoll and Kerschner, 2010; Carturan et al., 2011; Colucci et al., 2015; Joerg and Zemp, 2014).
The increased need to reduce costs and operational limits of this survey techniques and the recent technological improvements in the field of image analysis have led researchers to reconsider the close-range photogrammetry for multi-temporal analysis in remote areas. A limited number of applications of SfM-photogrammetry exists on high altitude areas, principally employing Unmanned Aerial Vehicles (UAVs) for image acquisition (Solbø and Storvold, 2013; Whitehead et al., 2013; Immerzeel et al., 2014, Tonkin et al., 2014; Gauthier et al., 2014; Bühler et al., 2014; Dall'Asta et al., 2015a; Ryan et al., 2015) rather than ground-based surveys (Gómez-Gutiérrez et al., 2014; 2015). Kääb et al., (2014) tested the time-lapse SfM approach for measuring vertical and horizontal changes of periglacial patterned grounds.
The combination of two emerging technologies like SfM-photogrammetry and UAVs for glacial and periglacial monitoring has the potential to overcome many of the difficulties related to the main applied survey technologies (i.e. LiDAR, piloted aircraft, satellites and field method). However, survey platforms including helicopters and smaller scale UAVs at altitude is highly dependent on favourable weather conditions and may often be hampered by high wind speed and cloud cover. For terrestrial photogrammetric applications the greater practical limitation in alpine environment lies in achieving optimal camera positioning relative to the object of interest due to articulate topography, limited accessibility and hazardous areas. Additionally, reconstruction snow surface using SfM-photogrammetry is considered problematic due to the non-heterogeneous texture and the lack of features that the photogrammetric tool requires for generating the 3D models (Westoby et al., 2012; Fonstad et al., 2013).

This work demonstrated the applicability and the accuracy of ground based SfM-photogrammetry surveys for reconstructing glacial and periglacial environments and for measuring surface changes. In this research project, three real case studies were identified. The photogrammetric method was tested to reconstruct the Montasio Occidentale glacier, a debris covered glacier, the La Mare glacier and the neighbouring ADM3 Rock Glacier, a bilobate intact rock glacier located in the Ortles-Cevedale Group, Eastern Italian Alps. The primary goal was to obtain the optimum balance between the time and the risks associated with image capturing and the need to maximize the quality of the generated photogrammetric results. The terrestrial photogrammetric surveys were carried out using a common digital reflex camera, and the photos acquisitions were planned in order to obtained DTMs accuracies and resolutions sufficient for the calculation of the glacier mass balance (Montasio Occidentale glacier and La Mare glacier), and for the detection of the elevation changes and surface displacement of the Rock glacier. For the mass balance estimation, the geodetic method was applied that is based on the measure of the total volume change by using multi-temporal differences of DTMs

(Kaufmann and Ladstädter, 2008, Cogley et al., 2011). The SfM-MVS approach was applied to create a dense 3D point cloud of the investigated areas. As the DTMs represent the principal 3D products for measuring surface changes, the photogrammetric dense point clouds were interpolated to continuous surface before comparison with the reference data. The accuracy of the multi-temporal photogrammetric DTMs of the glaciers and the rock glacier was estimated as elevation differences between corresponding LiDAR DTMs (TLS for the Montasio glacier and ALS for La Mare glacier and rock glacier) assumed as benchmark. Additionally, for the debris covered glacier, the snow depth were measured by means of Ground Penetrating Radar (GPR) and the results compared with those obtained by the photogrammetric DTMs. Several issues of the photogrammetric approach (i.e., snow covered, accessibility and variable illumination condition) should be considered for application in glacial and periglacial environments. The main factors that affect the accuracy of the photogrammetric DTMs were investigated and the relevance of these factors for the interpretation of glacial and periglacial analysis were discussed.

Glacier mass balance calculation

Glacier monitoring aims at improve knowledge about the spatial variability of glacier fluctuations in relation to topographic factors and climatic trends. Different glaciers react in different ways to the same climatic force since their sensitivity depends on their physical characteristics (e.g. size, hypsometry, debris cover, prevalent feeding source) and also on regional climate variability (Kuhn et al., 1985; Oerlemans, 2001; Steiner et al., 2008; Carturan and Seppi, 2009; Abermann et al., 2011). At mid-latitudes (European Alps), a glacier is subject to contributions (accumulation) of snow during the winter and spring due to rainfall and to withdrawals (ablation) over the summer and autumn due to melting. The ice sheet is produced by snow accumulation, which after the processes of compaction, melting, sublimation and refreezing gives rise to ice crystals. In fact, a glacial body is composed by layers, which density increases with the increases of depth. Close to the surface the snow layer has a density around of 50-400 kg/m^3, then the firn layer with a density ranging from 400 to 800 kg/m^3 and below the ice with a density of 800-900 kg/m^3.

Ablation zone or ablation area refers to the low-altitude area of a glacier or ice sheet below firn with a net loss in ice mass due to melting, sublimation, evaporation, ice calving, or erosive removal of snow by wind. The equilibrium line altitude (ELA) or snow line separates the ablation zone from the higher-altitude accumulation zone. A glacier body is a system in dynamic equilibrium with the surrounding environment, this means that it responds to climatic and environmental changes through a variation of its surface and mass. The amount of snow and ice gained in the accumulation zone and the amount of snow and ice lost in the ablation zone during a hydrological year (from October 1 to September 30 of next year) determine glacier mass balance. Therefore, the mass balance evolution of glaciers is the immediate indication of their degree of imbalance in reaction to atmospheric changes (Carturan et al., 2013a). The mass balance of a glacier is quantified in millimetres (or metre) of water equivalent. Therefore, in addition to determining the magnitude of the volumes involved in the snow gains and losses, the snow density has to be known/measured. The latter is usually achieved by sampling each single layer of the glacier. Glacier mass balances of alpine glaciers are stringently determined using the glaciological method based on ablation stakes or snow stakes in the ablation zone which determines the volumetric change of a glacier through surface height measurements (Kaufmann and Ladstädter, 2008). Other variables closely related to the mass balance, such as the ELA and the Accumulation Area Ratio (AAR, the ratio between the accumulation area and total area) can be used to assess the direct impact of climate change or the degree of imbalance of glaciers with respect to current climate conditions (Carturan et al., 2013a). However, in high mountain environment, the presence of avalanches, debris cover and topographic shading leads to a spatial distribution of the mass balance (Braithwaite and Raper, 2009).

The geodetic method is an ‘indirect’ method for the determination of mass balance of glacier calculated from the total volume change ΔV (m^3) that occurs between two consecutive survey epochs (Kaufmann and Ladstädter, 2008; Cogley et al., 2011). The geodetic method in comparison to the glaciological method allows to increase the spatial coverage and to provide the total volume change also considering steep zones difficult to assess and processes not measured at the surface like the basal melting. (Cogley, 2009; Carturan et al., 2013a). Additionally the method can also be used to analyse the spatial pattern of glacier thickness changes over large regions (Haeberli et al., 2007). The multi-temporal differencing of DTMs acquired by ALS is becoming a common technique for the calculation of volume change, especially over large and/or remote areas, such as avalanchefed and debris-covered glaciers (Carturan et al., 2013b). For restricted areas like smaller glaciers ground-based TLS are being increasingly used since they provide the possibility to quickly (and safely) survey entire ice bodies from a few points, obtaining high resolution data. The reader is referred to the review papers of Avian and Bauer, (2005), Gelmini et al. (2005), Kellerer-Pirklbauer et al. (2005), Tamburini et al. (2007), Schaffhauser et al. (2008), Avian et al. (2009), Carturan et al. (2011) for more details.

For the annual mass balance estimation of the studies glaciers, the geodetic method using multi-temporal differencing of DTMs was calculated using both LiDAR and SfM-photogrammetry as following:

$$\Delta V = \overline{\Delta Z} \cdot A \tag{4.1}$$

where $\overline{\Delta z}$ is the average elevation change between two DTMs over the area A of the glacier. The area-averaged net geodetic mass balance in meters of water equivalent per year (m w.e. y^{-1}) was calculated as

$$\dot{M} = \frac{\Delta V \cdot \rho}{A} \tag{4.2}$$

where ρ is the mean density.

Surface changes of rock glacier

Rock glaciers are lobate to tongue-shaped bodies composed of a mixture of rock (coarse grained debris layer) and ice (interstitial ice cement, ice lenses or a core of massive ice) (Barsch, 1996). Rock glaciers are a creep phenomenon of alpine/mountain permafrost and must not be confused with debris covered glaciers. Their monitoring is important to understand the effect of ongoing climate change on slope dynamics (Dall'Asta et al., 2015). Active rock glaciers are slowly creeping downhill by internal deformation of ice and force of gravity. The upper layer composed by rock is the active layer and typically, the front of intact rock glacier is straight and steep. Due to the physical properties of ice the annual flow velocities are in the range of centimeter to meters. The flow velocity and the thickness of the rock glacier are strongly influenced by climatic parameters (i.e. temperature and precipitation, in particular water) and by internal composition (contents of ice and debris) (Kääb et al., 2007).

Their dynamics have so far not been investigated in detail (Kenner at el., 2013). Three common methods used to observe surface changes are digital airborne photogrammetry and more recently TLS and ALS. As mentioned above, single point GPS measurements can be used to obtain precise reference data or to observe the kinematics of spatially limited areas (Lambiel and Delaloye, 2004). Elevation changes in DTMs are used for estimate of rock mass waste, but do not reveal information about displacement directions and rates of mass movements. Photogrammetry is mainly used for the detection of horizontal creep rates of rock glaciers over several decades (Kääb et al., 2003) while ALS/TLS allows to obtained information in each directional component with high accuracy and resolution. However several methods can be combined to measure surface movements. Kääb and Vollmer (2000) were one of the first to set up a digital photogrammetric workflow for area-wide mapping and monitoring permafrost geometry, thickness changes and surface creep based on multitemporal orthophotos. They developed a software system called CIAS for the calculation of creep rates based on image correlation between two images that is able to detect the corrispodingfeatrues by searching for example similar texture in two imges. These techniques were widely used for glacier ice velocity measurements based on optical satellite images (Scambos et al., 1992; Haug et al., 2009). Image correlation can also be applied on shaded relief images derived from ALS DTMs instead of optical images (Fey et al., 2015). Recently, Kernel et al. (2013) extracted 3D surface change of a rock glacier complex through comparison of multitemporal laser scanning data (both ALS and TLS) and digital airborne photogrammetry (orthophoto). Dall'Asta et al. (2105) reconstructed the surface of an Italian rock glacier with SfM-UAV technique and calculated the biennial displacements via manual identification and automatically tracking of corresponding features between the generated SfM orthophoto.

In this study, to assess the AVDM3 Rock glacier kinematics, the vertical elevation differences between DTMs derived from airborne and SM-photogrammetry and manual feature tracking of feature identified in the shaded DTMs were calculated.

4.2 MONTASIO OCCIDENTALE GLACIER CASE STUDY

The purpose of this case study is to apply the SfM-MVS approach based on terrestrial images for monitoring and calculating of the mass balance of the Montasio Occidentale glacier, one of the lowest glaciers of the European Alps. The Montasio Occidentale is a good example of small (i.e. >0.5 km^2), debris-covered and avalanche-fed glaciers that are common in some regions of the Alps (e.g. in the Dolomites), but which are still poorly understood in terms of their reaction to climate change. In addition, this glacier is an interesting case study as it is located in a geographic area with high precipitation, where important differences are expected to exist in the behaviour and sensitivity of glaciers compared with other (drier) areas of the Alps (Carturan et al., 2011). However, access to the glacier with terrestrial laser instrumentation is not possible without the support of the helicopter, limiting, for reasons of costs, the monitoring of the area. Other terrestrial survey techniques like GPR survey or GPS are limited by the presence of rock walls that reduce the GPS signals. For that reason the SfM-photogrammetry could be a feasible solution for annual surveying of the glacier by delivering data quality and resolutions which are comparable with traditional survey methods but with a very low-cost capital instrument (hardware and software) and straightforwardness of the methodology. This work presents a comprehensive photogrammetric survey carried out in October 2012, September 2013 and October 2104 to characterize the glacier in its current state (area, volume and degree of activity) and to establish a baseline for the reconstruction of historical fluctuations and for future monitoring using this methodology.

4.2.1 Study area

The Montasio Occidentale Glacier (46° 26′ 09″ N; 13° 26′ 09″ E, World Glacier Inventory ID number: I4L0003005; Haeberli et al., 1989) is located in the Italian Julian Alps (Eastern European Alps), near the boundaries with Austria in the north and Slovenia in the east. The glacier is cone-shaped and occupies a cirque located at the base of the north walls of Mount Jôf di Montasio [2754 m a.s.l.] (Fig. 4.1). The elevation ranges from 1860 m to 2050 m a.s.l. with an average value of 1910ma.s.l. The glacier covers an area of 0.068 km^2 (maximum length of 350m; maximum width of 280 m); the major source of nourishment is avalanche snow from the overhead rock walls. The glacier is currently composed of an upper, steep accumulation area and a lower, gently sloping ablation area that is covered by debris (Carturan et al., 2013b).

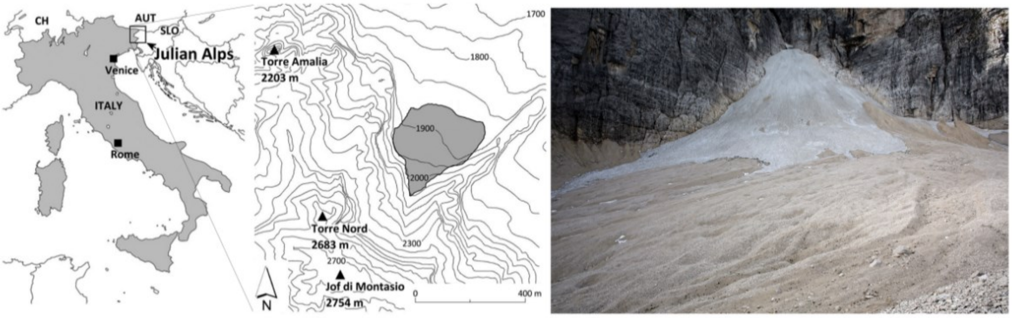

Figure 4.1. Geographic setting of Montasio Occidentale Glacier and view of the glacier from the moraine on 26 September 2013. The lower part of the glacier is completely covered by debris.

4.2.2 Methods

The Montasio Occidentale Glacier was simultaneously surveyed using the photogrammetric technique and a TLS on two different dates: 5 October 2012 and 26 September 2013 (Fig. 4.2). The TLS-based DTMs were used as a reference to estimate the quality of the photogrammetric results. Additionally, in 2014 a photogrammetric survey on October 25 and a GPR survey on October 29 were carried out in order to estimate the snow depth. This section describes how the data were acquired and processed.

Figure 4.2. The Montasio Occidentale Glacier during the photogrammetric surveys of 5 October 2012, 26 September 2013 and 25 October 2014.

TLS data acquisition and processing

In both survey epochs, the scans of the glacier were acquired with a Riegl LMS-Z620 TLS (Riegl, Horn, Austria). Measurements were performed from two scan positions located over the Little Ice Age (LIA) terminal moraine, which provided a good angle of incidence for the study area and a good overall coverage of the catchment (Fig. 4.3). The spatial resolution ranged from 0.1 to 0.3m at 300m from the scanner. To register the two TLS scans and georeference the TLS surveys in the global coordinate system UTM-WGS84, zone 33N, laser scanning targets were employed. Their positions were surveyed by dGPS measurements using dual frequency GPS/GLONASS receivers

(Topcon HiPer PRO; Topcon, Tokyo, Japan). TLS and dGPS data acquisition required approximately five hours on both survey dates. A total of 4,180,417 points were collected inside the glacier area during the October 2012 survey and 3,511,071 points were collected during the September 2013 survey, with a point density of 62 pts m^2 and of 53 pts m^2, respectively. The point clouds were processed with the Riegl RiScanPro software and interpolated with ESRI ArcGIS (ESRI, Redlands, CA) to generate the DTMs. To avoid errors due to global shifts or rotations between the two DTMs, the TLS 2013 point cloud was co-registered on the TLS 2012 point cloud using the ICP algorithm by considering the stable areas outside the glacier. The co-registration has provided a RMSE of 0.017 m and an average value of 0.025 m (0.049 m maximum value). The accuracy of the two TLS-based DTMs was estimated by computing the elevation difference between the DTMs of the two surveys on stable areas outside the glacier; a mean residual distance of 0.07m with a standard deviation (σ) of 0.13m was obtained.

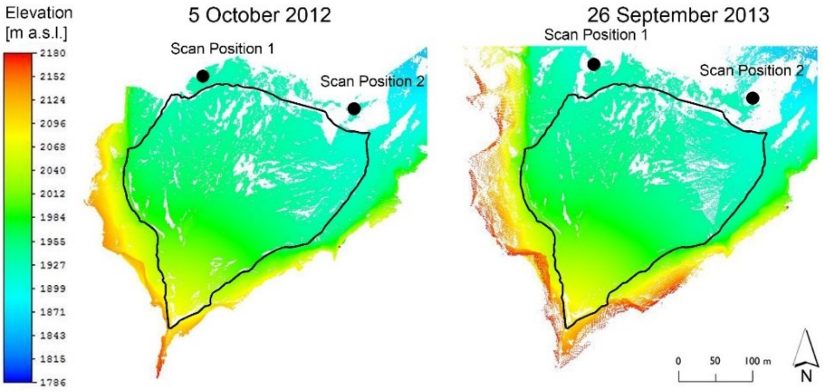

Figure 4.3. The terrestrial laser scanning (TLS) point clouds of 5 October 2012 and 26 September 2013. The black line represents the glacier perimeter while the black points denote the two scan positions.

Ground Penetrating Radar (GPR) data acquisition and processing

The GPR survey was performed on 29 October 2014 using a shielded 300 MHz antenna connected to a Zond GPR. GPR data acquisition, processing and results interpretation were provided by Colucci and Forte (University of Trieste, Italy). The GPR profile was 250m long with a constant 5 cm trace interval triggering the instrument with an electro-mechanic odometer, while the positioning was obtained by using an RTK GPS. The direction of acquisition is from North-Est toward South-West. The profile was processed applying a standard flow which includes zero time correction (drift removal), background removal, bandpass filter, amplitude recovery based on the inverse mean decay function, velocity estimation based on diffraction hyperbolas fitting, topographic correction, Kirchhoff time migration, depth conversion. The mean velocity of the first layers down to an internal debris level was estimated in 20 cm/ns (ε_r=2.3), corresponding to a density value of about 600 g/dm3. The results highlighted three main reflectors interpreted as: the bottom of the shallowest snow/firn layer (cyan), the bottom of the firn almost without debris inside (green), and the bottom of the firn (i.e. the top of an internal debris layer, in purple). A crevasse has been imaged in the uppermost part of the profile (in grey) (Fig. 4.4).

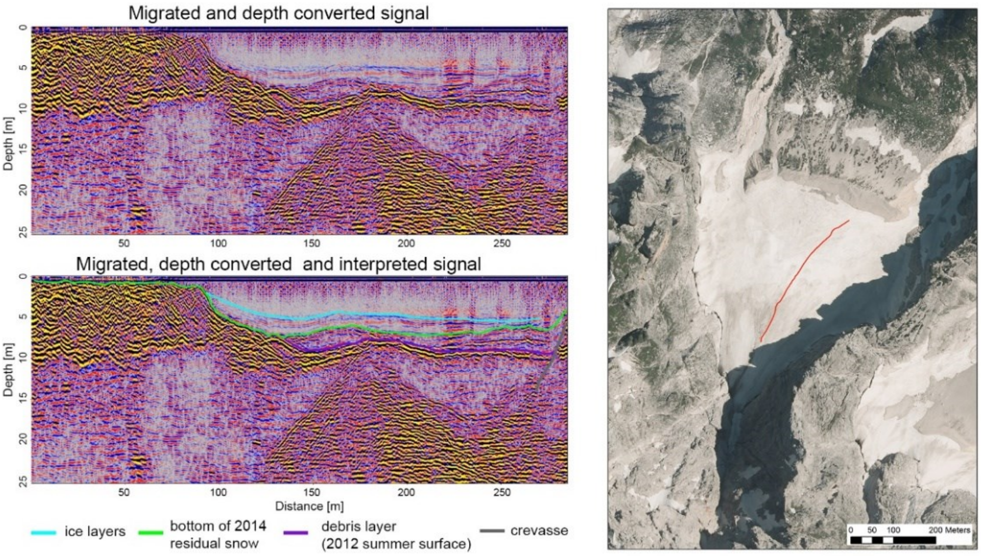

Figure 4.4. GPR measurements and GPR profile.

Photogrammetric data acquisition and processing

Data acquisition

The three ground-based photogrammetric surveys were conducted by adopting different data acquisition settings, which are summarized in Table 4.1. The survey of 5 October 2012 was carried out using a Nikon D5100 SLR digital camera with 16 megapixel resolution, equipped with a lens of 10 mm focal length chosen to have a great angle of view. The acquisition was made trying to ensure a large overlap between the photos, taking 35 images from the lower part of the glacier (Fig. 4.5), with an average baseline of 14 meters. The acquisition required about one hour. For the second survey of 26 September 2013 it was decided to use a camera with higher resolution and a much shorter average baseline among the camera positions. A full-frame camera CANON EOS 5D with 22 megapixels was used, equipped with a lens of 28 mm focal length. The images were taken with an average baseline of 3 m, trying to ensure a greater overlap between images (Fig. 4.5). Consequently, a much larger number of images was acquired (347 in total) whose acquisition required around three hours. Based on the results of the 2013, similar settings in term of camera focal length and baseline were adopted to acquire the images in 2014. During this survey a larger number of images were acquired in the lower part of the glacier in order to increase the spatial coverage of the surface that it is characterized by a very articulate morphology. Different light condition and surface coverage have characterised the three photogrammetric surveys. In 2012, the presence of low fog has limited the acquisition of the images reducing strongly the visibility of the glacier and the surrounding rock walls. In 2013 survey, the direct sunny light was predominant on the lower part of the glacier. This provided strong shadows on the surface and therefore different images texture. The last survey was achieved under a perfect weather and light condition with a diffuse illumination given by cloudy sky. In 2012 and 2013, the debris layer covered the lower part of the glacier with the presence of supra-glacial features like debris deposit in the middle part. In 2014, the glacier surface included the debris covered area was completely covered by dirty snow with a visible presence of deep crevasses.

Table 4.1. Data acquisition settings for the photogrammetric surveys.

Photogrammetric surveys						
Survey epoch	Camera type	Camera Resolution *[Mpix]*	Focal Length *[mm]*	Nb. Images	Average baseline *[m]*	Acquisition Time *[hour]*
5 Oct. 2012	Nikon D5100	16	10	35	14	1
26 Sept. 2013	Canon 5D Mark III	22	28	347	3	2÷3
25 Octo 2014	Canon 5D Mark III	22	28	489	3	2÷3

Data processing

The surface reconstruction of the Montasio Occidentale Glacier was realized following the SfM-MVS workflow shown in Figure A2. (Appendix A). The preliminary step of the adopted workflow was identified the GCPs in the image in order to include these constraint into the bundle adjustment. Due to logistical constrains and safety issues, no artificial targets could be placed on the glacier surface for the georeferencing of the photogrammetric models. However, this task was accomplished using the 3D coordinates of 13 GCPs, which were properly selected on the 2012 TLS point cloud and the images. Then, the extraction of matching points, the calculation of the camera positions and the generation of the sparse point cloud were automatically provided by the software with the step of cameras alignment. The results are shows in Table 4.2 for each survey. The average transformation residual error (i.e. the distance between the input and estimated positions of the GCPs; AgiSoft LLC, 2010b) calculated by the software for the 13 GCPs was around 80 cm (Table 4.2). The major contribution to this error may be attributed to the manual identification of the GCPs on the TLS point clouds and the images.

The images resolution selected to perform the dense point cloud reconstruction was different for the three dataset. The small number of processed photographs for the 2012 survey enabled the use of images at full resolution (image quality parameter set to ‘ultrahigh’), which resulted in an average pixel size on the ground (GSD) of 0.096 m. Due to the larger number of photographs and their higher resolution the dense point clouds of the 2013 and 2014 survey were generated with the image quality set to 'medium' to limit the memory requirements and the processing times. Consequently, all images were downsized by the software to 25% before their processing, which resulted in an average GSD of 0.11 m and 0.12 for the 2013 and 2014, respectively (Table 4.2). In this study, the choice of the smoothing filter for the dense point cloud reconstruction has affected the final spatial coverage and the 'mild' filter has proven to be better in term of the number of reconstructed points. Camera orientation, GPS position and dense point cloud reconstruction for each epoch are shown in Figure 4.5.

After the 3D models reconstruction, the outliers and noisy peaks of the photogrammetric point clouds were manually removed. To reduce the error of the adopted georeferencing method, the ICP algorithm was applied to co-register the point clouds in the stable area outside the glacier, using the TLS 2012 point cloud as a reference (the same point cloud used to select the GCPs). ICP registration was performed in Cyclone 8.0 software, and the RMSE is provided in Table 4.3 for each dataset.

Table 4.2. Average transformation residuals error [m] and RMS reprojection error for the GCPs [pix] after the georeferencing of the dense 3D point clouds.

SfM-MVS results							
Survey epoch	Average Reprojectior error *[pix]*	15 GCPs error		GSD	Image Reconstruction quality	Point Count	
		[m]	*[pix]*	*[m/pix]*		*from PS*	*after filtering*
2012	0.47 (0.99 max)	0.79	0.98	0.09	18 Mpix (Ultrahigh)	21,610,898	15,450,237
2013	0.36 (2.41 max)	0.78	1.20	0.11	6 Mpix (Medium)	23,620,740	17,912,656
2014	0.37 (2.31 max)	0.81	0.86	0.12	6 Mpix (Medium)	23,113,918	16,154,854

Table 4.3. ICP registration error. The 2012 TLS point cloud was set as fix.

Survey epoch	**ICP registration**					
	SfM-MVS point cloud			TLS point cloud		
	RMSE	*Mean*	*Max.*	*RMSE*	*Mean*	*Max.*
2012	0.052	0.025	0.890	0.017	0.013	0.049
2013	0.021	0.017	0.050			
2014	0.022	0.08	0.049			

4.2.3 Results

The co-registered point clouds obtained in 2012, 2013 and 2014 by ground-based photogrammetry and the TLS point cloud were interpolated into DTMs with a cell size of 0.2 m x 0.2 m using ArcGIS software. This spatial resolution was selected as a reasonable compromise between the size of the resulting data files and the capability of accurately representing the surface features on the glacier. A visual comparison between the hillshaded DTMs obtained with both surveying techniques is shown in Figure 4.6. Areas without information (blank zones in Figure 4.6) were masked and not interpolated while converting point clouds into DTMs. The spatial coverage of the photogrammetric DTMs was 47% in 2012, 95% in 2013 and 97% in 2014; for the TLS-based DTMs, the spatial coverage was 84% and 82% in 2012 and 2013, respectively. The lower part of the glacier, which is covered by fine debris, could not be reconstructed from the 2012 dataset with the SfM-MVS method, as no matching points were calculated by PS among photographs of this part of the glacier (Fig. 4.5). Conversely, the collection of a higher number of images with shorter baselines in 2013 and 2014 solved this problem. As shown in the four insets in Figure 4.6, both survey techniques enabled the identification of the main supra-glacial features. In the 2013 survey, the noise was comparable for TLS and SfM-MVS; in the 5 October 2012 survey, the noise for the SfM-MVS was significantly higher than the noise for the TLS.

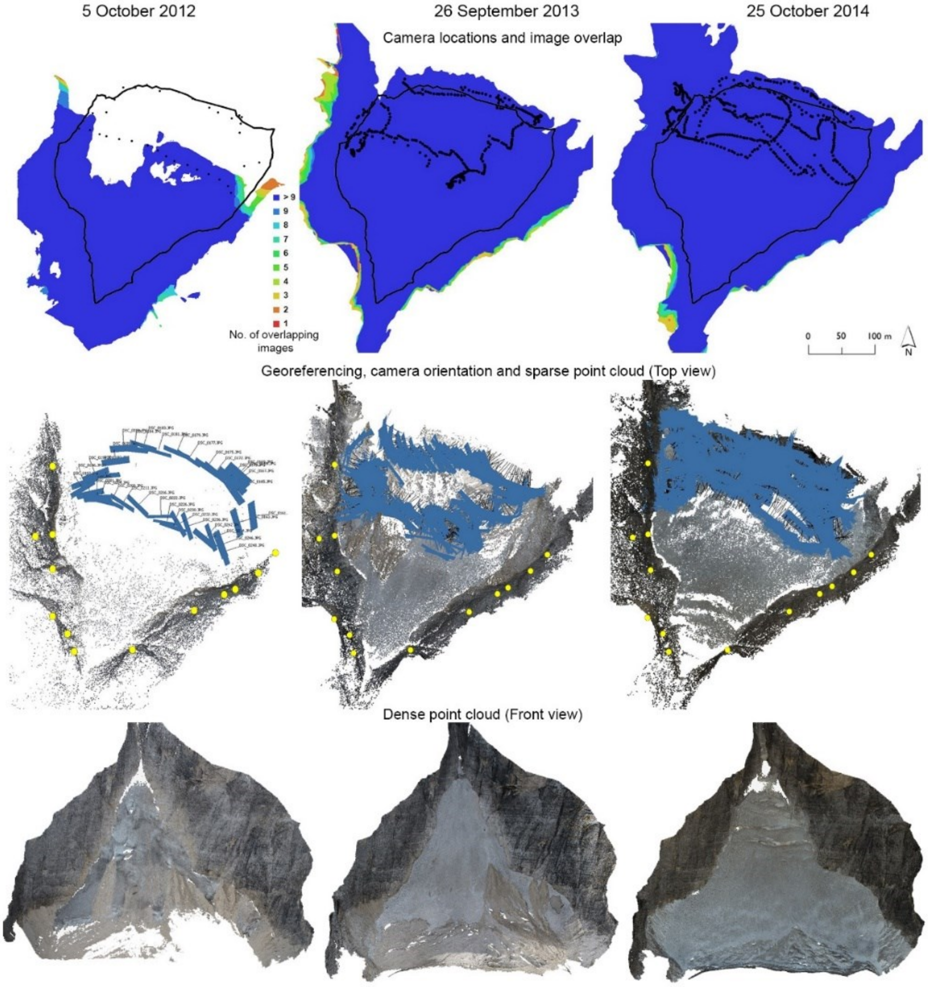

Figure 4.5. Results of photogrammetric surveys of the Montasio Occidentale Glacier carried out on 5 October 2012, 26 September 2013 and 25 October 2014. The image processing was performed in PhotoScan. Top: the acquisition geometry and the image overlap for each photogrammetric survey. Center: the SfM result with the georeferencing, the camera orientation and the sparse point cloud for each survey (top view). Bottom: the generated dense point clouds with MVS algorithm (front view of the reconstructed glacier surface). Black dots represent the camera positions and yellow dots are the GCPs.

Accuracy assessment of the SfM-MVS DTMs according to the TLS-based DTMs

The accuracy of SfM-MVS DTMs was assessed by calculating the digital elevation model of difference (DoD) between the photogrammetric and the corresponding TLS-based DTM for each survey epoch. The latter was employed as a reference for the comparisons, given the high accuracy of TLS measurements confirmed by previous applications in our study area (Carturan et al., 2013b). The calculations were performed in the common coverage areas. At the time of the surveys, the upper part of the glacier was covered by snow and firn, whereas the lower part of the glacier was covered by fine-grained debris (Fig. 4.2). As the SfM-MVS approach is significantly affected by the quality of the image texture, which varies according to the different substrata, the photogrammetric reconstruction accuracy was also separately evaluated for the snow-firn and debris areas, whose extents were outlined in ArcGIS using the orthophoto exported from PS. The spatial distribution of the elevation differences between photogrammetric and TLS DTMs appears clustered in 2012 and more homogeneous in 2013 (Fig. 4.7). The spatial pattern observed in the DoD of 2012 suggests a residual horizontal shift between the photogrammetric DTM and the terrestrial laser scanner DTM. The average elevation difference and the standard deviation of the reconstructed glacier area for the 2012 comparison were 10 cm higher than the 2013 results which provided a mean value of 0.02 m with 10 cm of standard deviation. Outside the glacier on the stable area, the standard deviation of the comparison with the TLS DTMs was higher in 2012 but with lower mean value. However, this result is influenced by the smaller extent of the stable area outside the glacier. The frequency distribution histograms extracted from the DoDs (Fig. 4.7) reveal a normal distribution of the elevation differences in both survey dates, but show a considerably lower dispersion around zero in 2013 compared with 2012: 61% of the cells fall in the range ±0.2m in 2012, whereas the percentage increases to 95% in 2013. In 2013, the standard deviation of the elevation differences over debris was two times the standard deviation of the elevation differences over snow-firn (Table 4.4). Similar results were obtained for 2012 comparison although this result is influenced by the smaller extent of the debris area compared with the snow-firn area (Table 4.4).

In terms of spatial coverage and the standard deviation of the elevation differences versus TLS, better results were obtained with the SfM-MVS approach in the snow-firn covered part of the glacier. To identify the main factors that affect the accuracy of the photogrammetric model, the effects of imaging incidence angle, slope and point density analysing their correlation with the elevation differences between photogrammetric and TLS DTMs were investigated. The incidence angle represents the angle between the incident line of sight of the camera and the vector normal to the surface. For both studied years, the 90% of incidence angles range between 60° and 90°. Examining the influence of these angles on the elevation difference, no significant relationship was identified (R^2 = 0.0017 and 0.0011 in 2012 and 2013, respectively). Similarly, no statistically significant relationship was detected between slope and elevation difference (R^2 = 0.0426 and 0.0316 in 2012 and 2013, respectively), and between point density and elevation difference (R^2 = 0.0014 and 0.0125 in 2012 and 2013, respectively).

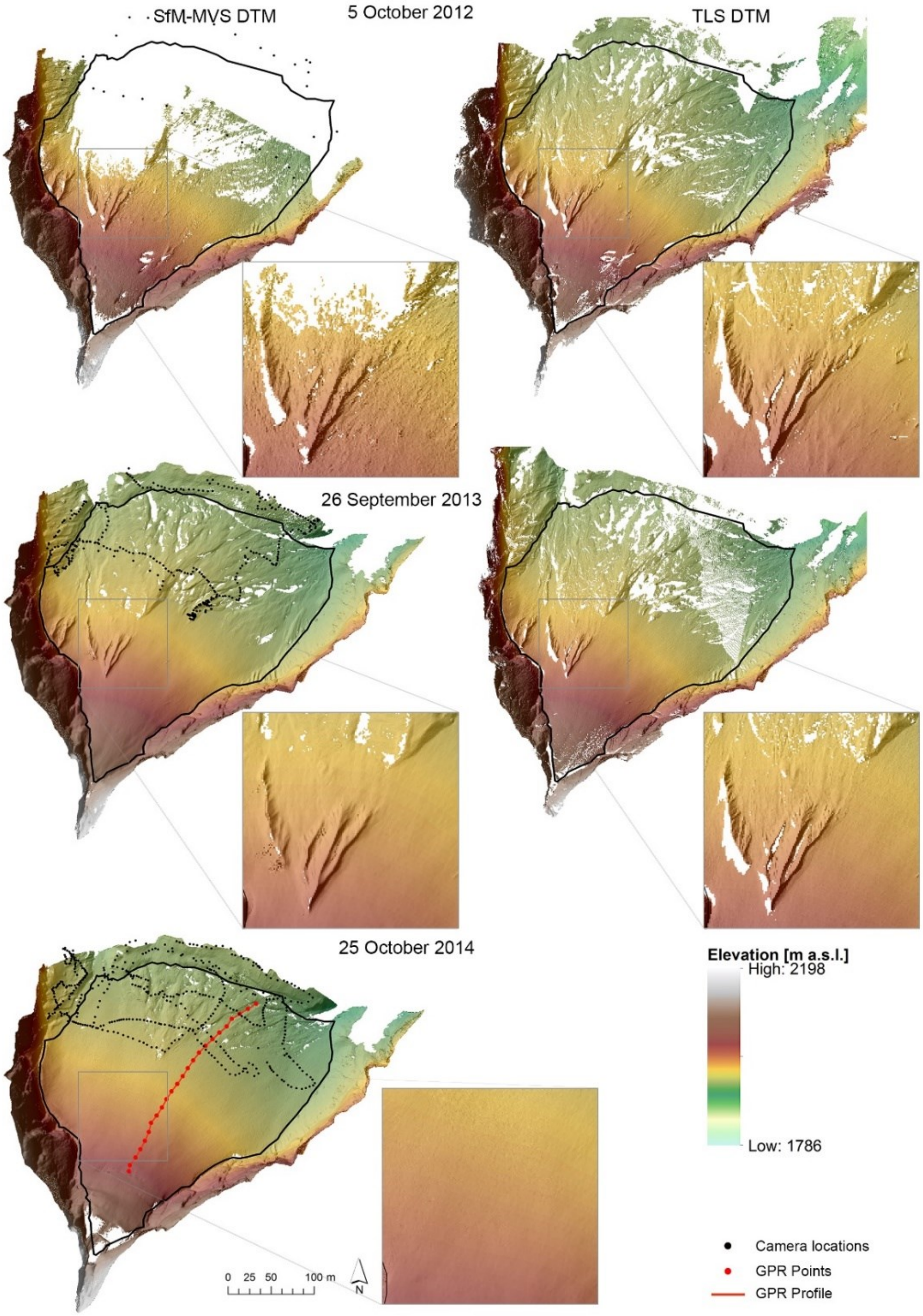

Figure 4.6. Hillshaded digital terrain models (DTMs) of Montasio Occidentale Glacier derived from photogrammetric (left) and TLS (right) measurements in 5 October 2012, 26 September 2013 and 25 October 2014.

These analyses suggest that in this case study, the accuracy of SfM-MVS DTMs is not influenced by incidence angle, slope, point density and type of substrata. This finding infers that the quality of the photogrammetric results and the completeness of the point cloud are primarily dependent on the image network geometry and the camera characteristics, as suggested by Wenzel et al. (2013) and Dai et al. (2014).

The results of the SfM-MVS approach were also compared with the TLS data in terms of point cloud densities (Fig. 4.8). The photogrammetric method can produce point cloud densities that exceed the point cloud densities derived from TLS measurements. The average density obtained by photogrammetry was 113 pts m^2 for the survey of October 2012, 112 pts m^2 for the survey of September 2013 and 113 pts m^2 and 98 pts m^2 for the survey of October 2014. By comparing with the TLS, the average density was 62 pts m^{-2} and 53 pts m^{-2} in 2012 and 2013, respectively. Considering the strong downsizing (25%) applied to the 2013 and 2014 photographs in the processing step, the point density that is potentially achievable in this case study with the SfM-MVS method is much larger than the point density obtained by the TLS used. As illustrated in Figure 4.8, no distinct relationship seems to exist between the camera-object distance and the point density. The highest point density in the SfM-MVS point cloud was obtained in the upper part of the glacier, which is located far from the camera positions. In this portion of the glacier, the SfM-MVS point cloud is denser than the TLS point cloud. Conversely, the different type of substrata on the glacier affect the point density, which is characterized by higher values and lower spatial variability over snow–firn (105 pts m^{-2}), compared with debris (131 pts m^{-2}).

Table 4.4. Results of comparisons between SfM-MVS-based DTMs vs. TLS-based DTMs in the common area for the entire glacier, for the two different substrata (snow-firn and debris) and for the stable area outside the glacier.

Elevation difference (DoD) between SfM-MVS and TLS –DTMs common coverage area										
Common area	**5 October 2012**					**26 September 2013**				
	Min.	*Max.*	*Mean*	*σ*	*RMSE*	*Min.*	*Max.*	*Mean*	*σ*	*RMSE*
Glacier										
All glacier	- 17.732	+ 6.333	+ 0.096	0.286	0.302	- 2.377	+ 3.648	+ 0.024	0.097	0.100
Snow-firn	- 4.062	+ 6.332	+ 0.037	0.237	0.234	- 2.240	+ 3.536	- 0.013	0.071	0.072
Debris	- 17.734	+ 6.286	+ 0.153	0.316	0.351	- 2.377	+ 3.648	+ 0.029	0.122	0.126
Stable area (off glacier)										
Debris	- 1.482	+ 1.521	- 0.015	0.224	0.225	- 2.077	+ 1.970	+ 0.068	0.132	0.149

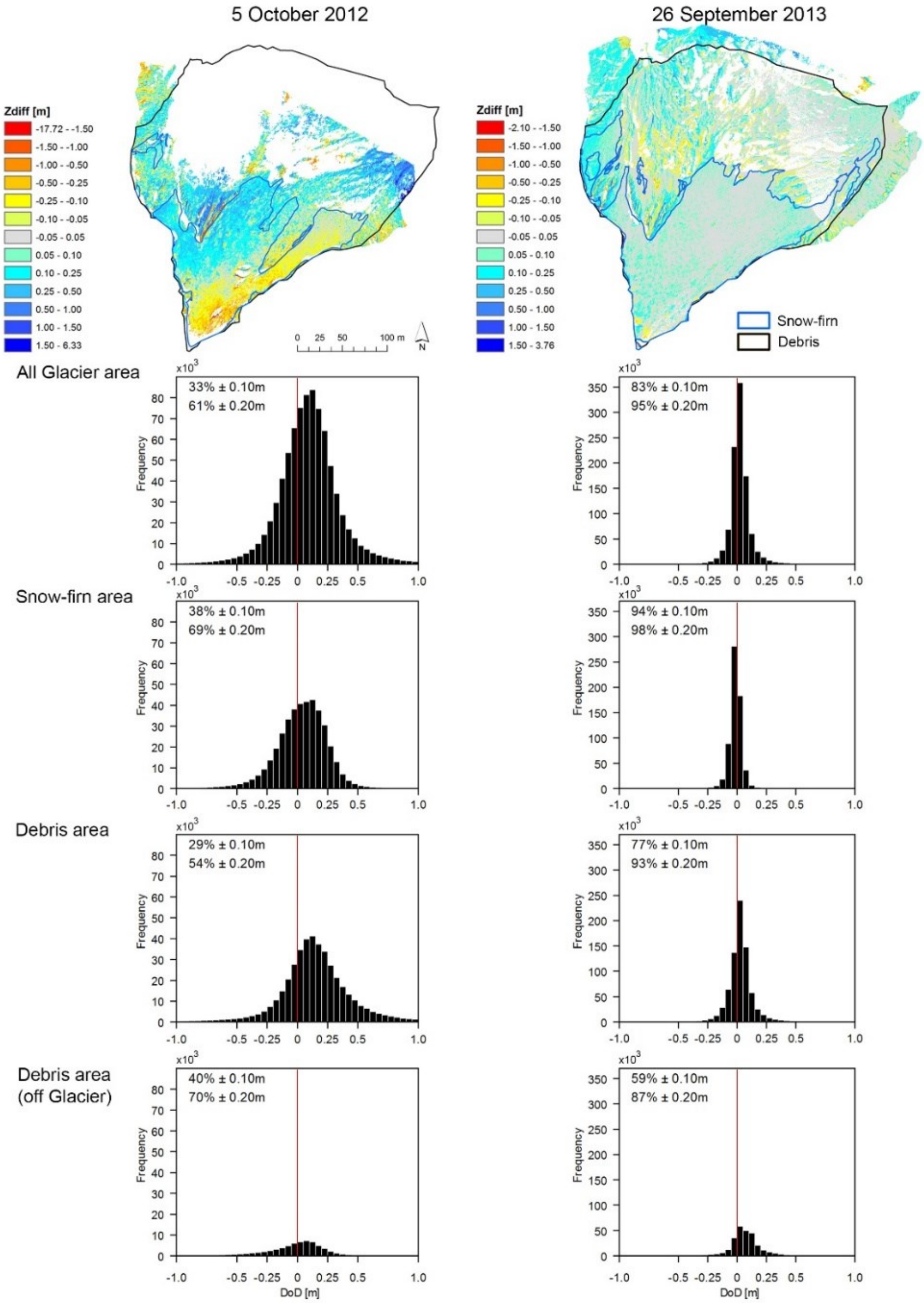

Figure 4.7. Spatial distribution of elevation differences between SfM-MVS and TLS-based DTMs on 5 October 2012 and 26 September 2013. Frequency distribution histograms of elevation differences between SfM-MVS and TLS-based DTMs calculated for all glacier area, and in the two sub-areas covered by debris and snow-firn and in the stable area outside the glacier. The blue line represents the limit between the snow-firn covered area and the debris-covered area inside the glacier.

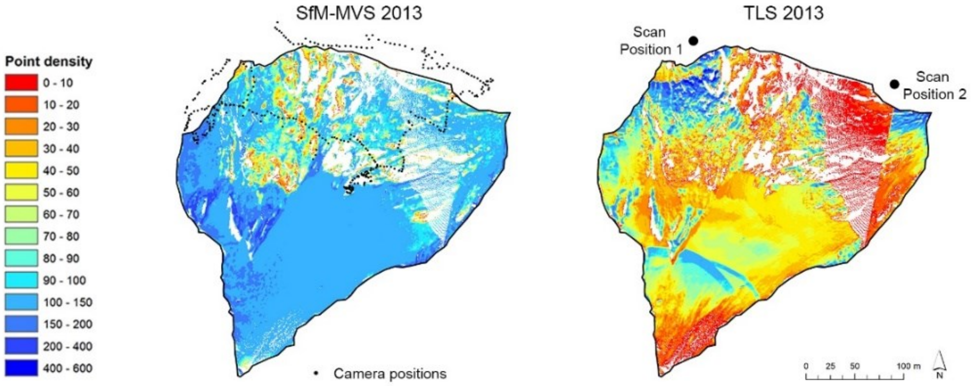

Figure 4.8. Point density map of the glacier surveyed on 26 September 2013 by photogrammetry and TLS. Locations of camera and TLS positions are displayed as black dots.

Mass balance calculation

The geodetic mass balance rate is calculated according to the Equation (4.2). As the extent of the accumulation area increased in the investigated period and the accumulation area ratio (AAR) increased from 0 to 0.40, the mean density was obtained by a fractional area-weighted mean, assigning 900 kg m^3 for the ablation area (Huss, 2013) and 650 kg m^3 for the accumulation area, as directly measured in a snow pit. The resulting weighted mean density was 800 kg m^3. For comparison purpose, the mass balance of 2012 and 2013 using the photogrammetric DTMs was calculated for the common coverage area with the TLS DTMs (Fig. 4.9). However, due to the partial coverage of the SfM-MVS DTM obtained in 2012 (Fig. 4.6), the mass balance between 2012 and 2013 of the entire glacier (by interpolating the missing areas) was estimated using the TLS-based DTMs and the SfM-MVS DTMs 2013 (Fig. 4.10). The volume change evaluated by TLS from 5 October 2012 to 26 September 2013 was +41,908 m^3, the mean elevation change was +0.61 m, and the geodetic mass balance was +0.488 m w.e. Similar results in terms of the spatial distribution and average elevation change were achieved by using the SfM-MVS DTM of 2013 and the TLS DTM of 2012.

Given the visible increase of the glacier volume between 2013 and 2014 (the debris deposits were completely covered in 2014), the annual mass balance of the glacier from 2013 to 2014 was calculated by photogrammetry (Table 4.5). The elevation change between the photogrammetric DTMs was around 4 m with a consequent increasing of the volume of 275,010 m^3.

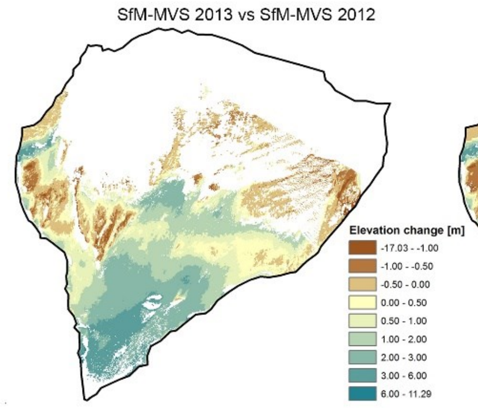

Figure 4.9. Spatial distribution of elevation changes from October 2012 to September 2013 between the two DTMs derived from SfM-MVS and TLS data over the area of the glacier with common coverage.

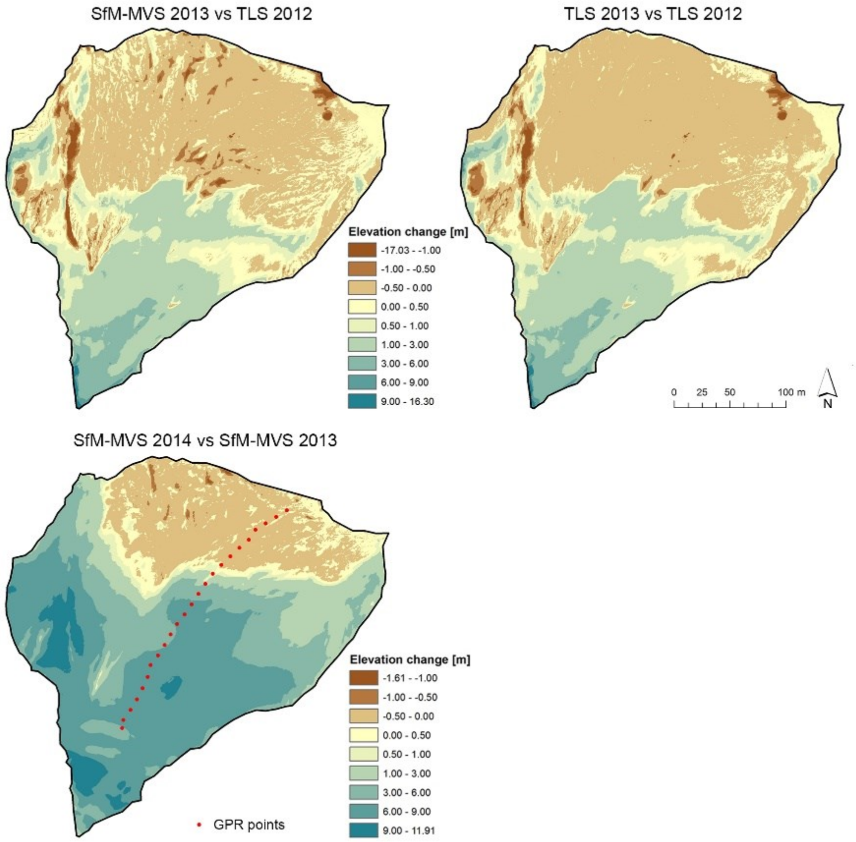

Figure 4.10. Spatial distribution of elevation changes over the entire glacier from October 2012 to September 2013 calculated by TLS DTMs and by SfM-MVS DTM of 2013 and TLS DTM of 2012. At bottom the elevation change from September 2013 to October 2014 between the two DTMs derived from SfM-MVS.

Table 4.5. Statistics of elevation changes and mass balance estimations from 2012 to 2013 and from 2013 and 2014 calculated with both technique in the common coverage area and for the entire glacier.

Elevation change 2013-2012 and 2014-2013								
Epoch	Method	Min. *[m]*	Max. *[m]*	Mean *[m]*	σ *[m]*	Volume change *[m^3]*	Mean density *[kg m^3]*	Mass balance *[m w.e.]*
				Common area 30,953 m^2				
2012-2013	SfM-MVS 2012 - SfM-MVS 2013	- 3.07	+ 9.81	+ 1.07	1.27	+ 33,120	800	+ 0.820
	TLS 2012 - TLS 2013	- 17.04	+ 11.29	+ 1.11	1.19	+ 34,358	800	+ 0.799
				Entire glacier 68,702 m^2				
	TLS 2012 - TLS 2013	- 17.04	+ 16.29	+ 0.59	1.24	+ 40,534	800	+ 0.472
	TLS 2012 - SfM-MVS 2013	- 16.99	+ 16.30	+ 0.61	1.26	+ 41, 098	800	+ 0.488
2013-2014	TLS 2012 - SfM-MVS 2013	- 1.61	+ 11.96	+ 4.04	3.28	+ 275,010	812.5	+ 3.252

Snow depth estimation

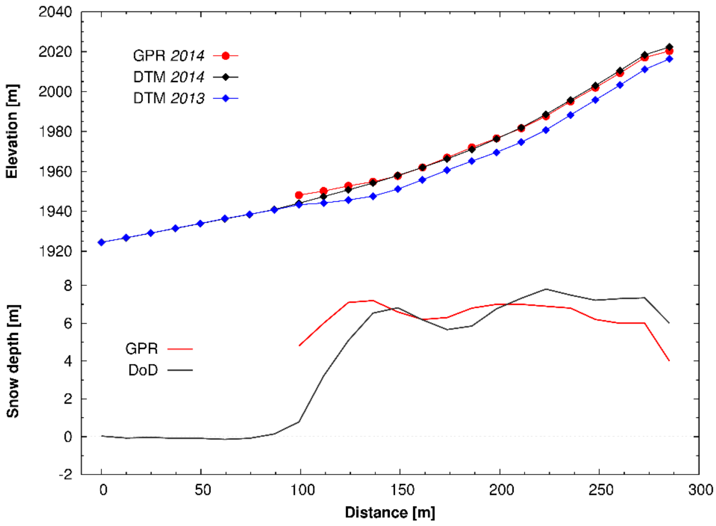

Figure 4.11. Snow depth estimation between 2013 and 2014 along the GPR profile. Comparison of elevation differences between SfM-MVS DTMs with GPR measurements.

The snow depth of the glacier between 2013 and 2014 was estimated by the GPR measurements and by the values obtained along the GPR profile from the elevation change between the SfM-MVS DTMs. The two methods have provided comparable results in term of mean value with 6.30 m measured with the GPR and 6.04 m obtained from the DoD. Also the trend of the snow depth (Fig. 4.11) showed a good correspondence between the two methods but a shift between the two profiles is evident. This shift is also highlighted in the GPR profile of the elevation suggesting an error on the GPR measurements which can be caused by the low accuracy of GPS measurement close to the rock walls.

4.2.4 Discussion

The ground-based photogrammetric method tested in this study has been proven to be an expeditious and efficient technique compared with the alternative solution based on the use of a TLS instrument. The photogrammetric DTMs showed a reasonable qualitative and quantitative correspondence with the TLS-based DTMs (Fig. 4.6 and Fig. 4.7), confirming previous findings reported in the literature (James and Robson, 2012; Westoby et al., 2012; Micheletti et al., 2014). The results obtained in 2012 and 2013 were significantly different. In 2012 the spatial coverage obtained by SfM was lower than in 2013, and the spatial distribution of elevation differences between SfM and TLS DTMs reveal a horizontal shift between the two point clouds, which is not apparent in the average elevation difference (Table 4.4), but can be explained by a distribution which includes both positive and negative biases which approximately compensate for each other (Fig. 4.7). Both the spatial coverage and the spatial distribution of elevation differences between SfM and TLS DTMs were significantly better in 2013, revealing the key role of the improved camera network geometry in the final result of the SfM approach, as already highlighted by previous studies (Remondino and Fraser, 2006; Wackrow and Chandler, 2008, 2011; Bemis et al., 2014; Dai et al., 2014; James and Robson, 2014). In our case study, the homogeneous texture of the lower part of the glacier, which was characterized by a continuous cover of fine debris and rough morphology, affected the completeness of the photogrammetric model reconstructed from the survey of October 2012. This problem was resolved in 2013 by adjusting the camera network geometry and using a higher resolution camera. Smaller baselines between the images were helpful in this case, even if a good compromise has to be reached between base to distance ratios, for ensuring depth precision, and good image similarity, for ensuring good matching performance and spatial coverage (Wenzel et al., 2013). The characteristics of the adopted survey methodology (baseline, degree of overlap, resolution of the images) affected not only the accuracy and coverage of the SfM survey, but also the point density of the final 3D model. Our results showed that the potential point density of the photogrammetric method is significantly higher than the potential point density of the TLS employed in this case study. However, the availability of a large number of data points may generate computational issues within the image processing step. Accuracy assessments based on the elevation differences between the SfM-MVS and the TLS-based DTMs also indicate that the snow-firn area, which is located at the top of the glacier, was less problematic for the photogrammetric method compared with the lower debris area. Mass balance estimation based on the geodetic method was significantly affected by the presence of areas with missing data. To overcome this issue, the capability of the two surveying techniques for calculating the glacier mass balance was assessed over the common coverage areas. These results were encouraging, with almost identical values for both geodetic methods. However, the computation of the glacier mass balance that was only based on the TLS DTMs showed a substantial influence of the lower part of the glacier (ablation zone, missing in the

2012 photogrammetric DTM) in the total estimate. The improvements in the spatial coverage obtained in 2013 demonstrated that the majority of the Montasio Occidentale Glacier can be accurately and completely surveyed using ground-based photogrammetry, with a spatial coverage comparable to the spatial coverage of TLS. Regardless of the employed measuring technique (SfM-MVS or TLS), a higher measurement density enables a better spatial interpolation on small unreconstructed areas without significantly modifying the glacier mass balance estimation (refer to Figure 4.10 for comparison). The same strategy of 2013 and 2014 should be adopted in the future to calculate the mass balance using the photogrammetric data.

4.3 LA MARE GLACIER CASE STUDY

The objective of this application was to test the feasibility of a terrestrial photogrammetric survey for reconstructing the surface of the La Mare Glacier, located in the Ortles-Cevedale Group, Eastern Italian Alps. The adopted ground survey characteristics make this case study an interesting real application of the SfM-photogrammetry in remote area. In fact, the target object covers an area of around 2km^2 prevalently covered by snow, that represents the first challenge for photogrammetric application. The survey was intentionally planned to be as quick and easy as possible. Therefore, in order to carry out the images acquisition safely and replicable over the years, also by non-experts, the access inside the glacier has been avoided. Consequently, the only position accessible to capture the images was the ridge north in front of the glacier. This means that the distance from the glacier to the camera imposed by the topography was up to 2900 m. Based on these characteristics, the acquisition of panorama images was tested in a real application in order to reconstruct from a limited camera positions the entire glacier surface. Two photogrammetric survey campaigns were planned with the aim to calculate the annual mass balance of the glacier by the geodetic method. The accuracy of the photogrammetric DTMs of the glacier was estimated as elevation differences between corresponding ALS-based DTMs in the same reconstructed areas. The main factors that affect the accuracy of the photogrammetric DTMs were also investigated and the relevance of these errors for the interpretation of glacial analysis were highlighted.

4.3.1 Study area

The La Mare Glacier is located in the south-eastern part of the Ortles-Cevedale massif (Eastern Italian Alps), the largest glaciated mountain group of the Italian Alps (Fig. 4.12). The La Mare Glacier (World Glacier Inventory code I4L00102517; WGMS 1989) is a 3.55 km^2 valley glacier currently composed of two ice bodies, which have different morphologies and tend to separate (Carturan et al., 2014). In this work we focused on the southern ice body, which feeds the main tongue. This 2.11 km^2 ice body primarily faces north-east, and its surface is rather flat, with the exception of the small remnant of its valley tongue. The elevation ranges from 2660 to 3590 m a.s.l. Mass balance investigations using the direct glaciological method were started on La Mare Glacier in 2003 and detected an average annual mass balance of -0.76 m w.e. y-1 during the period from 2003 to 2014 (Carturan, 2015). The mass balance was close to zero in 2013 (-0.06 m w.e.) and was positive for the first time since the beginning of measurements in 2014 (+0.83 m w.e.).

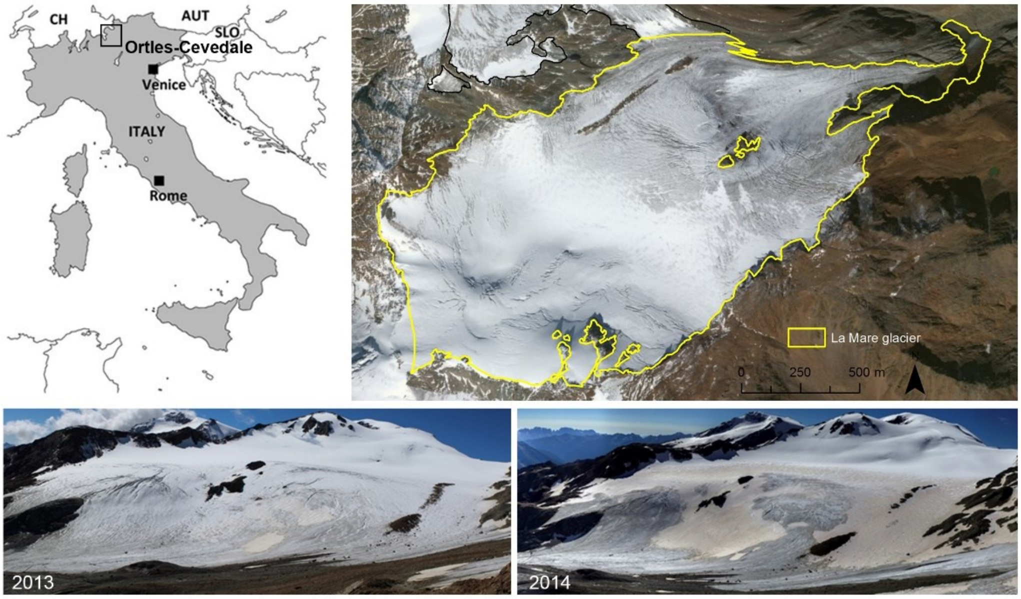

Figure 4.12. Geographic setting of study areas. Panorama view of the La Mare Glacier from the same camera position on 4 September 2013 and 27 September 2014.

4.3.2 Methods

The photo-based reconstruction was used to produce high resolution point clouds and DTMs of the La Mare glacier. In order to estimate the elevation change and calculate the mass balance of the glacier, the images were acquired at the end of the glacier year when also ALS data were available. The ALS data that were used to i) select the ground control points (GCPs) required to scale and georeference the SfM 3D models, ii) co-register the point clouds before producing the DTMs, and iii) validate the photogrammetric results. In this section a description of the photogrammetric surveys and the data processing to produce the dense point clouds and DTMs of the La Mare Glacier are provided.

ALS data acquisition and data processing

ALS flights of the study area were available for 22 September 2013, and 24 September 2014. The technical specifications of the ALS surveys are reported in Table 4.6. To avoid errors due to global shifts or rotations between the individual DTMs, we automatically co-registered the ALS point clouds using a version of the ICP algorithm (Chen and Medioni, 1991; Besl and McKay, 1992) tailored to topographic point clouds (Glira et al., 2015). The LiDAR point cloud acquired in 2013 was treated as a reference only for stable areas outside the glaciers, and snow patches. The 2014 LiDAR point clouds were iteratively fitted to the reference point cloud by applying an affine transformation. The ICP registration of the point clouds produced z-direction residual values of 0.08 m for the 2014 LiDAR point clouds. These accuracies can be assumed to be sufficient for calculating the annual elevation changes of the glacier.

The co-registered point clouds were then converted to DTMs using Natural Neighbours interpolations. A pixel size of 1 x 1 m was produced for the La Mare Glacier based on the LiDAR point cloud density (Table 4.6). To evaluate the relative ALS DTM accuracies after the co-registration, the elevation difference errors of the DTMs were calculated for the stable areas. The standard deviation from the 2013 ALS DTM was 0.19 m for the 2014 DTM comparisons.

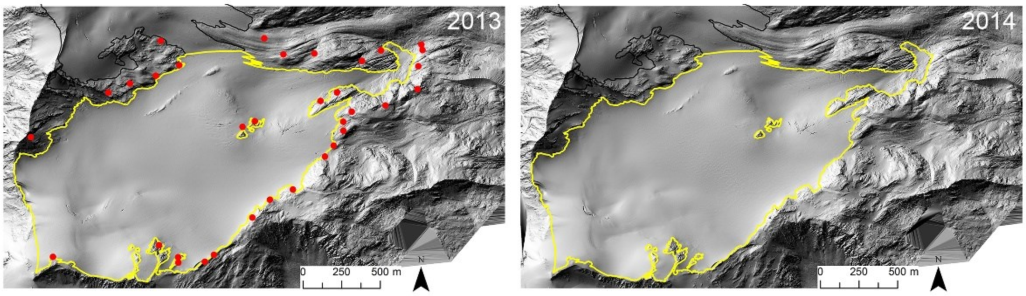

Figure 4.13. ALS shade DTMs of la Mare glacier acquired on September 24, 2014 and September 21, 2013. The red dots represent the selected GCPs in 2013 DTM used in the photogrammetric approach.

Table 4.6. Date and main parameters of available LiDAR data.

Date	Aircraft	Laser scanner model	Laser scanner rate	Max. Scan angle	Scan frequency	Point density *[pts·m^{-2}]*
24 Sept. 2014	Elicopter AS350 B3	Optech ALTM GEMINI (04SEN164)	100 kHz	46°	34 Hz	5.1
22 Sept. 2013	Cessna 404 D-IDOS	ALTM 3100	70,000 Hz	±25°	32 Hz	0.9

Photogrammetric data acquisition and data processing

Data acquisition

The terrestrial photogrammetric surveys of the La Mare Glacier were conducted on 4 September 2013 and 27 September 2014, that is, close to the end of the mass balance year and of ALS flights. The timing of the surveys enabled the calculation of the annual mass balance of the glacier and the ability to compare the results with the ALS-based results. On both days, the sky was clear, with almost no cloud cover. To guarantee a safe and easily repeatable survey of the glacier, we avoided directly accessing its surface, instead performing the survey from a rocky ridge on the north side of the glacier (Fig. 4.14). The elevation of the survey ranged from 3100 to 3300 m in 2013 and from 2600 to 3300 m in 2014. The distance from the glacier surface to the camera positions dictated by the topography ranged between 300 and 2900 m. To cover the entire glacier surface from these positions, the acquired images were panoramic, which involved taking a series of photographs rotating the camera from each individual camera position. In 2013, seven camera positions were used, and 37 photographs were taken with the camera attached to a small tripod to avoid camera shake. In 2014, the number of camera positions was increased to 21, and 177 photos were taken freehand (Fig. 4.14). Both surveys were performed using a SLR Canon EOS 600D. The camera was equipped with a 25-70 mm zoom lens, which was set to a focal length of 25 mm in 2013 and 35 mm in 2014.

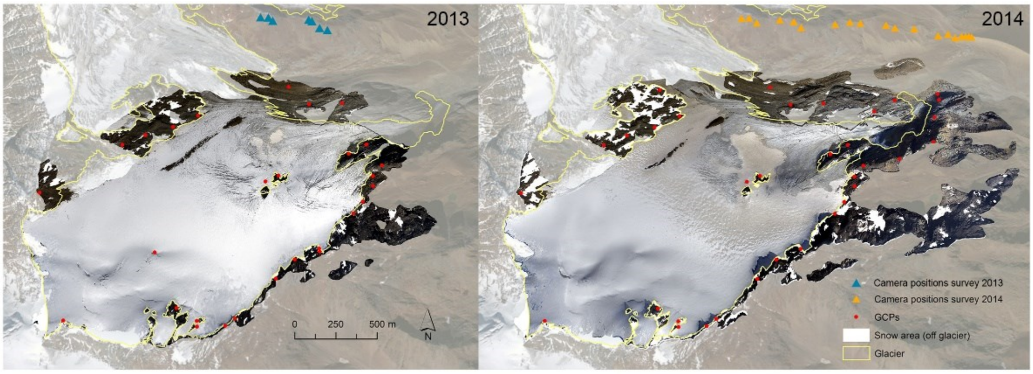

Figure 4.14. Orthophoto-images of SfM-MVS 3D model of La Mare glacier surveyed on 4 September 2013 and 27 September 2014. The white areas in the ortho-images represent the snow-covered area in the rock stable area. The red dots outside the glacier area are the GCPs and the triangles identified the camera locations.

Data processing

The photo-based reconstruction workflow with PS is summarized in Figure A3, Appendix A. The key components of the workflow are 1) acquisition and photograph editing, 2) GCPs identification, image feature detection, matching and 3D scene reproduction (the SfM-MVS steps), 3) point cloud processing, (filtering, subsampling and ICP) and 4) DTM reconstruction. GCPs were selected as natural features in stable area outside the glacier and their coordinates were extracted from the 2013 ALS hillshaded DTM. The GCPs were included into the SfM process to avoid instability in the bundle adjustment solution. The camera was pre-calibrated and the calibration parameters were kept constant during the entire SfM processing given the limits of the camera network geometry and the homogeneous texture of the surveyed terrain. The geo-referenced dense point cloud was reconstructed by the MVS algorithm, using the 'mild' smoothing filter to preserve as much spatial information as possible (AgiSoft LLC., 2010b). To reduce the noise and outliers generated during the dense matching reconstruction (Bradley et al., 2008; Nilosek et al., 2012), an initial filtering was performed in PhotoScan to manually remove the outliers. Further denoising was applied to the dense point clouds exported from PhotoScan, using a specific tool to treat the point clouds. To obtain a uniform spatial distribution of the points, the photogrammetric point clouds (much denser than the ALS point clouds), were down-sampled to 20 cm. Following the same procedure used for the ALS data, the ICP algorithm (OpalsICP, TU Vienna) was applied to co-register the point clouds in the stable area outside the glacier using the 2013 ALS point cloud as a reference. The data acquisition settings and processing results of the photogrammetric surveys are summarized in Table 4.7.

Table 4.7. Data acquisition settings and processing results of the photogrammetric surveys. The GCPs error is the average transformation residuals error [m] and RMS reprojection error for the GCPs [pix] during the bundle adjustment computation. The image quality represents the downsized of the images resolution during the dense matching computation. "Ultra-high" means full resolution, "High" a downsized of 50%. The ground sample distance (GSD) is the average pixel size on the ground. The standard deviation of ICP registration is reported in the table.

SfM-MVS data processing		
	4 September 2013	*27 September 2014*
Input data		
Camera type	Nikon 600D	Nikon 600D
Focal Length	25 mm	35 mm
Image size	5184x3456 pix	5184x3456 pix
N° Images	37	177
Processing data		
Reprojection error	0.43pix (1.76 max)	0.40pix (3.75 max)
GCPs error	1.52 m 1.48 pix	1.14 m 1.96 pix
Image quality	Ultra high	High
Mean GSD	0.16 m/pix	0.22 m/pix
Dense point cloud	49,844,094 pts	55,114,074 pts
Point density	37 pts m^{-2}	20 pts m^{-2}
Post-processing data		
Filtered point cloud /subsampled	15,617,342 pts (sampled 0.20 m)	24,226,221 pts (sampled 0.20 m)
Point density	8 pts m^{-2}	9 pts m^{-2}
ICP transformation	0.14 m	0.15 m

4.3.3 Results

The accuracy of the photogrammetric DTMs was evaluated as mean and standard deviation (σ) of the elevation differences (DTM of Difference, DoD) between SfM-MVS DTMs and ALS DTMs, using the latter as a reference dataset. The primary factors controlling the quality of the photogrammetric DTMs (i.e., camera-object distance, slope and angle of incidence and camera network geometry) were evaluated in terms of DTM accuracy and spatial resolution. After the accuracy assessments, the suitability of using the terrestrial photogrammetric surveys to calculate the annual mass balance of the glacier was investigated and the results were compared with those obtained from ALS surveys.

Accuracy assessment of the SfM-MVS DTMs

DTMs with spatial resolution of 1 x 1 m pixel size were generated interpolating the dense point cloud of La Mare glacier. Snow accumulation in the rock stable area, zone without information and not visible from the camera positions (viewshed analysis) were masked and not interpolated while converting point clouds into DTMs. The shaded photogrammetric DTMs are shown in Figure 4.15. The two photogrammetric DTMs were compared with the ALS data to evaluate their z-differences. Due to the temporal offset between the test and reference data the SfM-MVS DTMs accuracy was estimated in the rock stable area and inside the glacier. For a better evaluation of the photogrammetric accuracy, the elevation change of the glacier between the two survey campaigns with photogrammetry and LiDAR acquisition at the same epoch was estimated. In 2013 the melting of glacier between September 4, (photogrammetric measurement), and September 27, (LiDAR data) was about 50 cm. In 2014, as the glacier was detected by ALS three days after the photos acquisition, the melt rate was up to 10 cm in the lower part of the glacier and a few centimetres at an altitude of 3000-3200 m a.s.l. However, both ALS measurements were carried out following a snowfall (estimated around 10 cm), clearly visible from the hillshaded DTMs, and not present during the photogrammetric surveys.

The mean elevation difference between the SfM-MVS DTM from 4 September 2013 (Fig. 4.16a) and the ALS DTM from 22 September 2013 (Fig. 4.13a), evaluated in the common stable area outside the glacier, was -0.42 m (σ = 1.72 m). The same calculation between the SfM-MVS DTM from 27 September 2014 (Fig. 4.16b) and the ALS DTM from 24 September 2014 (Fig. 4.13b) yielded a mean value of 0.03 m (σ = 0.74 m). In this area, the mean difference between the 2014 and 2013 SfM-MVS DTMs is 0.38 m (σ = 1.73 m), and the mean difference between the respective ALS DTMs is -0.09 m (σ = 0.29 m, Table 4.8). In addition to the higher σ, the 2013 SfM-MVS DTM has a residual average bias of -0.42 m, which must be taken into account in the glacier mass balance calculations. These results show that the photogrammetric survey conducted in 2014, using a higher number of camera positions and photographs and a slightly longer focal length, provided a significant improvement compared to the survey of 2013. Table 4.8 also presents the same statistics for the area of the glacier. However, given that in 2013 the ablation was not negligible between the photogrammetric survey of 4 September and the ALS survey of 22 September, the comparison between SfM-MVS and ALS of the same year is meaningful only in 2014, with a mean difference of 0.23 m (σ = 0.65 m). The comparison of the two ALS DTMs of 2014 and 2013 yields a mean difference of 1.30 m for the glacier, attributable to the positive mass balance experienced by the glacier in that time period (+ 0.83 m w.e., Carturan, 2015).

The spatial distribution of the z-distance between SfM-MVS and ALS DTMs at the same epochs is provided in Figure 4.16. The map shows a clustering of the z-differences that it is evidence of bias of the photogrammetric 3D models. For both comparisons, the error distribution inside the glacier is not apparent in the average elevation difference, which includes positive and negative values that approximately compensate for each other. The minimum and maximum values of differences indicate the presence of big outliers both negative and positive also after outlier removal. The higher z-error >±10 m are located in restricted rock areas where varying and steep topography have influence in elevation differences values. The z-distance, commonly applied in geomorphometric studies, is less suitable for quantifying differences in steep areas with slope angles higher than ~ 50° (Fischer et al., 2011). However, due to the limited spatial coverage of stable area outside the glacier the steepest cells of DTMs were not excluded during the DoD calculation. The influence of the slope angle of the surface on the SfM-MVS DTMs accuracy is much more evident in the section profile (Fig. 4.17). High variations of elevation difference up to 1 m are visible in the steep bare-ground reconstructed area. However evidence of systematic and random errors is visible in both substrata.

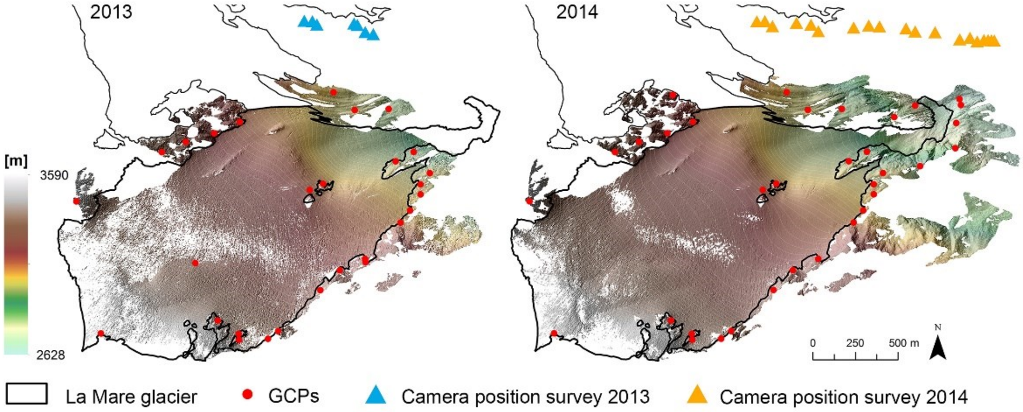

Figure 4.15. Hillshaded DTMs of La Mare glacier derived from photogrammetric measurements on (a) 4 September 2013 and (b) 27 September 2014.

Table 4.8. Results of comparisons between SfM-MVS-based DTMs vs. ALS-based DTMs in the common area and for the bare-ground stable area and glacier.

Elevation differences [m] cell size 1 m x 1m										
DTMs			Common SfM-MVS bare-ground area				Common SfM-MVS glacier area			
			Min	*Max*	*Mean*	*σ*	*Min*	*Max*	*Mean*	*σ*
SfM-MVS 2013	-	ALS 2013	-19.59	33.61	-0.42	1.72	-9.91	12.04	-0.13	0.78
SfM-MVS 2014	-	ALS 2014	-18.48	22.42	0.03	0.74	-18.17	11.41	0.23	0.65
SfM-MVS 2014	-	SfM-MVS 2013	-33.12	14.19	0.38	1.73	-12.44	12.33	1.58	1.42
ALS 2014	-	ALS 2013	-15.38	10.81	-0.09	0.29	-14.61	7.37	1.30	0.97

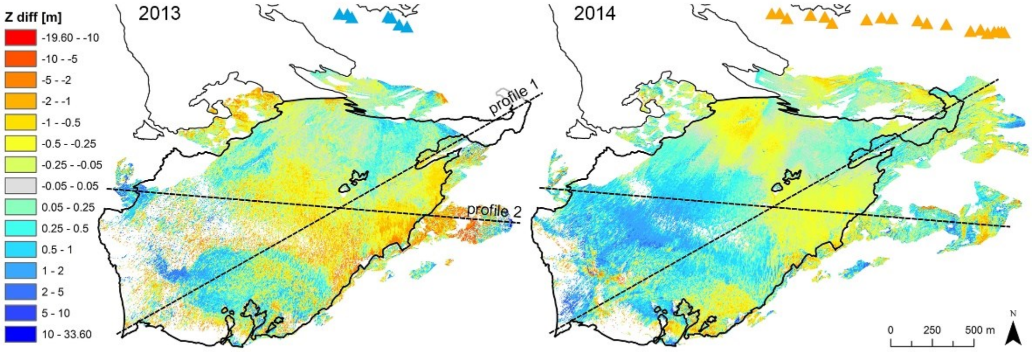

Figure 4.16. Spatial distribution of elevation differences between photogrammetric and ALS-based DTMs on (a) 2013 and (b) 2014.

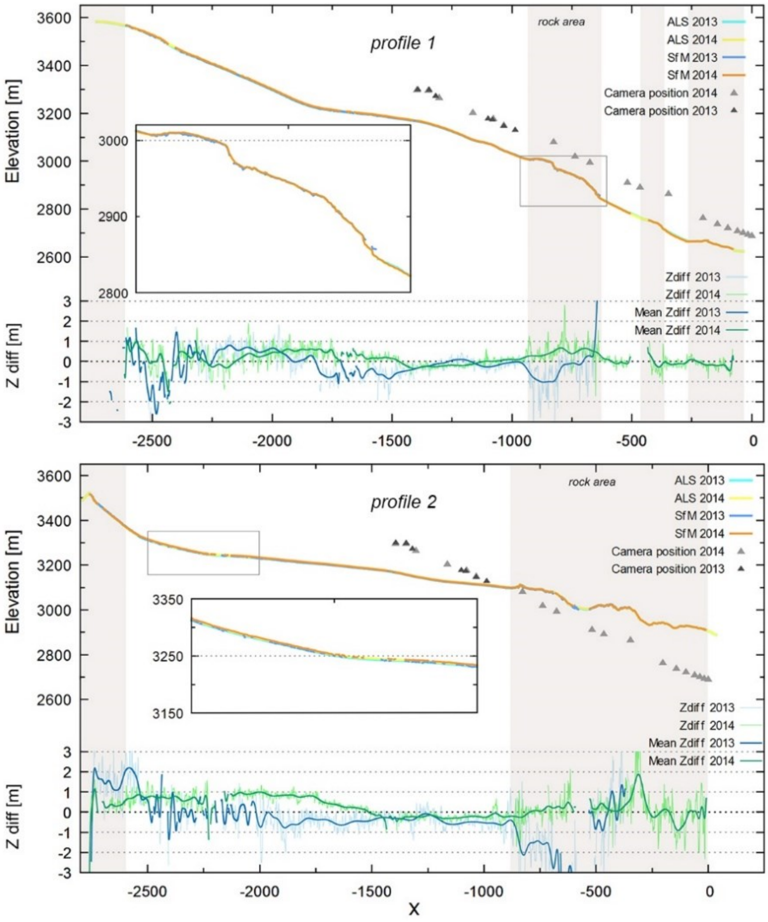

Figure 4.17. Cross sections through the La Mare glacier DTMs show the glacier elevation change and the difference between 2013 and 2014 in SfM-MVS and ALS-based DTMs. The location of the profile 1 and profile 2 is indicated in Figure 4.16. The x-axis zero has been fixed at the first camera position of the 2014 survey and the minimum and maximum values of the z-difference set to ± 3 m.

The effect of terrain slopes on the accuracy of 2014 photogrammetric DTM was quantified for 10 grouped classes of angles (Fig. 4.18). As expected, the standard deviation of elevation differences between the 2014 SfM-MVS and ALS DTMs is proportional to slope but remains lower than 1 m up to 40° on the glacier and up to 60° in the area outside it (Fig. 4.18). A rapid increase in the error is observed for the highest slope classes, which represent a very small part of the investigated area. For the glacier, only 1% of the area has a slope higher than 40°. The mean elevation difference is around zero for most of the low- and middle-slope classes, with the exception of the 0-10° class inside the glacier, where a mean value of 0.41 m (σ = 0.44 m) was calculated. The majority of this slope class lies in a flat area of the glacier at 3200-3300 m a.s.l. and is covered by fresh snow. In addition, this zone has an unfavourable line of sight from the camera positions.

The incidence angle between the line of sight of the camera and the photographed object (vector normal to the surface) is closely related to the slope angle. Five camera locations at different altitude were selected (Fig. 4.19) from where the incidence angles were estimated. Figure 4.19d shows the camera position and the surface covered from each camera view. Frequency distribution histograms for the 5 camera positions reveal that more than 80% of incidence angle range between 70° and 90° (Fig. 4.19a). Linear regression (Fig. 4.19b) shows no statistically significant relationship between incidence angle and elevation difference for the investigated camera positions. Contrary to what is speculated, for the low interval of incidence angle that correspond to high slope angle and consequently good incidence angle, high values of mean and standard deviation were obtained (Fig. 4.19c). For high incidence angles which are flat surfaces with respect to the point of camera view and therefore with few variations in elevation, low and constant values of standard deviation were found. These analyses suggest that, in our case study, the accuracy in z of SfM-MVS DTM is more influenced by slope angle that incidence angle.

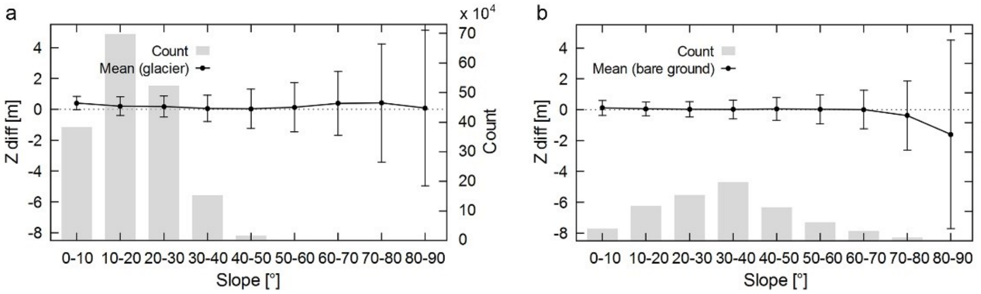

Figure 4.18. Mean and standard deviation of the 2014 DoD between SfM-MVS and ALS-based DTM depending on slope calculated (a) in the glacier area and (b) in the bare ground outside glacier covered by rock. The grey bars show the count of cells at any given slope (y-axis on the right).

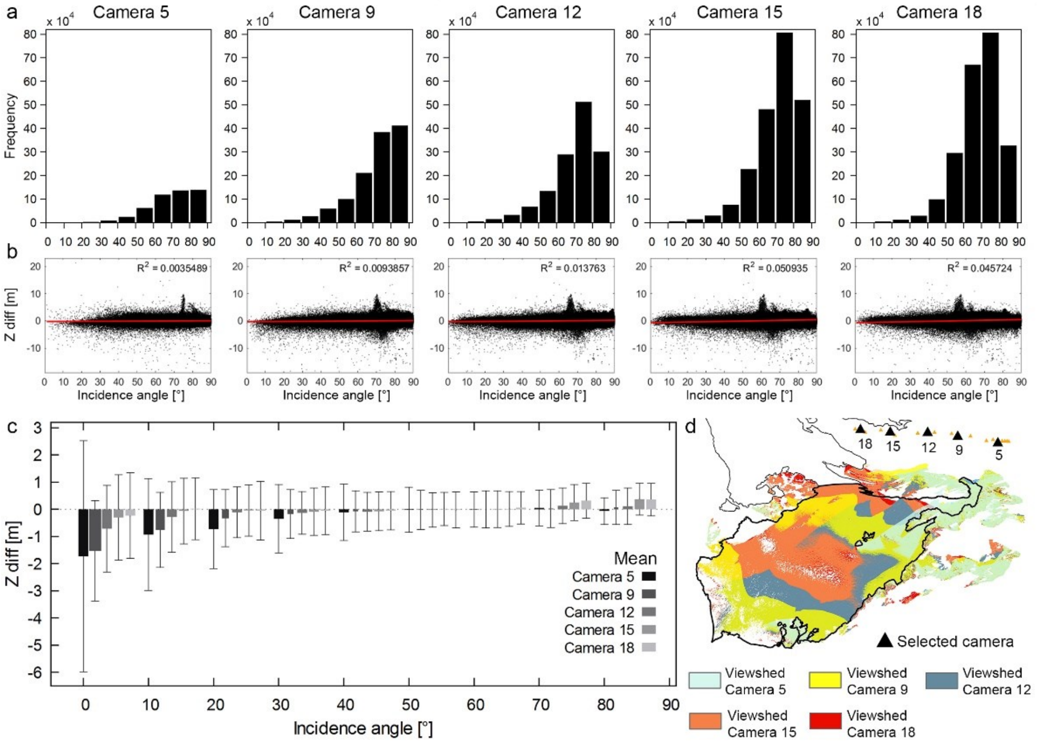

Figure 4.19. Incidence angles between five cameras positions and vectors normal to the surface. (a) Frequency distribution histograms of incidence angles calculated for the corresponding surface and (b) the scatterplot of the elevation difference and incidence angle for the five camera positions; (c) mean of elevation differences with one standard deviation y bars calculated for each camera and for incidence angle intervals; (d) map of the locations of the selected cameras with the viewshed reconstructed area visible from each camera point.

Because the camera-object distance (depth) strongly influences the photogrammetric accuracy (Gómez-Gutiérrez et al., 2014), its effect was evaluated by calculating the mean and standard deviation of the elevation difference between the 2014 SfM-MVS and ALS DTMs, clustering the pixels in 200 m distance classes from a camera position at the centre of the array displayed in Figure 4.15b. The relationship between error and depth is clearer for the glacier area (Fig. 4.20a), whereas in the surrounding area, the error appears to be more influenced by the variability of the slope angle (Fig. 4.20b). The obtained results were compared to the theoretical behaviour of the error as a function of the depth (σ_d), as calculated using the following formulation, already mentioned in Chapter 3 (Eq. 3.3):

$$\sigma_d = m_B \cdot \frac{D}{B} \cdot \sigma_i, \tag{4.3}$$

where m_B represent the image scale (*D/ focal length*); *D* is the depth in y direction (distance camera-object); *B* is the baseline and σ_i is the measured accuracy in image space.

The theoretical σ_d was calculated for each class of distance considering a mean baseline of 400 m and an accuracy in the image space of 0.40 pixel, which is the reprojection error after bundle adjustment computations. Another quantification of the error as a function of the depth was obtained, for comparison purposes, by multiplying the GSD (which increases with depth) by the reprojection error provided by PS for the GCPs. Figure 4.20c shows that, on the glacier, the accuracy calculated from the DoD matches quite well the 'theoretical' calculations up to a depth of 1900 m. Beyond this distance, the detected error increases faster than in theory, likely due to the increasing coverage of fresh snow, which affects the image texture and decreases the accuracy.

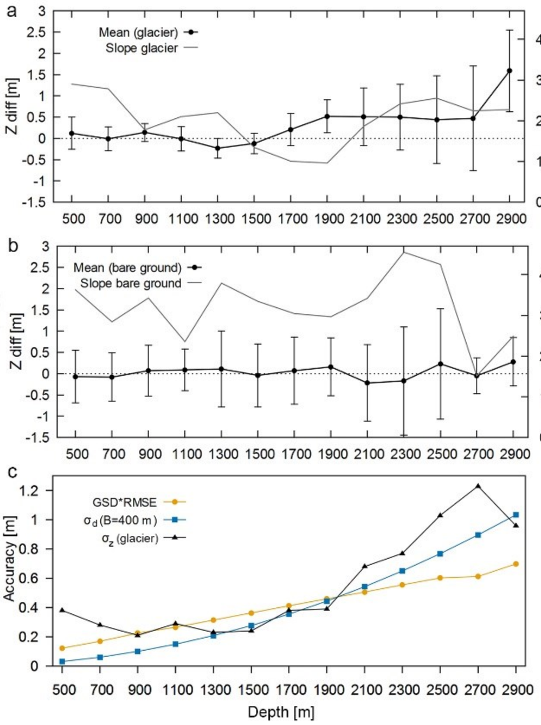

Figure 4.20. Mean and standard deviation of the 2014 DoD between SfM-MVS and ALS-based DTM depending on depth calculated (a) in the glacier area and (b) in the bare ground outside glacier covered by rock. The trend of the average slope angle for depth intervals is shown on the right y-axis. (c) Comparison of σ_z measured in the glacier reconstructed area, the theoretical depth accuracy estimated according to the Eq. (4.3) and the GSD multiplied for the GCPs RMSE for the depth intervals.

Then it was evaluated the accuracy of photogrammetric reconstruction for the different substrata, whose spatial distribution was outlined on the orthophoto exported from PhotoScan. Debris, ice and firn display similar accuracy, with median values of elevation difference between the 2014 SfM-MVS and ALS-based DTMs close to zero and interquartile ranges of the same magnitude. Conversely, the area covered by fresh snow, which is also the area with greater depth, shows prevailing positive differences, a median value of 0.48 m and a much higher standard deviation (σ = 0.82 m). The texture of the surface also influences the point density distribution and the spatial coverage of the reconstructed area. A lower value of the point density was obtained for fresh snow (4 pts m^{-2}). Increasing point densities were obtained for firn, ice and debris (10, 13 and 15 pts m^{-2}, respectively). The spatial coverage in the fresh snow area was 75%, whereas it was 93% in the rest of the glacier. Excluding the areas not visible from the camera position and occlusions imposed by the topography, the spatial coverage in the fresh snow area was 82% and 98% in the remaining part.

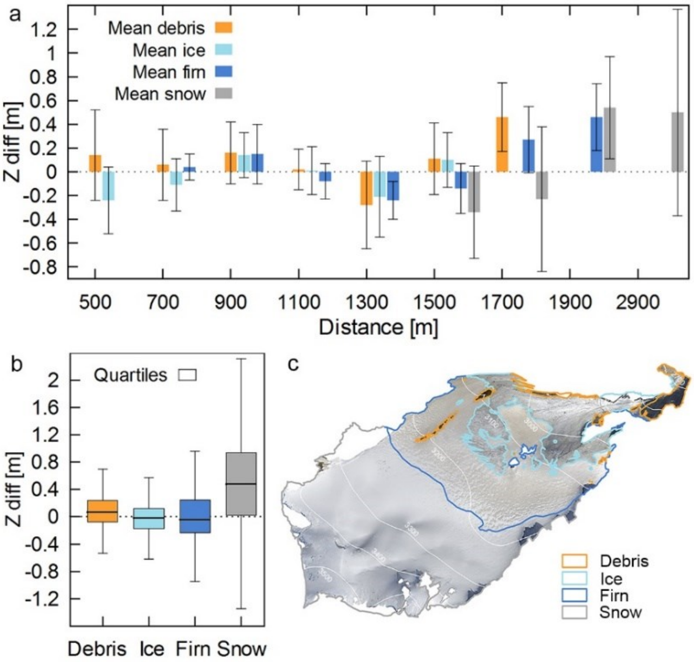

Figure 4.21. Elevation difference between the 2014 SfM-MVS and ALS-based DTMs calculated for different substrata. The figure shows (a) the mean and standard deviation of z-difference for four substrata (debris, ice, firn, and snow) grouped by distance from camera position; (b) the box plot of the z-difference for four substrata. In the box-whisker plot, values which exceed 1.5 * IQR were considered outliers. In figure (c) the orthophoto of the glacier on 27 September 2014 and map of substrata.

The point density is also affected by the depth, elevation and slope (Fig. 4.22). Due to the GSD, the average point density decreases with depth, which in our case is also proportional to the elevation. On the glacier, the point density decreases more rapidly than in the surrounding area for elevations between 3100 and 3300 m a.s.l., due to the poor texture in this snow-covered flat area. Increasing densities with slope, up to 70-80°, are observed and likely result from more favourable incidence angles, which do not however guarantee high accuracy, as noted earlier (Fig. 4.19). Considering the entire reconstructed surface, the point density was higher in the area surrounding the glacier than on it (12 pts m^{-2} vs. 8 pts m^{-2}, respectively).

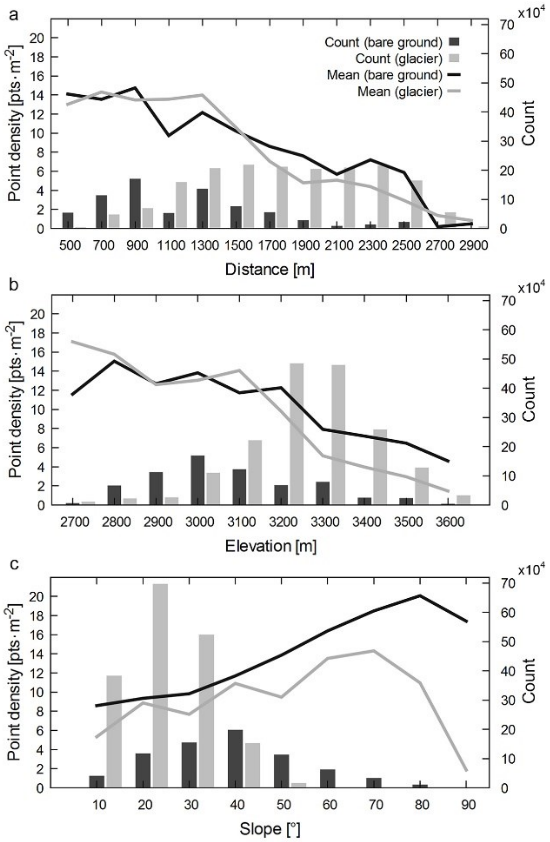

Figure 4.22. Relationships between point density of the 2014 photogrammetric 3D model and (a) camera-object distance, (b) elevation and (c) slope calculated for the glacier and rock stable area outside glacier. The point density was estimated using the filtered and subsampled point cloud.

Mass balance calculation on La Mare Glacier

Due to abundant solid precipitation during the accumulation season and low ablation rates during the summer (the glacier was snow-covered above ~3000-3100 m a.s.l.), the mass balance of the La Mare Glacier was positive in the 2013-14 hydrological year for the first time since the beginning of measurements in 2003. At the end of the ablation season, the Equilibrium Line Altitude (ELA) was at 3012 m a.s.l., and the Accumulation Area Ratio (i.e., the ratio between the accumulation area and the total area, AAR) was 0.86. According to the direct glaciological method, the annual mass balance was +0.83 m w.e. (Carturan, 2015).

The mass balance estimates obtained with the geodetic method based on the SfM-MVS and ALS DTMs acquired in 2013 and 2014 were compared according to the Eq. (4.1) and (4.2). The area of the glacier between the two surveys did not change. The mean density was obtained by a fractional area-weighted mean, assigning

900 kg m^{-3} for the ablation area (Huss, 2013) and 530 kg m^{-3} for the accumulation area, as directly measured in a snowpit. The resulting weighted mean density was 600 kg m^{-3}. In the mass balance calculations, both raw $\overline{\Delta z}$ values and corrected raw $\overline{\Delta z}$ values were used to account for the mean errors in the stable areas outside the glacier (Table 4.9). As shown in Table 4.9, the geodetic mass balance estimates using only ALS data do not differ significantly for either the entire glacier or the sub-areas covered by the photogrammetric surveys of 2013 and 2014 (88% and 93%, respectively). The estimates range between 0.85 and 0.88 m w.e for the raw data and between 0.90 and 0.94 m w.e. for the corrected data. The geodetic mass balance calculations using only photogrammetric data yield a raw value of 1.09 m w.e. and a corrected value of 0.87 m w.e. Using the 2014 SfM-MVS, which has a higher quality than the 2013 ALS DTM, yields a raw value of 0.98 m w.e. and a corrected value of 1.02 m w.e. Area-averaged estimates of the geodetic mass balance from photogrammetric data are very close to the estimates from ALS data and from the direct method and are closer still if the mean DTM error in the stable areas outside the glacier is subtracted from the raw average elevation differences. The spatial distribution and magnitude of elevation change is also well captured by the terrestrial photogrammetry (Fig. 4.23 and Fig. 4.24), even if, as already noted in the previous section, problematic areas are present in the upper part of the glacier, which was covered by fresh snow, especially in the 2013 SfM-MVS survey.

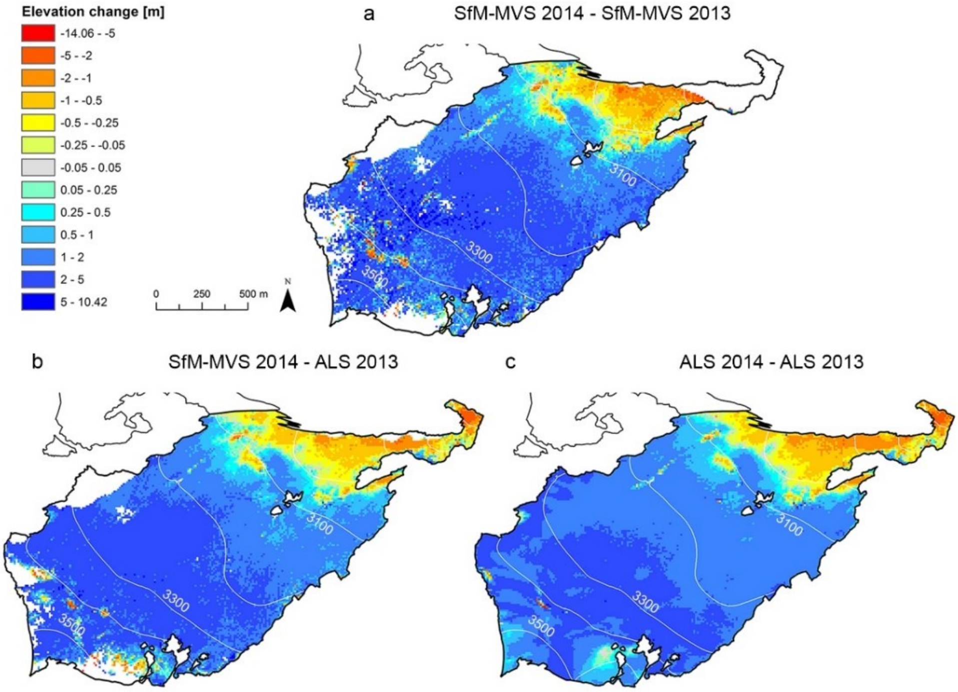

Figure 4.23. Spatial distribution of elevation changes between (a) SfM-MVS 2014 and SfM-MVS 2013 DTMs (b) SfM-MVS 2014 and ALS 2013 over the area of the glacier with common coverage and (c) ALS 2014 and ALS 2013 over the entire glacier.

Table 4.9 Mass balance calculations on La Mare Glaciers using different combinations of SfM-MVS and ALS DTMs.

Mass balance estimation									
DTMs cell size 10 m			Spatial coverage $[m^2]$	Average elevation changes *[m]*		Volume change *$[m^3]$*		Mass balance *[m w.e]*	
				Raw	*Corrected*	*Raw*	*Corrected*	*Raw*	*Corrected*
SfM-MVS 2014	-	SfM-MVS 2013	1,834,800 (~88%)	1.81	1.45	3,320,988	2,660,460	1.09	0.87
ALS 2014	-	ALS 2013		1.47	1.56	2,697,156	2,862,288	0.88	0.94
SfM-MVS 2014	-	ALS 2013	1,938,700 (~93%)	1.64	1.70	3,179,468	3,295,790	0.98	1.02
ALS 2014	-	ALS 2013		1.41	1.50	2,733,567	2,908,050	0.85	0.90
ALS 2014	-	ALS 2013	2,072,700 (entire glacier)	1.43	1.52	2,963,961	3,150,504	0.86	0.91

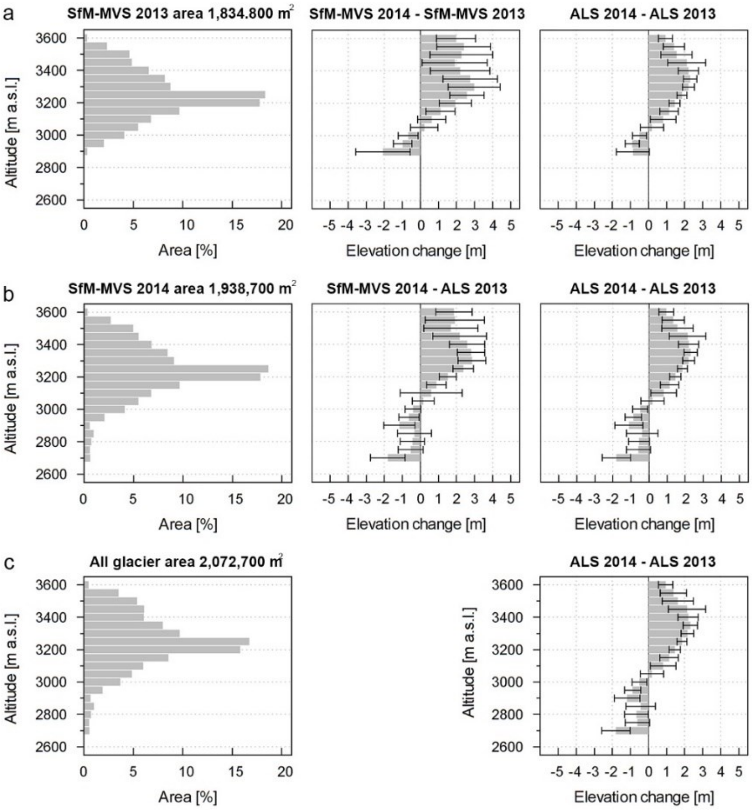

Figure 4.24. Area-altitude distribution and surface elevation change with standard deviation for the glaciological year 2014/2013 displayed for altitudinal bands with 50 m interval. The elevation change were calculated between (a) SfM-MVS DTMs of 2013 and 2014 in the 2013 photogrammetric reconstructed area; (b) SfM-MVS DTMs of 2014 and ALS DTM of 2014 in the 2014 photogrammetric reconstructed area; (c) ALS DTMs of 2013 and 2014 of the entire glacier. The photogrammetric results were compared with the corresponding ALS result calculated in the same area.

4.3.4 Discussion

The terrestrial photogrammetric approach based on SfM-MVS algorithms was tested for reconstructing the glacier DTMs in order to monitoring geometry and volumetric change of the surface. The DTMs accuracy obtained by SfM-MVS point cloud was calculated and analysed as elevation differences from the reference ALS DTMs. In this application the accuracy assessment of SfM-MVS DTMs reveals the presence of systematic errors. As it was demonstrated that inaccurately estimated lens distortion parameters is the cause of systematic error in DTMs (Wackrow and Chandler, 2011) the cameras (with the same settings used during the surveys) were pre-calibrated in the test-field and their estimated parameters were maintained fix during the bundle block adjustments. During the bundle adjustment in addition to interior calibration parameters, the positions and orientations of all images are determined. Consequently, considering the camera calibration correctly estimated the systematics effect should be identified in the external camera orientation that depends on the accuracy of the automatic image feature extraction and feature matching and in the scale definition of the photogrammetric model. The latter is defined in this work via the manual identification of natural GCPs in the reference ALS DTM and then in the images.

The GCPs positions were included in the bundle adjustment process to reduce the distortion of the model shape (James and Robson, 2014). However, the GCPs should be distributed widely across target area, not the margins (Bemis et al., 2014), but the changes over the time of the glacier restricted the GCPs location outside of interested area. The low accuracy GCPs identification, quantified by the RMSE (Table 4.7), can be cause of scaling and referencing errors between the compared DTMs. The scaling error or shift between the photogrammetric and LiDAR point cloud is demonstrated by a strong influence of DTM z-error with slope inclination. In steep and complex alpine terrain error in the x and y direction implicate large errors in the z direction (Fisher and Tate, 2006).

The quality assessment of DTMs derived by SfM-MVS showed that the photogrammetric accuracy decreases significantly in terrain steeper than 50°. Highest values of slope and z-errors are identified outside the investigated objects characterized by bedrock terrain. That areas appeared during the surveys and consequently in the images with strong contrasts, deep shadow with different length due to change in the sun`s azimuth and the topography, and high feature variability between the images due to changes in illumination.

The source of errors in that areas has to be identify in the quality of the image texture that reduce the ability of automated feature matching to identify unique corresponding features in overlapping images (Bemis et al., 2014, Müller et al., 2014). Variable images texture is mainly due to the duration of the survey about four hours for the glacier survey needed to reach the upper part of ridge opposite to the glacier. However, lower accuracy of photogrammetric DTM of the glacier was identified in the snow coverage area characterized by poor image texture, with little texture variation (also after the editing of photos exposure) and surface reflection.

The poor features present in the snow covered area affected also the point density with a strong reduction of points in this substratum. This area was also the most subjected to filtering of noise and identifying a good compromise between spatial coverage and noise reduction was a big challenge. Priority was given to the spatial coverage. A decrease of point density was also obtained with the increase of distance from the camera positions. The characteristics of the adopted terrestrial photogrammetric survey affected the density of points and the accuracy of points.

In the range of the main factors that influence the image measurements precision and the related object point precision, the role of incidence angle was not so relevant. Contrary to held assumptions, high values of incidence angle from the ground photos acquisition (that should be an issue in the photo-based reconstruction) highlighted lower error variations that can be justified by a constant z for flat areas.

A crucial aspect was the high camera-object distance (up to 2900 m) imposed by the ground survey. According to the statement of Gómez-Gutiérrez et al., (2014), distances from the camera to the target closer than 1 km are recommended for accuracy smaller than 1m. However, in remote area it is not always feasible to establish the acquisition distances according to desired precision. In this application, the baseline and the number of overlapping images were increased by acquiring the images in panorama mode, in order to reduce the negative effect of high distances having few acquisition points and the risk of data gaps. This image acquisition approach allowed us to reconstruct the entire glacier visible from the camera views with accuracy around 1 m up to the 1900 m from the camera. Better results in terms of noise, spatial coverage and elevation difference with the reference ALS data were obtained in 2014 measurements. The better quality of the 2014 survey has to be attributed by i) the higher numbers of camera locations viewing the same point that ensured an increasing of the baseline and relative intersection angles between the cameras, and ii) the higher numbers of images for each panorama, due to the larger focal length, that is recommended to obtain reliable models (Favalli et al., 2012; Bemis et al., 2014; Hosseininaveh et al., 2014). However, although for longer distances better depth accuracy than the theoretical estimation was achieved. The reconstructed glacier tongue, closer to the camera positions, produced lower precisions (around 30 cm) than the expected results in terms of depth accuracy. In fact, the tongue of the glacier due to its low altitude is visible from a limited number of camera positions with high intersection angle and it is subject to the shadows of the surrounding bedrock area.

Additionally, the panoramic acquisition for the target objects that lie both in background and foreground was not an optimal solution for the SfM-MVS approach that can generate misalignments of the frames that compose the panoramas, especially when poor features extraction and features matching occur as well.

Compared to airborne laser scanning the terrestrial photogrammetry method in the tested area has been shown to be less accurate. However, the DTMs obtained from the images showed a good qualitative and quantitative correspondence with ALS-based DTMs for monitoring glacial processes with sufficient accuracy. On the La Mare Glacier, the area-averaged estimates of the 2013-14 geodetic mass balance from ALS and photogrammetric data were almost identical (0.91 and 0.87 m w.e., respectively) and close to the mass balance calculated from the direct glaciological method (0.83 m w.e.). The differences are well within the uncertainty of the direct mass balance estimates, which has been quantified as approximately ±0.2 m w.e. y-1 by previous studies (Cogley and Adams, 1998; Cogley, 2009).

The tested photo-based 3D reconstruction technique can fill the gaps of range-based technique by providing more frequent surveys with high level of detail and high expertise for data collection are not required. For improving the photogrammetric accuracy at long scale, aerial platform in combination with oblique images acquired from the ground that are more adequate for steep terrain could represent a solution. However, the feasibility of UAVs in glacier environments has to be further investigated (Immerzeel et al., 2014), because the wide extension of the surface and extremely windy conditions reduce the applicability of these platforms in alpine environments. For the glacier area aerial platform such as helium balloon may be more suitable but less manoeuvrable (Smith et al., 2015). The panoramic mode acquisitions have shown their effectiveness to reconstruct the glacier area. However, further research remain open in order to optimize the images acquisition (camera filter, HDR images), the panorama images orientation and the filtering of noise of the dense point cloud.

4.4 ROCK GLACIER CASE STUDY

The aim of this application is test the potential and limits of terrestrial SfM-photogrammetry for monitoring the rock glacier dynamics, and in particular for annual surface changes estimation. The approach was adopted to detect the surface displacement of a 0.06-km^2 rock glacier located in Eastern Italian Alps. The active rock glaciers are a creep phenomena and due to the physical properties of ice the annual flow velocities are in the range of centimetre to meters. Therefore, the LiDAR technology is an efficient tool to perform these measurements in accurate way. However, the ALS lacks in resolution for a reliable investigation of the phenomena in short temporal scale. Contrary, the TLS has high potential in term of density of point and accuracy but lacks in the achievable spatial coverage and the low portability of the instrumentation reduces the practical application on remote areas. Compared to other available survey techniques, the photogrammetry with a reasonable cost in time and money, the applicability at wide scale at very high resolution and potentially with high accuracy and precision appears an interesting solution for measuring homogeneous surface displacement such as those generally affecting rock glaciers. However, the application of the technology for this purpose is limited at few cases. Therefore, this case study represents a practical application that highlights the practical issues of a ground photogrammetric survey in complex terrain like rock glacier.

4.4.1 Study area

Figure 4.25. Geographic setting of the study area. View of the AVDM3 Rock glacier surveyed on 27 September 2014.

The AVDM3 Rock Glacier is located in the south-eastern part of the Ortles-Cevedale massif (Eastern Italian Alps), close to the La Mare glacier. The AVDM3 Rock Glacier (Carturan et al., 2015) is an intact, tongue-shaped rock glacier characterized by the presence of two lobes. The 0.058 km^2-wide Rock Glacier (maximum length of 390 m; maximum width of 240 m) faces south-east and is located at elevations of between 2943 and 3085 m a.s.l. The average slope of the Rock Glacier is 26°, and the slope of the advancing front is 36°. The activity status of the AVDM3 Rock Glacier was assessed via repeat geomorphological field surveys between 2007 and 2014. These surveys revealed the advance of the front of the southern lobe (Carturan, 2010). The general morphology and the elevation of the front also suggest that this rock glacier is active (Seppi et al., 2012), and its permafrost content is further corroborated by spring temperature measurements (Carturan et al., 2015). Moreover, Bertone (2014) provided the first quantification of the surface displacement rates of this rock glacier for 2003 to 2013 using ALS data.

4.4.2 Methods

In this section, the photogrammetric survey of the AVDM3 Rock glacier and the image processing to produce the dense point cloud are described. ALS data were used to select the GCPs required to scale and georeferencing the SfM-MVS 3D model and to validate the photogrammetric result and estimate the surface displacements of the rock glacier.

ALS Data acquisition and data processing

The AVDM3 Rock Glacier was surveyed by airborne laser scanning on 17 September 2003, 22 September 2013, and 24 September 2014. The ALS data of 2013 and 2014 were already mentioned and described in the previous Paragraph (Table 4.6, Section 4.3.2). The LiDAR processing was the same adopted for the previous case study. Therefore, the 2003 and 2014 ALS point clouds were iteratively fitted to the 2013 point cloud by applying an affine transformation. The LiDAR point cloud acquired in 2013 was treated as a reference only for stable areas outside rock glaciers, and therefore snow patches and geomorphologically active areas (e.g., landslides, river beds, and debris flows) were removed before the registration. The 2003 and 2014 LiDAR point clouds were iteratively fitted to the reference point cloud by applying an affine transformation. The ICP registration of the point clouds produced z-direction residual values of 0.11 m for the 2003 LiDAR point clouds. This accuracy can be assumed to be sufficient for calculating the decadal displacement rate on the rock glacier. The co-registered point clouds were then converted to DTMs, using the Natural Neighbours. Based on the low resolution obtained from the ALS acquisition of 2003 (i.e. point density of 0.5 pts m^2) the DTMs were generated with a pixel size of 0.5 x 0.5 m.

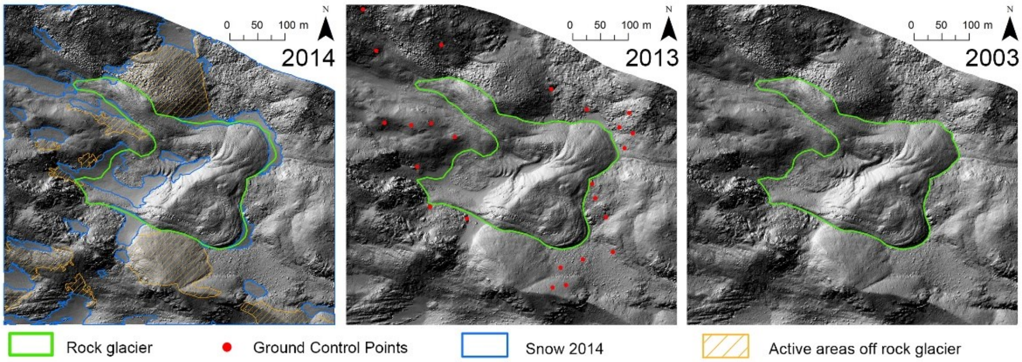

Figure 4.26. ALS shade DTMs of AVDM3 Rock glacier acquired on September 24, 2014, September 21, 2013 and 17 September 2003. The red dots represent the selected GCPs in 2013 DTM used in the photogrammetric approach.

Photogrammetric data acquisition and data processing

Data acquisition and data processing

Table 4.10. Data acquisition settings and processing results of the photogrammetric surveys for both case studies.

SfM-MVS data processing	
	27 September 2014
Input data	
Camera type	Canon 5D Mark III
Focal Length	28 mm
Image size	5760x3840 pix
N° Images	198
Processing data	
Reprojection error	0.38pix (1.20 max)
GCPs error	0.62m 1.86pix
Image quality	High
Mean GSD	0.064 m/pix
Dense point cloud	56,171,705 pts
Point density	244 pts m^{-2}
Post-processing data	
Filtered point cloud and subsampled	4,517,143 pts (sampled 0.10 m)
Point density	21 pts m^{-2}
ICP transformation	0.10 m

The terrestrial photogrammetric survey of the AVDM3 Rock Glacier was performed on 27 September 2014. In this survey, 198 images were acquired freehand while walking around and on top of the rock glacier. However, due to accessibility and safety issues it was impossible to acquire the images in order to cover the entire surface. The survey camera was a CANON EOS 5D full frame SLR camera equipped with a fixed-focal lens of 28 mm. The photo-based reconstruction workflow is summarized in Figure A.3, Appendix A. The same setting adopted for the processing of the La Mare

Glacier data (See Section 4.3.2) was adopted to process this dataset. This means that the camera was recalibrated and the constraints of GCPs and camera calibration parameter (maintained fix during the bundle adjustment optimization) was included during the camera orientation. GCPs were selected as natural features in rock stable area and the coordinates have been extracted from ALS DTM 2013. After several tests to optimize the GCPs distributions (see Appendix A, Fig. A.4), 24 control points were selected in stable area. The generated dense point cloud with 'high' quality (half image resolution) produced a very dense point cloud. After the noise filtering, the SfM-MVS point cloud was subsampled to 10 cm before to generate the DTM in order to obtain a comparable number of point with the ALS data. The SfM-MVS processing results are showed in Table 4.10.

4.4.3 Results

The vertical accuracy of Rock Glacier DTM derived from the SfM-MVS point cloud was estimated as z-difference with the ALS 2014 DTM. The effect of the slope, the surface texture and the shadows were evaluated in terms of DTM accuracy and spatial resolution. DTMs surveyed by ALS in September 2003 and September 2013 were used to estimate the decennial surface displacement of the rock glacier by DTMs differencing. The dataset of 2104 of both ALS and photogrammetry were used to evaluate the annual surface change comparing the results with those obtained by decennial estimation and with the 2013 DTM differencing. The horizontal movements of the rock glacier were estimated by manual feature tracking of features identified in the shaded DTMs.

Accuracy assessment of the SFM-MVS DTMs

The holes interpolation and the different snow accumulation areas were masked during the DTMs comparison for the accuracy evaluation. The 2014 terrestrial photogrammetric survey of the AVDM3 Rock Glacier provided a good spatial coverage (83%) of high-resolution terrain data (Fig. 4.27). A visual analysis of the SfM-MVS DTM reveals the presence of grainy effect in the direction of photo acquisition and pixel-noise which is not present in the DTM produced with ALS methods (Fig. 4.27a). The spatial distribution of the elevation difference between the contemporaneous SfM-MVS and ALS DTMs shows the existence of areas with both positive and negative values (Fig. 4.28). The average elevation difference is 0.02 m on the rock glacier (σ = 0.17) and 0.05 in the surrounding areas (σ = 0.31 m, Tab. 4.11). Due to the articulate morphology of the rock glacier surface the accuracy of the photogrammetric DTM was evaluated according to the slope angles that were calculated from the ALS 2014. Similar to the La Mare Glacier area, the accuracy decreases with increasing slope in the rock glacier area. The standard deviation of the average elevation difference between the SfM-MVS and ALS DTMs is less than 0.20 m up to 40° (Fig. 4.29). However, in the area surrounding the rock glacier, the error increases faster with slope because steep areas coincide with shaded areas and high solar zenith angles, because the images were acquired in the afternoon. As suggested by Gómez-Gutiérrez et al. (2014) the relationship between the quality of the photogrammetric DTM and the amount of shadowed-lighted areas in the photographs was calculated. For this purpose, a hillshaded model (Fig. A.5, Appendix A) was calculated by simulating the position of the sun in the sky (the azimuth angle and the zenith angle) during the photogrammetric survey. The statistics of elevation difference with ALS DTM were calculated for ten groups of hillshaded value. As shown in Figure 4.30, larger errors occur in shadowed areas and smaller errors in well-lit areas, even if the largest differences in accuracy can be observed outside rather than on the rock glacier.

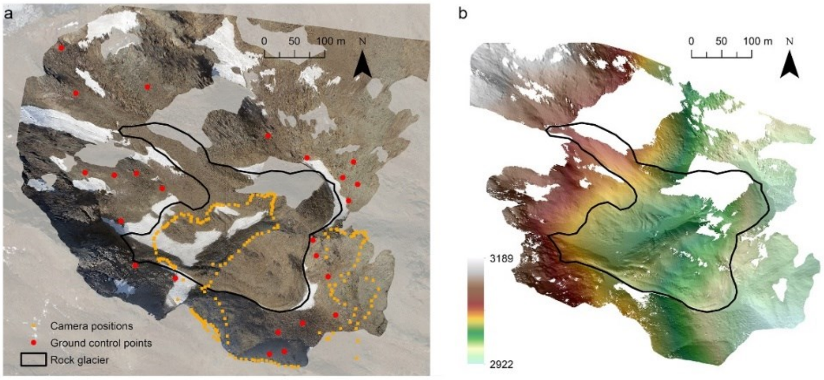

Figure 4.27. Correspondence between (a) the orthophoto of SfM-MVS 3D model of rock glacier surveyed on 27 September 2014 and (b) the hillshaded model of rock glacier model calculated at the same data and hour of the images acquisition. The holes in the DTM represent not reconstructed area.

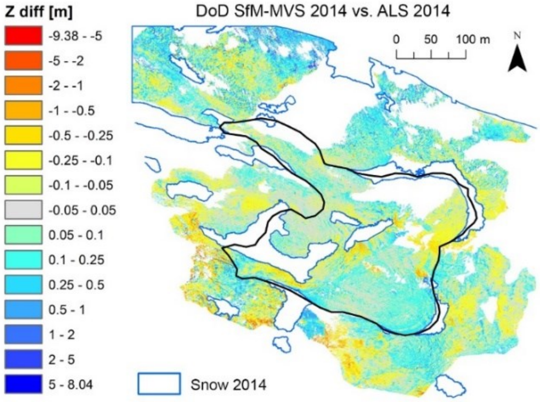

Figure 4.28. Spatial distribution of elevation differences between photogrammetric and ALS-based DTM acquired on 27 September 2014 and 24 September 2014, respectively. The blue shape is the snow accumulation areas excluded during the DTMs comparison.

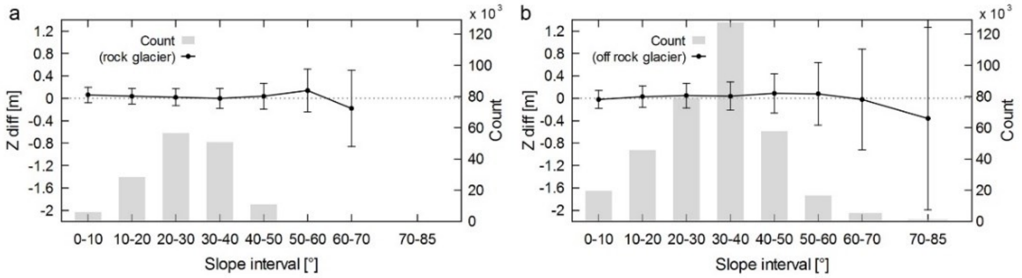

Figure 4.29. Elevation differences between 2014 SfM-MVS and ALS-based DTMs calculated for the slope interval (a) in the rock glacier reconstructed area and (b) in the bare ground outside the rock glacier.

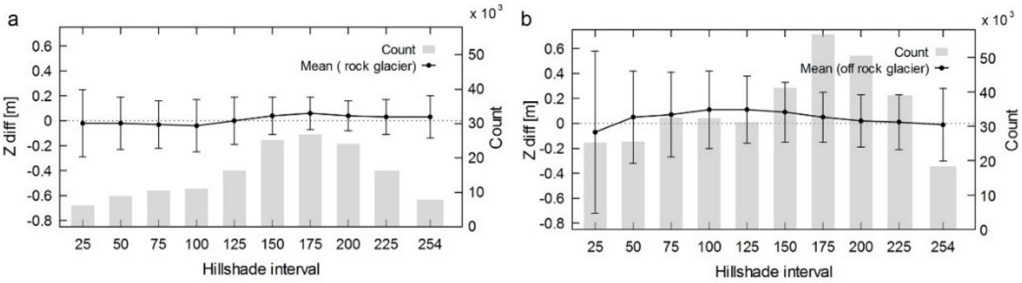

Figure 4.30. Elevation differences between 2014 SfM-MVS and ALS-based DTMs calculated for the hillshaded interval (a) in the rock glacier reconstructed area and (b) in the bare ground outside the rock glacier. Lowest values represent shadowed area whilst lighted areas present the highest values.

Table 4.11. Statistics of elevation changes in the rock glacier and in bed ground stable are off rock glacier from September 2014 to September 2013 and September 2003 in the ALS reconstructed area and in the common ALS and SfM-MVS coverage area.

			Elevation changes [m]							
Data			**ALS Reconstructed area**				**SfM-MVS Reconstructed area**			
			Stable area		Rock glacier		Stable area		Rock glacier	
			Mean	*σ*	*Mean*	*σ*	*Mean*	*σ*	*Mean*	*σ*
SfM-MVS 2014	-	ALS 2014	—	—	—	—	0.05	0.31	0.02	0.17
SfM-MVS 2014	-	ALS 2013	—	—	—	—	0.01	0.33	-0.04	0.18
ALS 2014	-	ALS 2013	-0.05	0.19	-0.07	0.12	-0.05	0.20	-0.07	0.12
SfM-MVS 2014	-	ALS 2003	—	—	—	—	0.06	0.33	-0.16	0.49
ALS 2014	-	ALS 2003	-0.01	0.22	-0.18	0.46	-0.00	0.21	-0.18	0.47
ALS 2013	-	ALS 2003	0.04	0.21	-0.11	0.41	—	—	—	—

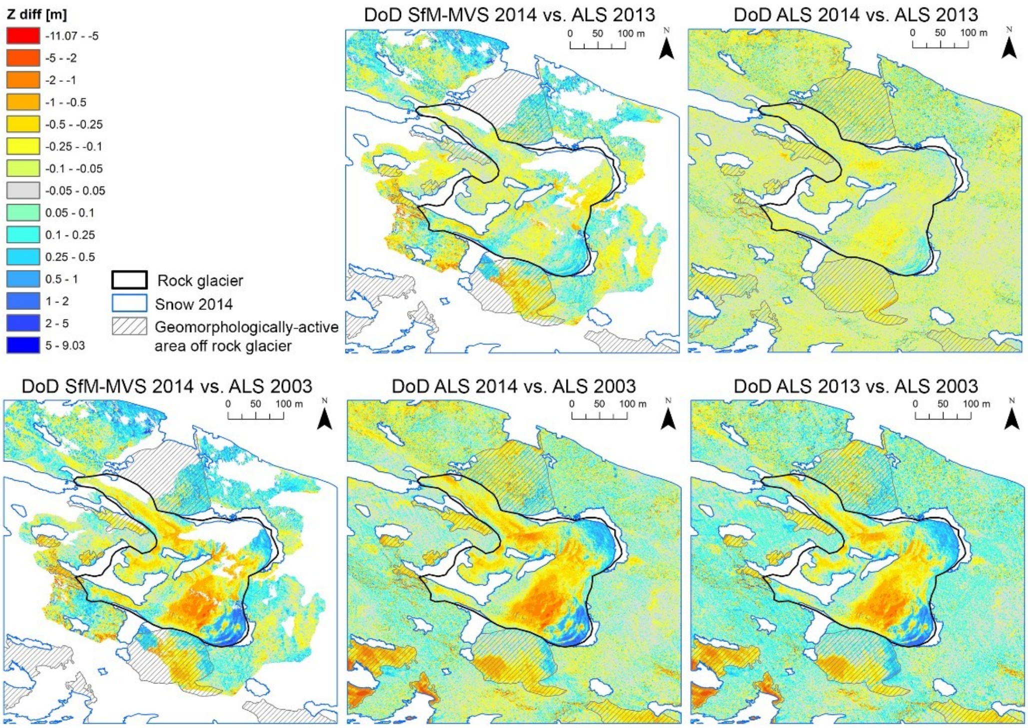

Figure 4.31. Spatial distribution of elevation changes from September 2014 to September 2013 and September 2003 between the DTMs derived from SfM-MVS and ALS.

Surface changes and velocities of the AVDM3 Rock Glacier

The spatial distribution and the mean value of elevation change on the surface of the AVDM3 Rock Glacier were calculated by differencing the available SfM-MVS and ALS DTMs. Table 4.11 shows that, according to the ALS data, there was a prevailing lowering of the surface in the period from 2003 to 2014. Taking into account the average residual bias in the stable area outside the rock glacier, the average lowering rates of the rock glacier surface were 1.5 cm y-1 in the period from 2003 to 2013, and 2 cm in the year 2013-14. Comparing the SfM-MVS DTM of 2014 with the ALS DTMs of 2013 and 2003 and accounting for the mean bias outside the rock glacier, slightly higher lowering rates of 2.2 cm y-1 from 2003 to 2013 and 5 cm from 2013 to 2014 were obtained. As expected on the basis of the accuracy assessment, the decadal lowering rates calculated from the SfM-MVS DTM are in closer agreement with those calculated from ALS data than the single-year calculations. The same can be observed for the spatial distribution of the elevation changes (Fig. 4.31), which shows a prevailing thinning in the upper and middle part of the rock glacier and a thickening of the two advancing lobes. Based on these results, the elevations changes statistics of the rock glacier are not representative for the entire landform due to the active ongoing frontal processes as visible in the map of vertical surface elevation change

(Fig. 4.31). To reveal information about displacement directions and rates of mass movements, the horizontal displacement rate over 11 years (2003 to 2014) was estimated based on both photogrammetric and ALS data of 2014.

Visually based technique has been used by selecting surface features in the shaded DTMs, manually finding their location (pixel) on the two DTMs and measuring their displacements. Shaded relief visualisations were obtained by illuminating DTMs from northwest at a fixed angle of 45°. In Figure 4.32 the vector field between 2003 and 2014 plotted on the 2014 shade DTMs generated by photogrammetry and ALS indicate the computed direction of the movements and the relative displacements.

The lowest number of the features identified on the photogrammetric DTM (97 points vs. 153 points) is related to the partial coverage of the investigated area. The Figure clearly indicates the high dynamics of the two frontal lobes of the rock glacier and slow motions of the northwest active area. Figure 4.31 shows that the fastest moving areas are the two frontal lobes, which also featured the greatest elevation changes. The displacements and velocity statistics obtained with both methods were evaluated in three distinct areas (each with homogeneous displacement) considering the spatial coverage of the photogrammetric DTM and the different topography (aspect and slope).

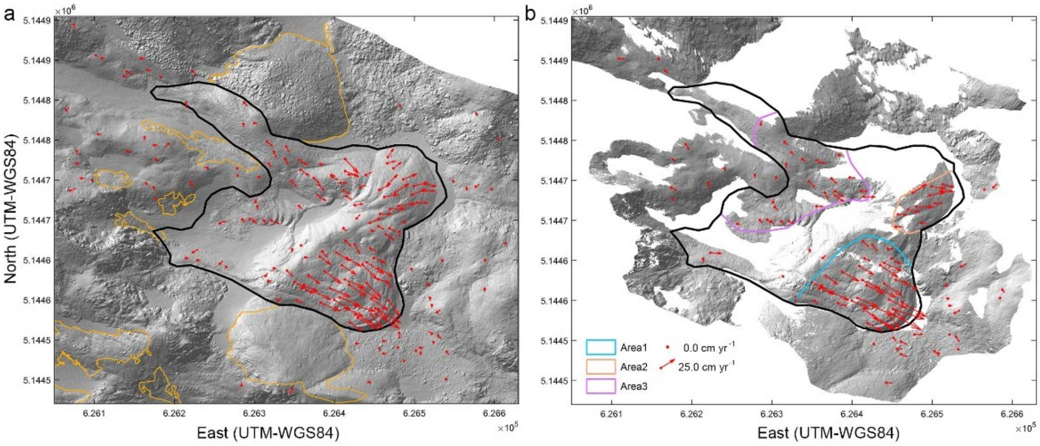

Figure 4.32. Displacement vectors of the rock glacier between 2003 and 2014 computed by a manual identification of natural features visible in the shaded DTMs generated by (a) ALS for both survey epochs and by (b) ALS and photogrammetry for 2003 and 2014 survey, respectively.

Table 4.12. Velocity statistics in three distinct areas of the rock glacier and in stable area outside the rock glacier evaluated comparing the 2003 and 2014 ALS DTMs and the photogrammetric DTM for the 2014 survey epoch.

	Horizontal movements between 2003 and 2014 [cm yr $^{-1}$]									
	ALS 2003 - ALS 2014					**ALS 2003 - SfM-MVS 2014**				
	Nb. points	*Min*	*Max*	*Mean*	*σ*	*N points*	*Min*	*Max*	*Mean*	*σ*
Area 1	41	7.3	43.3	26.8	8.9	36	6.8	47.5	26.3	10.3
Area 2	13	4.4	27.4	18.9	7.0	11	9.0	27.9	18.1	6.4
Area 3	26	4.5	16.5	9.4	4.0	24	4.5	18.2	9.0	4.1
Off rock glacier	65	0.0	10.7	3.6	3.1	23	0.0	13.6	5.3	4.2

The maximum velocity was recorded in the meridional lobe of the rock glacier (see Area 1, Fig. 4.32b) with value of 43 cm yr $^{-1}$ and 47 cm yr $^{-1}$ for the ALS and SfM-MVS DTM, respectively. Table 4.12 shows that the SfM-MVS and ALS data produced very similar surface velocities for the three sub-areas. Outside the rock glacier, the photogrammetric method exhibited a slightly lower accuracy compared to the ALS, but no systematic shift of the different DTMs was found.

4.4.4 Discussion

The results of the terrestrial photogrammetry application on the AVDM3 Rock glacier has shown the reliability of the method to quantify the investigated periglacial processes. The analysis of surface dynamics of the rock glacier based on vertical surface elevation changes reveal the presence of areas affected by subsidence or uplift both inside and outside the rock glacier. Because the AVDM3 Rock Glacier exhibited quite slow annual deformation and creep, reliable results of the displacement rates and area-averaged surface elevation changes can be derived from multi-year (decadal in this case study) time scale. This result confirms the findings of Gómez-Gutiérrez et al. (2014a), who applied a similar method to the Corral del Veleta Rock Glacier in the Sierra Nevada (Spain). The presence of areas with deep shadows and changes in the light during the survey (13:30 and 15:30 pm) reduced the accuracy of the photogrammetric 3D model in these areas. Bemis et al., 2014 demonstrated that model quality degrades significantly for durations > 30 minutes. During the rock glacier survey, additional negative effect on the images quality was determined by the acquisition of some images against the light that could not be removed from the dataset to ensure the orientation of adjacent images. The achieved spatial coverage was not complete due to the limited accessibility and the rock glacier's complex morphology like the presence of ridges, furrows and counter slopes.

The accuracy assessments confirm that the ALS data still provide results with somewhat higher accuracies (Tab. 4.11 and Fig. 4.34) but with much higher costs and demanding logistics than the SfM-MVS approach and lower resolution. The SfM-MVS method has the potential to provide a significantly higher spatial resolution and temporal resolution due to its significantly lower costs, and these characteristics must to be used to investigate the dynamics of complex terrain like rock glacier. In fact, the success of displacement measurements based on visual feature identification or automatic feature extraction (e.g. using images correlation tool) from multitemporal shaded DTMs varies spatially depending on the pixel size of DTMs. And the high point density of the photogrammetric point cloud would enable a detailed investigation of velocity vector compared to the coarse ALS DTM resolution. Moreover, the photogrammetric reconstructions still have room for improvement, by increasing the number of overlapping images and improving the camera network geometry, and try to avoid high sun`s azimuth during the acquisition. For future surveys of the rock glacier, shorter baselines are recommended to ensure greater spatial coverage, high image similarity and good matching performance. GCPs, for example, could be placed on the surface of the rock glaciers to reduce the model distortions (Bemis et al., 2014) and generate surveys with much higher accuracies via, for example, the use of dGPS (Dall'Asta et al., 2015a). In this area, more accessible than the glacier, the acquisition by a differential global positioning system of target or some natural points located inside the study area and visible in the images is feasible and therefore recommended if annual estimation of small-scale terrain movements is required. A solution for the missing areas caused by inaccessibility can to be reached using aerial platform in combination with oblique images.

5

CONCLUSIONS

High resolution three dimensional (3D) models produced from photographs acquired with consumer cameras are becoming increasingly common in the fields of geosciences. However, the biggest disadvantage of an image-based reconstruction is that the quality of the resulting 3D model depends on many factors associated to an individual survey. These factors are principally related to the configuration of the camera network and the ground control points (GCPs) distribution used for georeferencing. Network geometry comprises the number of photos, the percentage of overlap and how convergent the views are, and the intersection angle. The greatest problem to overcome is the distortion or systematic errors of the 3D model caused by parallel image configurations and limited image overlap, and by inhomogeneous distributions of GCPs over the target area.

From a practical point of view, a proper planning (of both photos and control data) of the photogrammetric survey especially for ground-based acquisition is a non-trivial aspect. Especially on complex natural landscapes and alpine environment, the optimal camera positioning in terms of number and locations of overlapping images relative to the object of interest is the major challenge due to the limited accessibility of the target object and the presence of occlusion such as vegetation cover or the presence of rock masses.

These practical issues were addressed in this work by testing the ground-based Structure from Motion and Multi View Stereo (SfM-MVS) approach for reconstructing the 3D surface of four different case studies. In particular the main contribution of this research was to test the potential and the limitation of the ground photogrammetric approach for glacial and periglacial analysis.

To deal the problem of camera network design, a different image acquisition strategy was proposed in this work and tested in a test-field and in a real application. The proposed strategy based on the acquisition of a sequence of images in panorama mode has improved the accuracy of the SfM results in comparison with those obtained from a single image acquisition. The increased number of overlapping and convergent images reduced the distortions of the 3D model where GCPs are not located and where a lower number of intersection rays is available. Furthermore, the proposed method increased the number of viewpoints reducing the risk of data gaps caused by the presence of occlusions such as vegetation cover.

Regarding the geo-referencing, the investigations in this project highlighted a significant influence on the 3D model accuracy of the distribution of ground control points used for georeferencing. In particular it was demonstrated in a test area that a weak GCP distribution generated model distortions, providing good accuracy only within the area covered by the GCPs. Increasing the number of GCPs did not improve the photogrammetric results. Furthermore, as demonstrated in the practical applications, the final SfM-photogrammetry accuracy is more affected by the GCP distribution than their accuracy, for example by using some natural features employed as GCPs whose coordinates were manually extracted from the LiDAR point cloud or digital elevation model (DEM). When the accuracy demands on change determination are not too strict, and a proper placing of GCPs is not ensured, direct measurement of camera positions using GPS is more convenient than usage of GCPs. Although, the ICP registration with a reference surface should be applied to solve the transformation error introduced by the directing measurements.

In this study, a photogrammetric processing method based on SfM-MVS algorithms was employed to create a portable, low cost, semi-automated approach to produce accurate 3D reconstructions of the Montasio Occidentale glacier, La Mare glacier and the neighbouring AVDM3 Rock glacier from a sequence of overlapping terrestrial images acquired with a common digital camera.

The primary goal of these applications was to obtain the optimum balance between the time and the risks associated with image capturing and the need to maximize the quality of the generated DEMs. Despite the limitations of the adopted expeditious method, which include i) the location of GCPs on natural targets outside the investigated glacier/rock glacier, ii) the presence of areas with deep shadows and changes in the light during the survey, iii) the presence of fresh snow in the upper and middle part of the glacier (La Mare Glacier), and iv) the high camera-object distance to avoid the access to the glacier (La Mare Glacier), the results are promising. Different accuracies and resolutions were obtained for the three reconstructed photogrammetric DTMs according to different ground survey characteristics. Among the various aspects analysed, the impact of factors that affected the quality of the 3D reconstructions like the surface texture, the type of substrata (snow, firn, and debris), slope and incidence angle was less decisive than issues related to the camera network geometry and GCPs distribution.

The terrestrial photogrammetry applications in the investigated case studies demonstrated that it is possible to reliably quantify the glacial and periglacial processes by means of a quick and safe survey that was conducted on a single day using cheap, light and easy-to-use hardware. Several steps required a certain degree of subjectivity, e.g., the identification of the GCPs. However, due to the high automatism of the image processing, the level of expertise is considerably lower than for LiDAR and traditional photogrammetry.

The accuracy assessments of the photogrammetric DEMs based on elevation differences with LiDAR data confirmed that the range-based technique still provide results with somewhat higher accuracies but with much higher costs and demanding logistics than the SfM-MVS approach. However, the SfM-MVS method has the potential to provide a significantly higher spatial resolution that should be used to investigate the dynamics of complex terrain like rock glacier. Additionally, even where LiDAR (both from terrestrial or aerial) derive topographic data already exist, photo-based 3D reconstruction technique can add to the temporal dimension of the topographic data by enabling more frequent surveys when repeat ALS or TLS survey would be cost prohibitive or logistically difficult.

The combination of SfM-photogrammetry and unmanned aerial vehicles could solve the problem of excessive camera-object distances and the issue of missing areas due to inaccessibility.

Based on the investigated studies and a consequent full understanding of the main issues and error sources of a photogrammetric survey, the method has still room for improvement for glacial and periglacial applications.

Future investigations are needed to assess the applicability of the method to other glaciers with different physical characteristics. The possibility to effectively combine GPS and photogrammetry in terrestrial applications with accurate (from cm to dm level) georeferencing of the survey without GCPs should be evaluated in practical applications.

In conclusion, the affordability and the flexibility of SfM-photogrammetry opens up the possibility of using high resolution topography as a monitoring tool in areas of limited vegetation, in a way that would be time consuming, difficult, and expensive with airborne and terrestrial LiDAR. The limited ability to predetermine data quality in SfM-photogrammetry survey and the variable success of surveys (which can only be evaluated after field campaigns are complete) is perhaps the biggest weakness in the approach. The thesis intend to deal the practical issues of a ground-based photogrammetry survey and the relative accuracies of the reconstructed surfaces by providing several survey configurations based on real applications in natural environments. To evaluate the accuracy of the SfM-photogrammetric results and possible deformations in object space, ground truth measurements obtained by other technique were used in this work. A key goal for each practical applications was to find an appropriate balance between the affordability and accessibility of the system (i.e. cost, speedy and espy of use and the quality of the resulting topographic data (accuracy and density). The methodology from data acquisition to data processing was plan to be easily implemented by a person working alone, or in situation where data collection must be expedited. In the thesis, the adopted methodology of the SfM-photogrammetry workflow is described for each case study with the intent to provide suggestions for others practical applications with similar requirements.

REFERENCES

Abdalati W., Krabill W.B. 1999. Calculation of ice velocities in the Jakobshavn Isbrae area using airborne laser altimetry. Remote Sensing of Environment 67(2):194-204.

Abermann J., Fischer A., Lambrecht A., Geist T. 2010. On the potential of very high-resolution repeat DEMs in glacial and periglacial environments. The Cryosphere 4:53-65. doi:10.5194/tc-4-53-2010

AgiSoft LLC 2010a. AgiSoft PhotoScan Professional Edition. Version 1.0.3, available at: http://www.agisoft.ru/products/photoscan/ (last access: 18 January 2015).

AgiSoft LLC 2010b. AgiSoft PhotoScan professional edition. Version 1.1.5. Retrieved from http://www.agisoft.ru/products/photoscan/

AgiSoft LLC 2010c. AgiSoft PhotoScan User-manuals Version 1.0, available at: http://www.agisoft.com/pdf/photoscan-pro_1_1_en.pdf (last access: 15 May 2015).

Aguilar F.J., Mills J. 2008. Accuracy assessment of lidar-derived digital elevation models, Photogramm. Rec., 23:148–169.

Ahmadabadian, A. H., Robson, S., Boehm, J., Shortis, M., Wenzel, K., Fritsch, D. 2013. A comparison of dense matching algorithms for scaled surface reconstruction using stereo camera rigs. ISPRS Journal of Photogrammetry and Remote Sensing, 78, pp. 157-167.

Alsadik B., Remondino F., Menna F., Gerke M., Vosselman G. 2013. Robust extraction of image correspondences exploiting the image scene geometry and approximate camera orientation. ISPRS Int. Arch. Photogramm. Remote Sens. Spat. Inf. Sci. 40(5/W1):1-7. doi:10.5194/isprsarchives-XL-5-W1-1-2013.

Arnold N.S., Willis I.C., Sharp M.J., Richards K.S., Lawson W.J. 1996. A distributed surface energy-balance model for a small valley glacier. I. Development and testing for Haut Glacier d'Arolla, Valais, Switzerland. Journal of Glaciology 42(140):77-89.

Arya S., Mount D.M. 1993. Approximate Nearest Neighbor Queries in Fixed Dimensions. In SODA 93:271-280.

Arya S., Mount D.M., Netanyahu N.S., Silverman R., Wu A.Y. 1998. An optimal algorithm for approximate nearest neighbor searching fixed dimensions. Journal of the ACM (JACM) 45(6):891-923.

Avian M., Kellerer-Pirklbauer A., Bauer A. 2009. LiDAR for monitoring mass movements in permafrost environments at the cirque Hinteres Langtal, Austria, between 2000 and 2008. Natural Hazards and Earth System Science 9(4):1087-1094.

Baltsavias E.P., Favey E., Bauder A., Bosch H., Pateraki M. 2001. Digital Surface Modelling by Airborne Laser Scanning and Digital Photogrammetry for Glacier Monitoring. The Photogrammetric Record 17:243–273. doi: 10.1111/0031-868X.00182

Barrand N.E., Murray T., James T.D., Barr S.L., Mills J.P. 2009. Optimizing photogrammetric DEMs for glacier volume change assessment using laser-scanning derived ground-control points. Journal of Glaciology 55(189):106-116.

Barsch D. 1996. Rockglaciers. Indicators for the permafrost and former geoecology in high mountain environments. Springer, Berlin, 331p.

Bay H., Ess A., Tuytelaars T., Van Gool L. 2008. Speeded-up robust features (SURF). Computer vision and image understanding 110(3):346-359.

Bemis S., Micklethwaite S., Turner D. 2014. Ground-based and UAV-Based photogrammetry: A multi-scale, high-resolution mapping tool for Structural Geology and Paleoseismology. J Struct Geol. 69:163-178. doi:10.1016/j.jsg.2014.10.007.

Bentley J.L. 1975. Multidimensional binary search trees used for associative searching. Communications of the ACM 18(9):509-517.

Bertone A. 2014. Misure di spostamento dei rock glacier con l'uso di feature tracking applicato a DTM multitemporali, BSc Thesis, Department of Earth and Environmental Sciences, University of Pavia, Pavia, Italy, 63 pp.

Besl P.J., McKay N.D. 1992. Method for registration of 3-D shapes, in: Proceedings of the International Society for Optics and Photonics IEEE Transactions on Pattern Analysis and Machine\Intelligence 1611:586-606.

Börlin N., Grussenmeyer P. Camera calibration using the damped bundle adjustment toolbox. ISPRS Annals - Volume II-5, 2014: ISPRS Technical Commission V Symposium 23–25 June 2014, Riva del Garda, Italy, 2014, Vol. II-5, pp. 89-96, doi:10.5194/isprsannals-II-5-89-2014,2014.

Bradley D., Boubekeur T., Heidrich W. 2008. Accurate multi-view reconstruction using robust binocular stereo and surface meshing. In Computer Vision and Pattern Recognition, 2008. CVPR 2008. IEEE Conference on (pp. 1-8). IEEE

Braithwaite R. J. Raper S.C. 2009. Glacier volume response time and its links to climate and topography based on a conceptual model of glacier hypsometry. The Cryosphere 3(2):183-194.

Brasington J., Vericat D., Rychkov I. 2012. Modeling riverbed morphology, roughness, and surface sedimentology using high resolution terrestrial laser scanning. Water Resources Research 48.11.

Bretar F., Arab-Sedze M., Champion J., Pierrot-Deseilligny M., Heggy E., Jacquemoud S. 2013. An advanced photogrammetric method to measure surface roughness: Application to volcanic terrains in the Piton de la Fournaise, Reunion Island. Remote Sensing of Environment 135:1-11.

Brown M., Lowe D.G. 2007. Automatic panoramic image stitching using invariant features. International journal of computer vision 74(1):59-73.

Bühler Y., Graf C. 2013. Sediment transfer mapping in a high-alpine catchment using airborne LiDAR. GRAF C (Red.) Mattertal – ein Tal in Bewegung, Publikation zur Jahrestagung der Schweizerischen Geomorphologischen Gesellschaft, 29 June–1 July 2011, Eidg. Forschungsanstalt WSL, St. Niklaus, Birmensdorf, Switzerland, pp. 113-124.

Bühler Y., Marty M., Egli L., Veitinger J., Jonas T., Thee P., Ginzler C. 2014. Spatially continuous mapping of snow depth in high alpine catchments using digital photogrammetry, The Cryosphere Discuss 8:3297–3333. doi: 10.5194/tcd-8-3297-2014.

Calonder M., Lepetit V., Strecha C., Fua P. 2010. Brief: Binary robust independent elementary features. Computer Vision–ECCV 2010, 778-792.

Carturan L. 2010. Climate change effects on the cryosphere and hydrology of a high-altitude watershed, PhD thesis, Department of Land, Environment, Agriculture and Forestry, University of Padova, Padova, Italy.

Carturan L. 2015. Starting new mass balance observations close to decaying monitored glaciers: La Mare Glacier (Ortles-Cevedale, Italian Alps), J. Glaciol., in preparation.

Carturan L., Baldassi G.A., Bondesan A., Calligaro S., Carton A., Cazorzi F., Dalla Fontana G., Francese R., Guarnieri A., Milan N., Moro D., Tarolli P. 2013b. Current behaviour and dynamics of the lowermost italian glacier (Montasio Occidentale, Julian Alps). Geografiska Annaler: Series A, Physical Geography 95(1):79-96.

Carturan L., Baroni C., Carton A., Cazorzi F., Dalla Fontana G., Delpero C., Zanoner T. 2014. Reconstructing Fluctuations of La Mare Glacier (Eastern Italian Alps) in the Late Holocene: new Evidence for a Little Ice Age Maximum Around 1600 AD. Geografiska Annaler: Series A, Physical Geography 96:287–306.

Carturan L., Blasone G., Calligaro S., Carton A., Cazorzi F., Dalla Fontana G., Moro D. 2013c. High-Resolution Monitoring of Current Rapid Transformations on Glacial and Periglacial Environments. Int. Arch. Photogramm. Remote Sens. Spatial Inf. Sci., XL-5/W3:39-44. doi:10.5194/isprsarchives-XL-5-W3

Carturan L., Cazorzi F., Dalla Fontana G. 2009. Enhanced estimation of glacier mass balance in unsampled areas by means of topographic data, Ann. Glaciol. 50:37–46.

Carturan L., Filippi R., Seppi R., Gabrielli P., Notarnicola C., Bertoldi L., Paul F., Rastern P., Cazorzi F., Dinale R., Dalla Fontana G. 2013a. Area and volume loss of the glaciers in the Ortles-Cevedale group (Eastern Italian Alps): controls and imbalance of the remaining glaciers. The Cryosphere 7:1339–1359.

Carturan L., Zuecco G., Seppi R., Zanoner Z., Borga M., Carton A., Dalla Fontana G. 2015. Catchment-scale permafrost mapping using spring water characteristics, Permafrost Periglac. (in press.).

Castillo C., Pérez R., James M.R., Quinton J.N., Taguas E.V., Gómez J.A. 2012. Comparing the accuracy of several field methods for measuring gully erosion, Soil Sci. Soc. Am. J. 76:1319–1332. doi:10.2136/sssaj2011.0390.

Chen Y., Medioni G. 1991. Object modeling by registration of multiple range images, in: Proceedings, IEEE International Conference on Robotics and Automation, 9–11 April, Sacramento, CA, USA, 10:145–155.

Clapuyt F., Vanacker V., Van Oost K. 2015. Reproducibility of uav-based earth topography reconstructions based on structure-from-motion algorithms. Geomorphology (in press). doi:10.1016/j.geomorph.2015.05.011.

Cogley J.G. 2009. Geodetic and direct mass-balance measurements: comparison and joint analysis, Ann. Glaciol. 50:96-100.

Cogley J.G., Adams W.P. 1998. Mass balance of glaciers other than the ice sheets, J. Glaciol. 44:315-325.

Cogley J.G., Hock R., Rasmussen L.A., Arendt A.A., Bauder A., Braithwaite R.J., Zemp M. 2011. Glossary of glacier mass balance and related terms. IHP-VII Technical Documents in Hydrology 86.

Colucci R.R., Forte E., Boccali C., Dossi M., Lanza L., Pipan M., Guglielmin M. 2015. Evaluation of internal structure, volume and mass of glacial bodies by integrated

LiDAR and ground penetrating radar surveys: the case study of Canin Eastern Glacieret (Julian Alps, Italy), Surv. Geophys. 36:231-252.

Dai F., Feng Y., Hough R. 2014. Photogrammetric error sources and impacts on modeling and surveying in construction engineering applications. Visualization in Engineering 2(1):2.

Dall'Asta E., Delaloye R., Diotri F., Forlani G., Fornari M., Morra di Cella U., Pogliotti P., Roncella R., Santise M. 2015. Use of UAS in a high mountain landscape: the case of gran sommetta rock glacier (AO), The International Archives of the Photogrammetry, Remote Sensing and Spatial Information Sciences, Volume XL-3/W3:391–397.

Dall'Asta E., Thoeni K., Santise M., Forlani G., Giacomini A., Roncella R 2015b. Network design and quality checks in automatic orientation of close-range photogrammetric blocks, Sensors 15:7985–8008.

Dandois J.P., Ellis E.C. 2013. High spatial resolution three-dimensional mapping of vegetation spectral dynamics using computer vision, Remote Sens. Environ., 136, 259–276, doi:10.1016/j.rse.2013.04.005.

Deems J.S., Painter T.H., Finnegan D.C. 2013. Lidar measurement of snow depth: a review, J. Glaciol. 59:467–479.

Delon J., Rougé B. 2007. Small baseline stereovision. Journal of Mathematical Imaging and Vision 28(3):209-223.

Diefenbach A.K., Crider J.G., Schilling S.P., Dzurisin D. 2012. Rapid, low-cost photogrammetry to monitor volcanic eruptions: an example from Mount St. Helens, Washington, USA. Bulletin of volcanology 74(2):579-587.

Dietrich J.T. 2015. Riverscape mapping with helicopter-based Structure-from-Motion photogrammetry. Geomorphology 252:144–157.

Eltern A., Kaiser A., Castillo C., Rock G., Neugirg F., Abellan A. 2015. Image-based surface reconstruction in geomorphometry – merits, limits and developments of a promising tool for geoscientists Earth Surf. Dynam. Discuss. 3:1445–1508. doi:10.5194/esurfd-3-1445-2015.

Eltner A., Schneider D. 2015. Analysis of different methods for 3-D reconstruction of natural surfaces from parallel-axes UAV images, Photogramm. Rec. 30:279–299. doi:10.1111/phor.12115.

Eltner A., Mulsow C., Maas H. 2013. Quantitative measurement of soil erosion from TLS and UAV data, Int. Arch. Photogramm. Rem. Sens. XL-1/W2:119–124.

Favalli M., Fornaciai A., Isola I., Tarquini S., Nannipieri L. 2012. Multiview 3D reconstruction in geosciences, Comput. Geosci. 44:168–176.

Fey C., Rutzinger M., Wichmann V., Prager C., Bremer M., Zangerl C. 2015. Deriving 3D displacement vectors from multi-temporal airborne laser scanning data for landslide activity analyses. GIScience & Remote Sensing 52(4):437-461. doi:10.1080/15481603.2015.1045278.

Fischer L., Eisenbeiss H., Kääb A., Huggel C., Haeberli W. 2011. Monitoring topographic changes in a periglacial high-mountain face using high-resolution DTMs, Monte Rosa East Face, Italian Alps, Permafrost Periglac. 22:140–152.

Fischler M.A., Bolles R.C. 1981. Random sample consensus: a paradigm for model fitting with applications to image analysis and automated cartography. Communications of the ACM 24(6):381-395.

Fisher P.F., Tate N.J. 2006. Causes and consequences of error in digital elevation models. Progress in Physical Geography 30(4):467-489.

Fisher R.B., Breckon T.P., Dawson-Howe K., Fitzgibbon A., Robertson C., Trucco E., Williams C.K. 2013. Dictionary of computer vision and image processing. John Wiley & Sons.

Fonstad M.A., Dietrich J.T., Courville B.C., Jensen J.L., Carbonneau P.E. 2013. Topographic structure from motion: a new development in photogrammetric measurement. Earth Surface Processes and Landforms 38(4):421-430.

Fox A.J., Gooch M.J. 2001. Automatic Dem Generation for Antarctic Terrain. The Photogrammetric Record 17:275–290. doi: 10.1111/0031-868X.00183

Frankl A., Stal C., Abraha A., Nyssen J., Rieke-Zapp D., DeWulf A., Poesen J. 2014. Detailed recording of gully morphology in 3-D through image-based modelling PhotoScan Digital Elevation Model (DEM) soil pipes Structure from Motion–Multi View Stereo (SfM–MVS) volume calculation, Catena 127:92–101. doi:10.1016/j.catena.2014.12.016.

Fraser C.S. 1996. Network design. In “Close-range Photogrammetry and Machine Vision”, Atkinson (Ed.), Whittles Pubblishing, UK, pp.256-282.

Friedman J.H., Bentley J.L., Finkel R.A. 1977. An algorithm for finding best matches in logarithmic expected time. ACM Transactions on Mathematical Software (TOMS) 3(3):209-226.

Furukawa Y., Ponce J. 2010. Accurate, dense, and robust multiview stereopsis. Pattern Analysis and Machine Intelligence, IEEE Transactions 32(8):1362-1376.

Gauthier D., Conlan M., Jamieson B. 2014. Photogrammetry of fracture lines and avalanche terrain: potential applications to research and hazard mitigation projects, Proceedings, International Snow Science Workshop, Banff, 29 September–3 October 2014:109–115.

Geist T., Stotter J. 2007. Documentation of glacier surface elevation change with multi temporal airborne laser scanner data – case study: Hintereisferner and Kesselwandferner, Tyrol, Austria, Zeitschrift fur Gletscherkunde und Glazialgeologie 41:77–106.

Glira P., Pfeifer N., Briese C., Ressl C. 2015. A correspondence framework for ALS strip adjustments based on variants of the ICP algorithm. PFG Photogrammetrie, Fernerkundung, Geoinformation 4:275-289. doi:10.1127/pfg/2015/0270.

Gómez-Gutiérrez Á., de Sanjosé-Blasco J.J., de Matías-Bejarano J., Berenguer-Sempere F. 2014. Comparing Two Photo-Reconstruction Methods to Produce High Density Point Clouds and DEMs in the Corral del Veleta Rock Glacier (Sierra Nevada, Spain). Remote Sensing 6(6):5407-5427.

Gómez-Gutiérrez Á., de Sanjosé-Blasco J.J., Lozano-Parra J., Berenguer-Sempere .F, de Matías-Bejarano J. 2015. Does HDR pre-processing improve the accuracy of 3D models obtained by means of two conventional SfM-MVS software packages? The case of the Corral del Veleta Rock Glacier, Remote Sensing 7:10269–10294.

Grün A. 2012. Development and status of image matching in photogrammetry, Photogramm. Rec. 27:36–57. doi:10.1111/j.1477-9730.2011.00671.x.

Haeberli W., Hoelzle M., Paul F., Zemp M. 2007. Integrated monitoring of mountain glaciers as key indicators of global climate change: the European Alps. Annals of Glaciology 46(1):150-160.

Haeberli W., Bösch H., Scherler K., Østrem G., Wallén CC. 1989. World Glacier Inventory; Status 1988. A Contribution to the Global Environment Monitoring System (GEMS) and the International Hydrological Programme, Compiled by the World Glacier Monitoring Service. IASH Press.

Haug T., Rolstad C., Elvehøy H., Jackson M., Maalen-Johansen I. 2009. Geodetic mass balance of the western Svartisen ice cap, Norway, in the periods 1968–1985 and 1985–2002, Ann. Glaciol. 50:119–125.

Höfle B., Geist T., Rutzinger M., Pfeifer N. 2007. Glacier surface segmentation using airborne laser scanning point cloud and intensity data, International Archives of Photogrammetry, Remote Sensing and Spatial Information Sciences 36 (W52):195–200.

Höfle B., Rutzinger M. 2011. Topographic airborne LiDAR in geomorphology: A technological perspective. Zeitschrift für Geomorphologie Supplementary Issues 55(2):1-29.

Hosseininaveh A., Sargeant B., Erfani T., Robson S., Shortis M., Hess M., Boehm J. 2014. Towards fully automatic reliable 3D acquisition: from designing imaging network to a complete and accurate point cloud, Robotics and Autonomous Systems 62:1197–1207.

Huss M. 2013. Density assumptions for converting geodetic glacier volume change to mass change. The Cryosphere 7(3):877-887.

Immerzeel W.W., Kraaijenbrink P.D.A., Shea J.M., Shrestha A.B., Pellicciotti F., Bierkens M.F.P., De Jong S.M. 2014. High-resolution monitoring of Himalayan glacier dynamics using unmanned aerial vehicles, Remote Sens. Environ. 150:93–103.

James M.R., Robson S. 2012. Straightforward reconstruction of 3D surfaces and topography with a camera: accuracy and geoscience application. Journal of Geophysical Research - Earth Surface 117:F03017. doi:10.1029/2011JF002289.

James M.R., Robson S. 2014. Mitigating systematic error in topographic models derived from UAV and ground-based image networks. Earth Surf Process Landforms 39:1413-1420. doi:10.1002/esp.3609.

Javernick L., Brasington J., Caruso B. 2014. Modelling the topography of shallow braided rivers using Structure-from-Motion photogrammetry. Geomorphology.

Joerg P.C., Zemp M. 2014. Evaluating Volumetric Glacier Change Methods Using Airborne Laser Scanning Data. Geografiska Annaler: Series A, Physical Geography 96:135–145.

Johnson K., Nissen E., Saripalli S., Arrowsmith J. R., Mcgarey P., Scharer K., Williams P., Blisniuk K. 2014. Rapid mapping of ultrafine fault zone topography with structure from motion, Geosphere 10:969. doi:10.1130/GES01017.1.

Kääb A. 2002. Monitoring high-mountain terrain deformation from repeated air-and spaceborne optical data: examples using digital aerial imagery and ASTER data. ISPRS Journal of Photogrammetry and remote sensing 57:39–52.

Kääb A. 2005. Remote Sensing of Mountain Glaciers and Permafrost Creep. Research Perspectives from Earth Observation Technologies and Geoinformatics, Schriftenreihe Physische Geographie, Glaziologie und Geomorphodynamik, 48, University of Zurich, Zurich, Switzerland.

Kääb A., Funk M. 1999. Modelling mass balance using photogrammetric and geophysical data: a pilot study at Griesgletscher, Swiss Alps. Journal of Glaciology 45(151):575-583.

Kääb A., Girod L., Berthling I. 2014. Surface kinematics of periglacial sorted circles using Structure-from-Motion technology. The Cryosphere Discussions 7(6):6043-6074.

Kääb A., Haeberli W., Gudmundsson G.H. 1997. Analyzing the creep of mountain permafrost using high precision aerial photogrammetry: 25 years of monitoring Gruben rock glacier, Swiss Alps, Permafrost Periglac. 8:409–426.

Kääb A., Kaufmann V., Ladstädter R., Eiken T. 2003. Rock glacier dynamics: implications from high-resolution measurements of surface velocity fields, in: Eighth International Conference on Permafrost, 21–25 July 2003, Zurich, Switzerland 1:501–506.

Kääb A., Vollmer M. 2000. Surface geometry, thickness changes and flow fields on creeping mountain permafrost: automatic extraction by digital image analysis. Permafrost and Periglacial Processes 11(4):315-326.

Kaiser A., Neugirg F., Haas F., Schmidt J., Becht M., Schindewolf M. 2015. Determination of hydrological roughness by means of close range remote sensing, SOIL 1:613–620. doi:10.5194/soil-1-613-2015.

Karpilo J.R., Ronald D. 2009. Glacier monitoring techniques. Geological Monitoring: Boulder, Colorado, Geological Society of America 2009:141-162.

Kaufmann V. 1998. Deformation analysis of the Doesen rock glacier (Austria), in: Proceedings of the 7th International Permafrost Conference, 23–27 June 1998, Yellowknife, Canada 551–556.

Kaufmann V., Ladstädter R. 2008. Application of terrestrial photogrammetry for glacier monitoring in Alpine environments. Ele 2700.2800, 2900.

Kellerer-Pirklbauer A. 2005. Alpine permafrost occurrence at its spatial limits: First results from the eastern margin of the European Alps. Norsk Geografisk Tidsskrift-Norwegian Journal of Geography 59(2):184-193.

Knoll C., Kerschner H. 2010. A glacier inventory for South Tyrol, Italy, based on airborne laserscanner data, Ann. Glaciol. 50:46–52.

Kodde M.P., Pfeifer N., Gorte B.G.H., Geist T., Höfle B. 2007. Automatic glacier surface analysis from airborne laser scanning, International Archives of the Photogrammetry, Remote Sensing and Spatial Information Sciences 36:221–226.

Krabill W., Frederick E., Manizade S., Martin C., Sonntag J., Swift R., Yungel J. 1999. Rapid thinning of parts of the southern Greenland ice sheet. Science 283(5407):1522-1524.

Kraus K. 1997. Photogrammetry. Volume 2: Advanced Methods and Applications. Ferd.Dümmlers Verlag.

Lague D., Brodu N., Leroux J. 2013. Accurate 3-D comparison of complex topography with terrestrial laser scanner: application to the Rangitikei canyon (N-Z), ISPRS J. Photogramm. 82:10–26. doi:10.1016/j.isprsjprs.2013.04.009.

Lambiel C., Delaloye R. 2004. Contribution of real-time kinematic GPS in the study of creeping mountain permafrost: examples from the Western Swiss Alps. Permafrost and periglacial processes 15(3):229-241.

Lowe DG. 2004. Distinctive image features from scale-invariant keypoints. International journal of computer vision 60(2):91-110.

Mancini F., Dubbini M., Gattelli M., Stecchi F., Fabbri S., Gabbianelli G. 2013. Using unmanned aerial vehicles (UAV) for high-resolution reconstruction of topography: the structure from motion approach on coastal environments, Remote Sensing 5:6880-6898. doi:10.3390/rs5126880.

Mathews A.J., Jensen J.L. 2013. Visualizing and quantifying vineyard canopy LAI using an unmanned aerial vehicle (UAV) collected high density structure from motion point cloud. Remote Sensing 5(5):2164-2183.

Micheletti N., Chandler J.H., Lane S.N. 2014. Investigating the geomorphological potential of freely available and accessible Structure-from-Motion photogrammetry using a smartphone. Earth Surface Processes and Landforms. doi: 10.1002/esp.3648.

Micusik B., Pajdla T. 2006. Structure from motion with wide circular field of view cameras. Pattern Analysis and Machine Intelligence, IEEE Transactions 28(7):1135-1149.

Morel J.M., Yu G. 2009. ASIFT: A new framework for fully affine invariant image comparison. SIAM Journal on Imaging Sciences 2(2):438-469.

Muja M., Lowe D.G. 2009. Flann, fast library for approximate nearest neighbors. In International Conference on Computer Vision Theory and Applications (VISAPP'09).

Müller J., Gärtner-Roer I., Thee P., Ginzler C. 2014. Accuracy assessment of airborne photogrammetrically derived high-resolution digital elevation models in a high mountain environment. ISPRS Journal of Photogrammetry and Remote Sensing 98:58–69.

Munkelt C., Trummer M., Denzler J., Wenhardt S. 2007. Benchmarking 3D Reconstructions from Next Best View Planning. In MVA (pp. 552-555). Nilosek D, Sun S, Salvaggio C 2012. Geo-accurate model extraction from three-dimensional image-derived point clouds, in: Proceedings of SPIE, Algorithms and Technologies for Multispectral, Hyperspectral, and Ultraspectral Imagery XVIII, 23 April 2012, Baltimore, MD, USA, 8390, 83900J, doi:10.1117/12.919148.

Nocerino E., Menna F., Remondino F. 2014. Accuracy of typical photogrammetric networks in cultural heritage 3D modeling projects. ISPRS-International Archives of the Photogrammetry, Remote Sensing and Spatial Information Sciences 1:465–472.

Nocerino E., Menna F., Remondino F., Saleri R. 2013. Accuracy and block deformation analysis in automatic UAV and Terrestrial photogrammetry–Lesson learnt. ISPRS Annals of the Photogrammetry, Remote Sensing and Spatial Information Sciences, Vol. II-5/W1, XXIV International CIPA Symposium, 2-6 September, Strasbourg, France.

Ouédraogo M.M., Degré A., Debouche C., Lisein J. 2014. The evaluation of unmanned aerial system-based photogrammetry and terrestrial laser scanning to generate DEMs of agricultural watersheds, Geomorphology 214:339–355. doi:10.1016/j.geomorph.2014.02.016.

Paul F., Huggel C., Kääb A. 2004. Combining satellite multispectral image data and a digital elevation model for mapping debris-covered glaciers. Remote Sensing of Environment 89(4):510-518.

Pellikka P., Rees W.G. 2009. Remote Sensing Of Glaciers: Techniques For Topographic, Spatial and Thematic Mapping of Glaciers, CRC Press, University of Cambridge, Cambridge, UK.

Piermattei L., Carturan L., Guarnieri A. 2015. Use of terrestrial photogrammetry based on structure from motion for mass balance estimation of a small glacier in the Italian Alps. Earth Surf. Proc. Land. 40:1791-1802. doi:10.1002/esp.3756, 2015.

Pierrot-Deseilligny M., Clery I.: APERO, an open source bundle adjustment software for automatic calibration and orientation of set of images, Intern. Arch. Photogramm. Rem. Sens. 38(5):269–276.

Prosdocimi M., Sofia G., Dalla Fontana G., Tarolli P. 2015. Bank erosion in agricultural drainage networks: effectiveness of Structure-from-Motion for post-event analysis, Earth Surf. Proc. Land. 40:1891-1906. doi:10.1002/esp.3767.

Quan L., Kanade T. 2010. Affine structure from line correspondences with uncalibrated affine cameras. Pattern Analysis and Machine Intelligence, IEEE Transactions 19(8):834-845.

Remondino F., Menna F., Koutsoudis A., Chamzas C., El-Hakim S. 2013. Design and implement a reality-based 3D digitisation and modelling project. In Proceedings of the Digital Heritage International Congress pp. 137-144.

Remondino F., Fraser C. 2006. Digital camera calibration methods: considerations and comparisons. International Archives of Photogrammetry, Remote Sensing and Spatial Information Sciences 36(5):266-272.

Remondino F., Del Pizzo S., Kersten T., Troisi S. 2012. Low-cost and open source solutions for automated image orientation-A critical overview. Proc. EuroMed 2012 Conference, LNCS 7616:40-54.

Rippin D.M., Pomfret A., King N. 2015. High resolution mapping of supraglacial drainage pathways reveals link between micro-channel drainage density, surface roughness and surface reflectance, Earth Surf. Proc. Land. 40:1279–1290. doi:10.1002/esp.3719.

Robertson D.P., Cipolla R. 2009. Structure from Motion. In: Varga, M. (Ed.), Practical Image Processing and Computer Vision. John Wiley, Chichester.

Roer I., Nyenhuis M. 2007. Rockglacier activity studies on a regional scale: comparison of geomorphological mapping and photogrammetric monitoring, Earth Surf. Proc. Land. 32:1747-1758.

Rumpler M., Daftry S., Tscharf A., Prettenthaler R., Hoppe C., Mayer G., Bischof H. 2014. Automated end-to-end workflow for precise and geo-accurate reconstructions using fiducial markers. ISPRS Ann. Photogramm. Remote Sens. Spatial Inf. Sci. 2(3):135-142. doi:10.5194/isprsannals-II-3-135-2014.

Ryan J.C., Hubbard A.L. Box J.E., Todd J., Christoffersen P., Carr J.R., Holt T.O., Snooke N. 2015. UAV photogrammetry and structure from motion to assess calving dynamics at Store Glacier, a large outlet draining the Greenland ice sheet, The Cryosphere 9:1-11. doi:10.5194/tc-9-1-2015.

Scaioni M. 2015. Modern Technologies for Landslide Monitoring and Prediction, Springer Natural Hazard. doi:10.1007/978-3-662-45931-7_10.

Scambos T.A., Dutkiewicz M.J., Wilson J.C., Bindschadler R.A. 1992. Application of image cross-correlation to the measurement of glacier velocity using satellite image data. Remote Sensing of Environment 42(3):177-186.

Schaffhauser et al., (2008

Scharstein D., Szeliski R. 2002. A taxonomy and evaluation of dense two-frame stereo correspondence algorithms. International journal of computer vision 47(1-3):7-42.

Seitz S.M., Curless B., Diebel J., Scharstein D., Szeliski R. 2006, June. A comparison and evaluation of multi-view stereo reconstruction algorithms. In Computer vision and pattern recognition, 2006 IEEE Computer Society Conference 1:519-528.

Seppi R., Carton A., Zumiani M., Dall'Amico M., Zampedri G., Rigon R. 2012. Inventory, distribution and topographic features of rock glaciers in the southern region of the Eastern Italian Alps (Trentino). Geografia Fisica e Dinamica Quaternaria 35:185-197. doi:10.4461/GFDQ.2012.35.17.

Smith M., Carrivick J.L., Quincey D.J. 2015. Structure from motion photogrammetry in physical geography. Physical Geography 1-29. doi: 10.1177/0309133315615805

Smith M.W., Vericat D. 2015. From experimental plots to experimental landscapes: topography, erosion and deposition in sub-humid badlands from Structure-from-Motion photogrammetry. Earth Surf. Proc. Land. 40:1656-1671. doi: 10.1002/esp.3747.

Snavely N., Seitz S.M., Szeliski R. 2006. Photo tourism? exploring photo collections in 3-D, ACM T. Graphic., 25:835–846.

Snavely N., Seitz S.M., Szeliski R. 2008. Modeling the world from internet photo collections, Int. J. Comput. Vision 80:189–210. doi:10.1007/s11263-007-0107-3.

Solbø S., Storvold R. 2013. Mapping svalbard glaciers with the cryowing uas, ISPRS International Archives of the Photogrammetry, Remote Sensing and Spatial Information Sciences, XL-1/W2:373-377.

Steiner D., Pauling A., Nussbaumer S.U., Nesje A., Luterbacher J., Wanner H., Zumbühl H.J. 2008. Sensitivity of European glaciers to precipitation and temperature– two case studies. Climatic Change 90(4):413-441.

Stöcker C., Eltner A., Karrasch P. 2015. Measuring gullies by synergetic application of UAV and close range photogrammetry – a case study from Andalusia, Spain, Catena, 132:1–11. doi:10.1016/j.catena.2015.04.004.

Stumpf A., Malet J.P., Allemand P., Pierrot-Deseilligny M., Skupinski G. 2015. Ground-based multi-view photogrammetry for the monitoring of landslide deformation and erosion. Geomorphology 231:130-145.

Tamburini A., Deline P., Jaillet S., Mortara G., Conforti D. 2007. Application of terrestrial scanning LIDAR to study the evolution of ice contact Miage Lake and Miage Glacier ice cliff (Mont Blanc massif, Italy). Geophysical Research Abstracts 9:07718.

Tarolli P., Arrowsmith J.R., Vivoni E.R. 2009. Understanding earth surface processes from remotely sensed digital terrain models. Geomorphology 113(1):1-3.

Thoeni K., Giacomini A., Murtagh R., Kniest E. 2014. A comparison of multi-view 3D reconstruction of a rock wall using several cameras and a laser scanner. Int. Arch. Photogramm. Remote Sens. Spat. Inf. Sci, ISPRS Technical Commission V Symposium, 23-25 June, Riva del Garda, Italy, pp. 573-580.

Tonkin T.N., Midgley N.G., Graham D.J., Labadz J.C. 2014. The potential of small unmanned aircraft systems and structure-from-motion for topographic surveys: a test of emerging integrated approaches at Cwm Idwal, North Wales, Geomorphology 226:35–43.

Triggs B. 1999. Camera pose and calibration from 4 or 5 known 3d points. In Computer Vision, 1999. The Proceedings of the Seventh IEEE International Conference 1:278-284.

Tseng C.M., Lin C.W., Dalla Fontana G., Tarolli P. 2015. The topographic signature of a Major Typhoon, Earth Surf. Proc. Land. 40:1129-1136.

Ullman S. 1979. The interpretation of structure from motion. Proceedings of the Royal Society of London. Series B. Biological Sciences 203:405-426.

Unger J., Reich M., Heipke C. 2014. UAV-based photogrammetry: monitoring of a building zone. ISPRS-International Archives of the Photogrammetry, Remote Sensing and Spatial Information Sciences XL-5:601-606.

Verhoeven G., Doneus M., Bries C., Vermeulen F. 2012. Mapping by matching: a computer vision-based approach to fast and accurate georeferencing of archaeological aerial photographs. Journal of Archaeological Science 39:2060-2070.

Verhoeven G., Karel W., Štuhec S., Doneus M., Trinks I., Pfeifer N. 2015. Mind your grey tones – examining the influence of decolourization methods on interest point extraction and matching for architectural image-based modelling. 3D-Arch 2015–3D Virtual Reconstruction and Visualization of Complex Architectures, ISPRS, 25-27 February, Avila, Spain 40:307-314. doi: 10.5194/isprsarchives-XL-5-W4-307.

Viswanathan M. 2005. Measurement error and research design. Sage.

Wackrow R., Chandler J. 2011. Minimising systematic error surfaces in digital elevation models using oblique convergent imagery. The Photogrammetric Record 26(133):16-31. doi.org/10.1111/j.1477-9730.2011.00623.x.

Wackrow R., Chandler J.H. 2008. A convergent image configuration for DEM extraction that minimises the systematic effects caused by an inaccurate lens model. The Photogrammetric Record 23(121):6-18.

Welch R., Howarth P.J. 1968. Photogrammetric measurements of glacial landforms. The Photogrammetric Record 6:75-96. doi:10.1111/j.1477-9730.1968.tb00915.x

Wenzel K., Rothermel M., Fritsch D., Haala N. 2013. Image acquisition and model selection for multi-view stereo. Int. Arch. Photogramm. Remote Sens. Spatial Inf. Sci 251-258.

Westoby M.J., Brasington J., Glasser N.F. 2012. 'Structure-from-Motion' photogrammetry: A low-cost, effective tool for geoscience applications. Geomorphology 179:300-314.

Westoby M.J., Brasington J., Glasser N.F., Hambrey M.J., Reynolds J.M. 2012. 'Structure from Motion' photogrammetry: a low-cost, effective tool for geoscience applications. Geomorphology 179:300-314.

Whitehead K., Moorman B.J., Hugenholtz C.H. 2013. Brief Communication: Low-cost, ondemand aerial photogrammetry for glaciological measurement, The Cryosphere 7:1879-1884. doi:10.5194/tc-7-1879-2013.

Woodget A.S., Carbonneau P.E., Visser F. 2014. Quantifying submerged fluvial topography using hyperspatial resolution UAS imagery and structure from motion photogrammetry. Earth Surface Processes and Landforms 40:47-64. doi:10.1002/esp.3613.

Division of work

Division of work at Perarolo di Cadore, Test field

Partecipants: Livia Piermattei (LP), Alberto Guarnieri (AG), Mattia Caiazzo (MC).

- Research concept and design: LP (100%)
- Site renaissance: LP (100%)
- Photogrammetry data collection and processing: LP (100%)
- Total Station data collection: MC (100%)
- Total Station data processing: LP (100%)
- TLS data acquisition: AG (100%)
- TLS data processing: LP (100%)
- GPS data collection: AG (70%), MC (30%)
- GPS data processing: AG (80%), LP (20%)
- Subsequent analysis: LP (100%)

Division of work at La Mare glacier and AVDM3 Rock glacier

Partecipants: Livia Piermattei (LP), Luca Carturan (LC), Fabrizio de Blasi (FB).

- Research concept and design: LP (80%), LC (20%)
- Site renaissance: LC (100%)
- Photogrammetry data collection: LP (50%, AVDM3 Rock Glacier survey 2014), LC (50%, La Mare Glacier survey 2013 and 2014)
- Photogrammetry data processing: LP (100%)
- ALS data processing: LP (20%), FB (80%). Additional, Philipp Glira (TU Vienna) for the supporting on ALS data processing with Opals.
- Subsequent analysis: LP (100%)

Division of work at Montasio Occidentale Glacier

Partecipants: Livia Piermattei (LP), Simone Calligaro (SC), Giacomo Blasone (GB), Federico Cazorzi (FC), Luca Carturan (LC), Emanuele Forte (EF), Renato Roberto Colucci (RC). Additional fieldwork assistance from Daniele Moro and Giovanni Baldassi is also gratefully acknowledged.

- Research concept and design: LP (80%), LC (20%)
- Site renaissance: LC (50%), FC (40%), RC (10%)
- Photogrammetry data collection: LP (70%, 2013-2014), GB (30%, 2012)
- Photogrammetry data processing: LP (100%)
- TLS and GPS data acquisition: SC (100%)
- TLS data processing: LP (90%), SC (10%)
- GPR data acquisition and processing: RC (50%), EF (50%)
- Subsequent analysis: LP (100%)

Photogrammetric workflow adopted for each case study

Test field

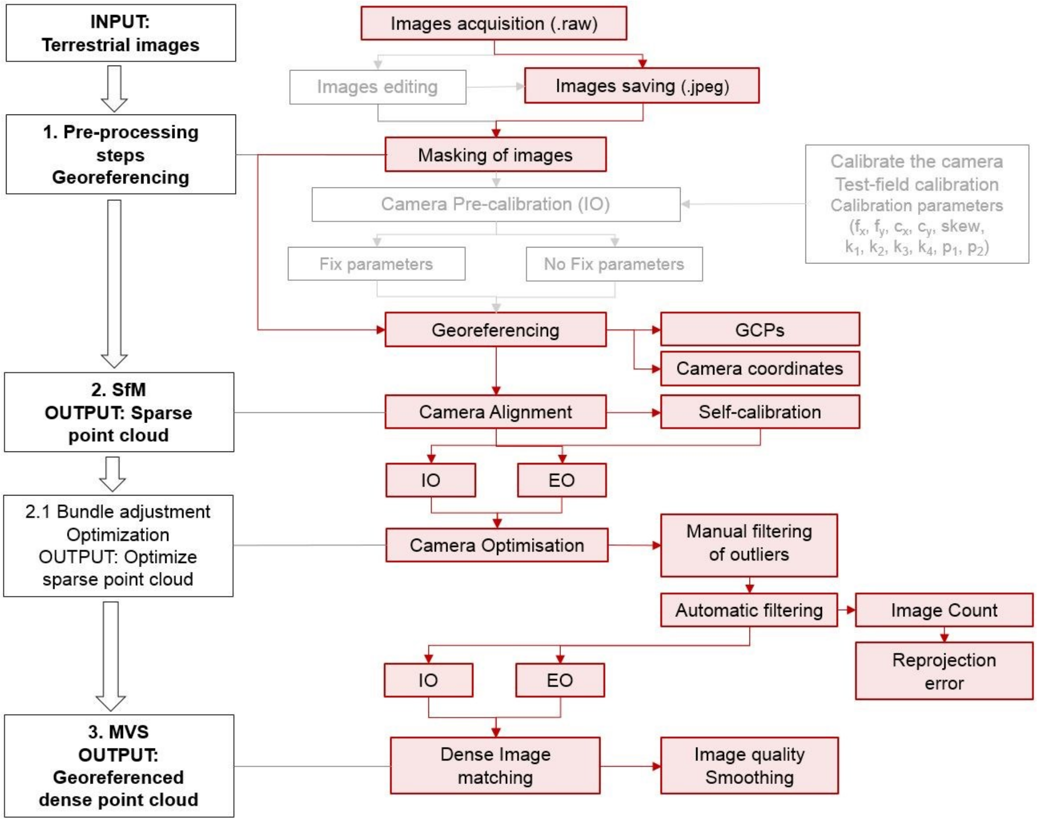

Figure A1. Image processing workflow with PhotoScan. The red lines represents the SfM-MVS workflow used to process the imagery dataset of the Test field.

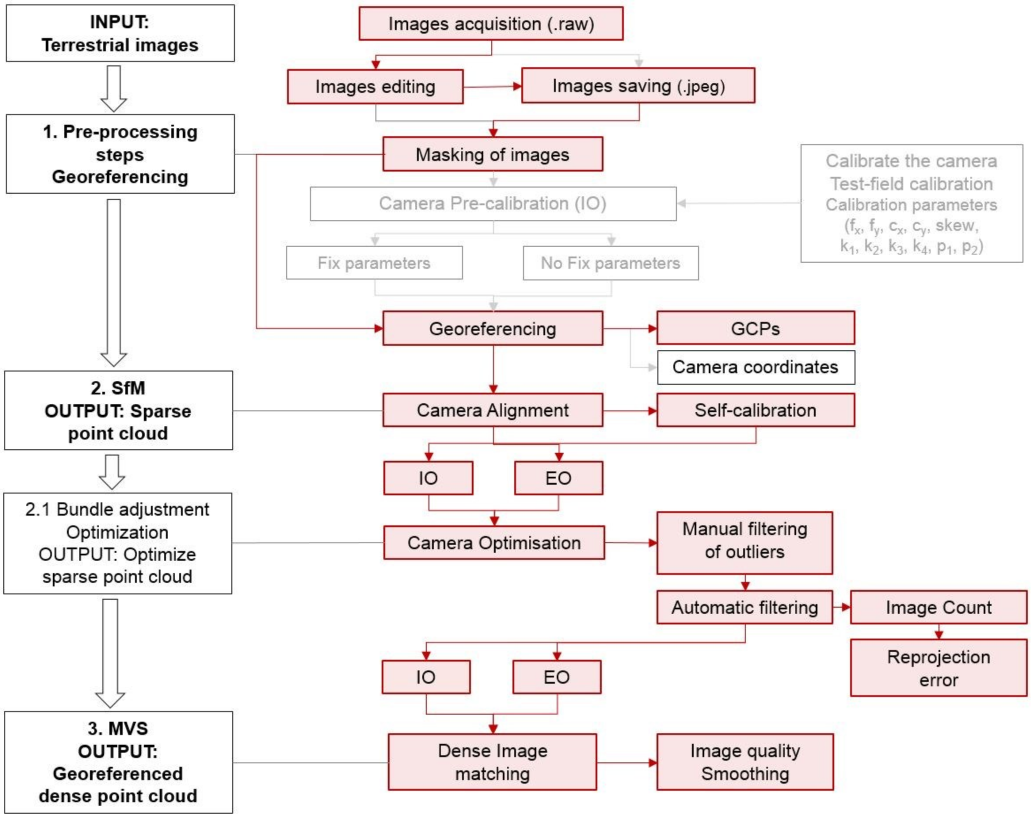

Figure A2. Image processing workflow with PhotoScan. The red lines represents the SfM-MVS workflow used to process the imagery dataset of the Montasio Occidentale glacier.

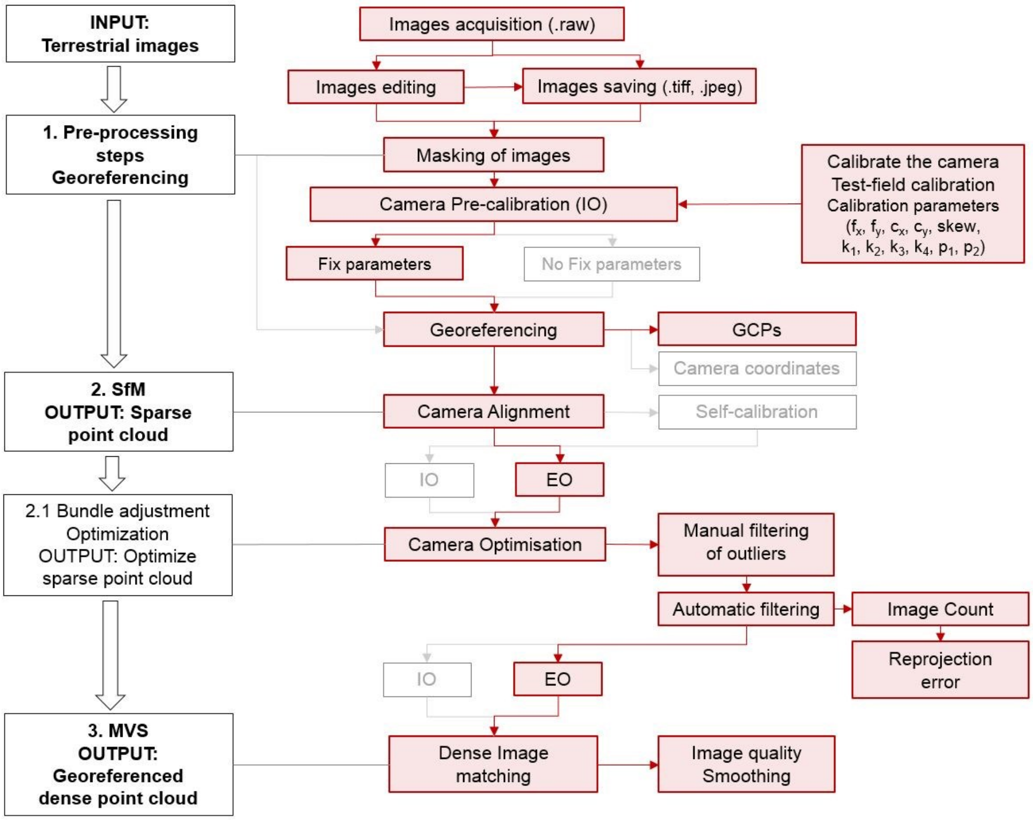

Figure A3. Image processing workflow with PhotoScan. The red lines represents the SfM-MVS workflow used to process the imagery dataset of the La Mare Glacier and the AVDM3 Rock glacier case study.

Test field

Table A.1 Coordinates of targets measured with Total Station and with the TLS after the transformation in the reference system of WGS84-UTM33N defined by the targets T1 and T2 measured with dGPS. The RMSE between TLS and total station was 0.009 m for the black and white targets. The Total station measurement were used to scale and georeferencing the SfM-MVS models.

Target ID	TOTAL STATION (TS)			TLS			Differences between TLS and TS measurement			
	East (X)	North (Y)	Elev. (Z)	East (X)	North (Y)	Elev. (Z)	Est (X)	Nord (Y)	Elev. (Z)	RSE [m]
Black and white targets										
BN1	296965,768	5138497,307	570,129	296965,785	5138497,321	570,124	-0,017	-0,014	0,005	0,023
BN2	296955,101	5138497,879	570,151	296955,099	5138497,893	570,151	0,002	-0,014	0,000	0,014
BN3	296944,126	5138498,584	570,224	296944,143	5138498,591	570,217	-0,017	-0,007	0,007	0,020
BN4	296932,982	5138499,167	570,197	296932,981	5138499,170	570,198	0,001	-0,003	-0,001	0,003
BN5	296922,372	5138499,710	570,184	296922,373	5138499,715	570,178	-0,001	-0,005	0,006	0,008
BN6	296911,420	5138500,557	570,182	296911,411	5138500,560	570,180	0,009	-0,003	0,002	0,010
BN7	296900,636	5138502,071	570,307	296900,628	5138502,086	570,310	0,008	-0,015	-0,003	0,017
BN8	296888,931	5138503,769	569,889	296888,931	5138503,772	569,892	0,000	-0,003	-0,003	0,004
BN9	296878,418	5138506,595	568,759	296878,421	5138506,599	568,762	-0,003	-0,004	-0,003	0,006
BN10	296868,300	5138508,658	567,814	296868,297	5138508,668	567,814	0,003	-0,010	0,000	0,010
BN11	296885,631	5138516,939	561,094	296885,623	5138516,945	561,098	0,008	-0,006	-0,004	0,011
BN12	296833,585	5138529,120	560,381	296833,587	5138529,125	560,387	-0,002	-0,005	-0,006	0,008
BN13	296874,452	5138519,530	560,949	*not measured by TLS*						
BN14	296905,742	5138515,684	561,605	296905,737	5138515,688	561,605	0,005	-0,004	0,000	0,006
BN15	296856,354	5138523,049	561,484	296856,356	5138523,055	561,483	-0,002	-0,006	0,001	0,006
BN16	296839,278	5138518,951	564,924	296839,269	5138518,952	564,923	0,009	-0,001	0,001	0,009
BN17	296859,777	5138512,132	566,835	296859,772	5138512,141	566,838	0,005	-0,009	-0,003	0,011
BN18	296897,958	5138516,095	561,226	296897,952	5138516,100	561,228	0,006	-0,005	-0,002	0,008
GPS targets										
T1	296880,125	5138584,228	565,001	296880,124	5138584,229	565,001	0,001	-0,001	0,000	0,001
T2	296909,728	5138542,116	562,685	296909,729	5138542,155	562,685	-0,001	-0,039	0,000	0,039

Montasio Occidentale glacier

Table A.2. Elevation (m. a.s.l.) and Snow depth estimation (m) calculated with ground penetrating radar (GPR) and elevation difference (DoD) of SfM-MVS DTMs of 2013 and 2014 for the 25 selected points measured with dGPS.

N° of Point	Distance [m]	Coordinates of points					Depth snow 2013-2014	
				GPR	SfM-MVS			
		X	Y	Z $_{\text{GPS 2014}}$	Z $_{\text{DTM 2014}}$	Z $_{\text{DTM 2013}}$	GPR [m]	DoD SfM-MVS [m]
1	0,00	139,26	4237,17	1924,00	1924,50	1924,46	-	0,00
2	12,40	129,81	4231,33	1926,20	1926,70	1926,77	-	-0,14
3	24,80	120,33	4225,59	1928,70	1929,06	1929,10	-	-0,04
4	37,20	111,15	4219,94	1931,00	1931,44	1931,52	-	-0,12
5	49,60	105,23	4210,88	1933,80	1933,83	1933,92	-	-0,12
6	62,00	96,79	4203,69	1936,30	1936,24	1936,39	-	-0,18
7	74,40	88,72	4196,08	1938,70	1938,45	1938,54	-	-0,10
8	86,80	80,64	4188,49	1942,00	1940,88	1940,74	-	0,05
9	99,20	73,05	4180,44	1944,80	1944,10	1943,32	4,80	0,74
10	111,60	66,45	4171,55	1948,40	1947,38	1944,16	6,00	3,17
11	124,00	60,15	4162,44	1951,40	1950,73	1945,64	7,10	5,09
12	136,40	54,13	4153,24	1955,10	1954,15	1947,61	7,20	6,54
13	148,80	47,83	4144,23	1959,20	1957,96	1951,14	6,60	6,83
14	161,20	41,12	4135,58	1963,40	1961,97	1955,78	6,20	6,18
15	173,60	35,22	4126,36	1967,90	1966,27	1960,61	6,30	5,68
16	186,00	29,97	4116,85	1974,40	1971,02	1965,17	6,80	5,85
17	198,40	23,95	4107,52	1983,70	1976,33	1969,57	7,00	6,71
18	210,80	17,46	4099,04	1987,30	1981,94	1974,62	7,00	7,29
19	223,20	14,85	4088,32	1991,60	1988,58	1980,77	6,90	7,65
20	235,60	10,28	4078,21	1997,70	1995,76	1988,27	6,80	7,49
21	248,00	5,15	4068,37	2004,40	2003,00	1995,78	6,20	7,22
22	260,40	-0,64	4058,92	2012,50	2010,54	2003,24	6,00	7,18
23	272,80	-7,06	4049,87	2021,80	2018,40	2011,06	6,00	7,21
24	285,20	-8,11	4042,74	2025,00	2022,33	2016,33	4,00	5,89

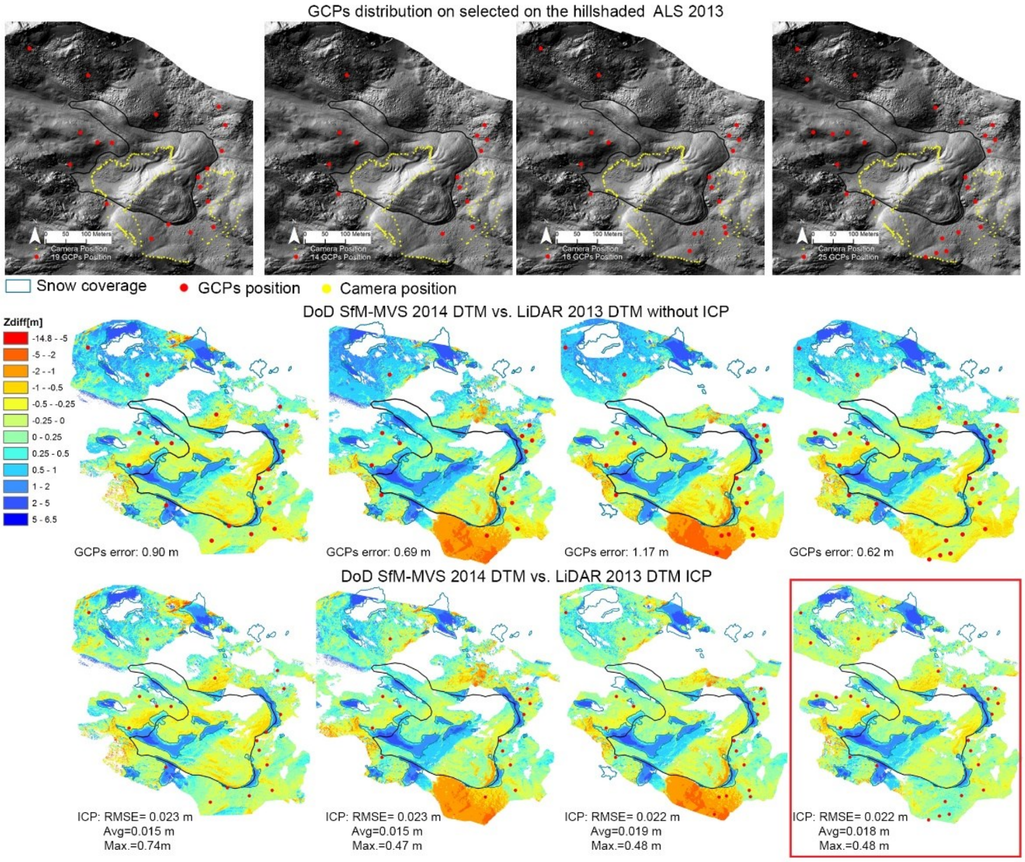

Figure A.4. GCPs selection on the 2013 ALS hillshaded DTM. 4 test before using 4 different number and distribution of GCPs. The accuracy of the GCPs distribution was evaluated as elevation differences (DoD) between SfM-MVS DTM 2014 and the ALS DTM of 2013. The red rectangular represents the best configuration adopted for the surface displacement analysis.

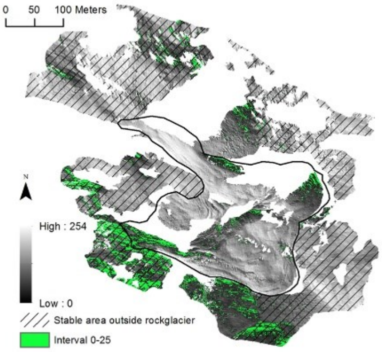

Elevation differences SfM-MVS DTM vs. ALS DTM for hillshaded interval in rock stable area outside Rock glacier

Classes [n]	Hillshaded Intervals	Number of Cells [n]	Min. [m]	Max. [m]	Mean [m]	σ [m]
1	0-25	34880	-8.77	6.54	-0.06	0.79
2	25-56	49682	-6.84	4.18	0.04	0.43
3	56-86	60551	-5.33	4.08	0.02	0.39
4	86-116	63206	-5.62	4.42	-0.01	0.36
5	116-143	75252	-4.56	5.83	-0.04	0.34
6	143-168	94921	-4.66	4.65	-0.06	0.32
7	168-192	90591	-3.61	4.17	-0.10	0.27
8	192-218	78984	-4.81	3.70	-0.09	0.27
9	218-254	48554	-7.08	3.40	-0.04	0.33

Figure A.5. Hillshaded DTM of the SfM-MVS surface reconstruction calculated at the time of the photos acquisition: September 27, 2014; E10 37, N46 25, at 13:30; sun's altitude: 38.6°, sun's azimuth: 206.4°). The altitude and the azimuth of the sun was calculated using a free-web application (Astronomical Applications Dept. U.S. Naval Observatory Washington aa.usno.navy.mil/data/docs/AltAz.php).